THE PENNSYLVANIA STATE UNIVERSITY
SCHREYER HONORS COLLEGE

DEPARTMENT OF BIOENGINEERING

AORTIC OUTLET EXTENSION IN THE 12CC PENN STATE PEDIATRIC
VENTRICULAR ASSIST DEVICE

MICHAEL GLENN FICKES

Spring 2010

A thesis
submitted in partial fulfillment
of the requirements
for a baccalaureate degree
In Bioengineering
with honors in Bioengineering

Reviewed and approved* by the following:

Keefe B. Manning
Assistant Professor of Bioengineering
Thesis Supervisor

William O. Hancock
Associate Professor of Bioengineering
Honors Adviser

Steven Deutsch
Senior Scientist Emeritus
Faculty Reader

*Signatures are on file in the Schreyer Honors College

ABSTRACT

Approximately 36,000 children are born each year with a heart defect, the most common birth defect in the U.S. Due to the low availability of donor hearts, pediatric ventricular assist devices (PVADs) are a possible solution to sustain the life of pediatric patients until a donor heart can be transplanted. Penn State is currently developing a 12cc PVAD, which is a scaled down model of the successful 70cc Pierce-Donachy VAD. This reduction in volume, necessary to accommodate pediatric patients, leads to changes in the functional fluid mechanics. One of these changes is a blockage region upstream of the aortic outlet valve, a characteristic that increases the probability of blood damage and can lead to emboli and other adverse effects. In an attempt to eliminate this region, the outlet port is extended 2 inches away from the model through the use of an acrylic extension. The PVAD is connected to a mock circulatory loop that models the systemic circulation under normal physiological conditions, with a 40% hematocrit blood analog as the fluid. Two dimensional particle image velocimetry is used to acquire flow data throughout the entire cardiac cycle. Results show that the flow patterns in the body of the device remain similar to those previous experiments, except for within the outlet port. With the extension, the velocity profile at the outlet port is more uniform, which in turn, reduces the potential for blood damage.

Table of Contents

LIST OF FIGURES

ACKNOWLEDGEMENTS

I would like to acknowledge my thesis adviser Dr. Manning for all of his patience and support throughout this process. Also, I would like to thank my honors adviser, Dr. Hancock, and my faculty reader, Dr. Deutsch, for their comments and time. I would like to thank the members of the artificial heart lab, especially Breigh N. Roszelle, who helped me greatly in the completion of this thesis. Finally, I would like to thank my family for their support throughout my education, including my research endeavors.

Chapter 1

INTRODUCTION AND BACKGROUND

1.1 Clinical Need

Approximately 36,000 children are born each year with a heart defect, and it is the most common birth defect in the United States. Congenital heart defects are structural defects of the heart at birth. They range in severity from simple holes connecting two chambers (septal defect) to the absence of one or more chambers or valves (pulmonary, aortic mitral, and triscupid). Congenital heart defects are the number one cause of death from birth defects during the first year of life. Almost twice as many children die from congenital heart disease in the United States as die from all childhood cancers. Though some of these children would benefit from a heart transplant, the availability of hearts for transplant is limited. Pediatric patients are the age group with the lowest organ availability and it is especially low in children younger than a year (AHA 2009). In 2005, the waiting list for pediatric patients on average was 107 days, resulting in a high mortality rate, particularly for infants (OPTN 2005). According to the United Network of Organ Sharing (UNOS), while more than 1600 infants were added to heart or heart/lung transplant lists over the past 10 years, fewer than 50% of these children received a donor organ (OPTN 2010). To reduce this high infant mortality rate requires the design of a system to sustain the life of pediatric patients until a donor can be identified. The current options to sustain these patients are quite limited.

Adult patients have the advantage of using FDA approved left ventricular assist devices (LVADs) to bridge the time to transplant. Adults might need LVADs to replace hearts

that have failed through minor defects at birth that did not manifest until later in life, congestive heart failure, or heart attack(s). Ventricular assist devices (VADs) work by taking blood from the right or left ventricle and returning it to the major artery following the ventricle, effectively bypassing the pulmonary or aortic valve, respectively. LVADs feed into the aorta and right VADs feed into the pulmonary artery. In the Randomized Evaluation of Mechanical Assistance in the Treatment of Congestive Heart Failure (REMATCH) trial, the use of implantable LVADs in patients with end-stage heart failure as a permanent alternative to heart transplant or destination therapy (DT) was first investigated. It was found that patients supported with the LVAD had significantly improved 1-year survival, from 25% to 52% (Rose, 2001).

The typical form of support for pediatrics is the extracorporeal membrane oxygenator (ECMO). ECMO, shown in Figure 1, works by taking blood from the right atrium, oxygenating the blood, removing carbon dioxide, and pumping blood back into the aorta. ECMO effectively bypasses and replaces the lungs of the patient and is important to the successful management of respiratory deficiency syndrome of a newborn. Anticoagulant drugs such as heparin are infused with the blood to decrease the probability of clot formation. Fluid is added to ensure that there is enough fluid to fill the device to avoid the formation of gas bubbles. The heat exchanger is placed after the oxygenator to function as a bubble trap and to heat blood back up to body temperature. ECMO is invasive, expensive, and results in many complications that increase in probability with longer usage (Black 1995). The average duration of ECMO support is approximately 72 hours with a maximum of 6 days of support (Karl 2000, Black 1995). Support lasting

longer than 6 days usually results in blood damage, infection, and bleeding (Kawahito 2002). The presence of the oxygenator in the ECMO results in more platelet damage, platelet activation, and hemolysis than for the VAD. Karl et al. has found that in their institution the VAD costs $234 per day for patient and requires one nurse while the ECMO requires two nurses and adds $1050 patient hospital costs per day (Karl 2000). ECMO is useful to support patients for the first 72 hours, after which bleeding, blood damage, infection, and other complications can arise (Karl 2000, Kawahito 2002).
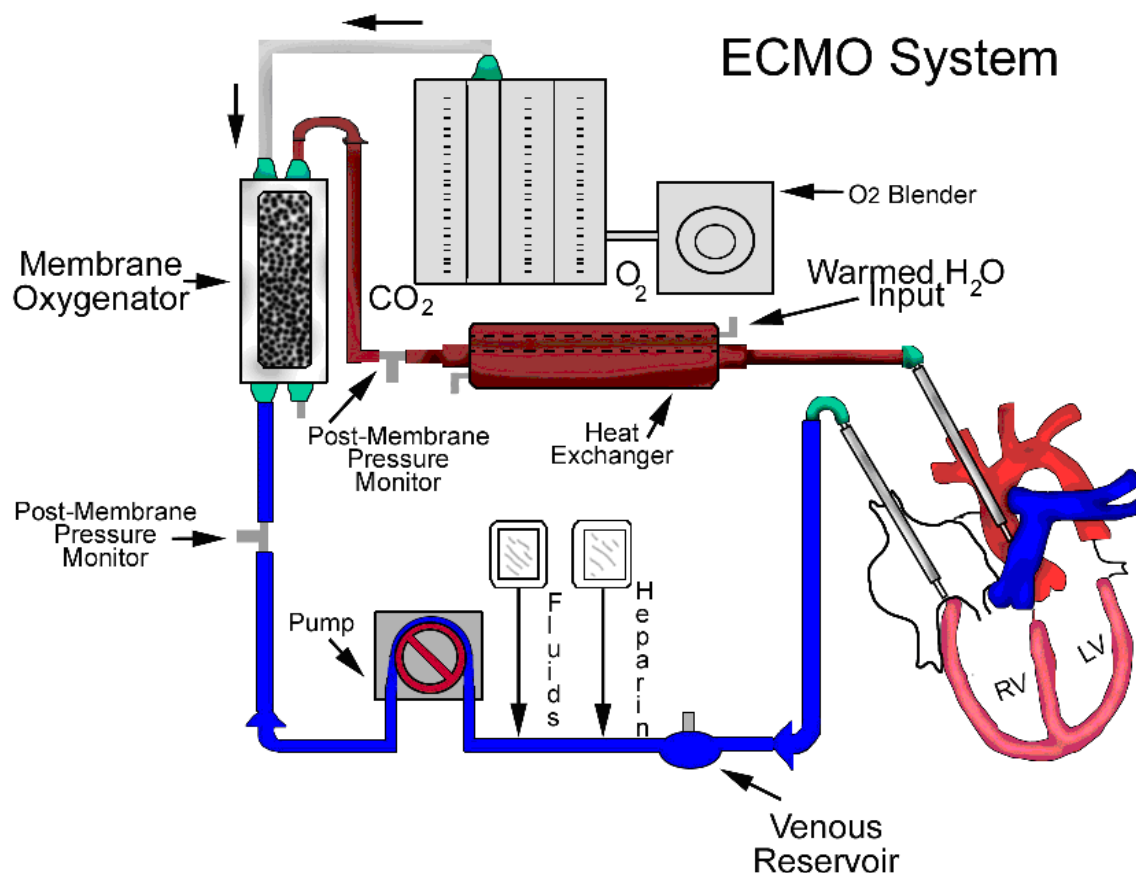

Figure 1: ECMO System. In the figure above, the blood flow through the ECMO system is displayed (Emedicine 2010).

The development of VAD support for pediatric patients has been slow because the demand is lower due to a smaller patient population, large range in body size, and potential patient growth while using the device until transplantation. In 2004, the

National Institute of Health's Heart, Lung, and Blood Institute initiated the Pediatric Circulatory Support Program and five contracts were awarded for the development of pediatric support systems for children ranging from 2 kg to 25 kg. Penn State was one of the selected programs and is currently developing a 12 and a 25 cc pneumatic pulsatile VAD, which are scaled down versions of the successful, adult sized Pierce-Donachy device, now sold as Thoratec® (Baldwin 2006). The use of the Thoratec® and the MicroMed DeBakey VAD® is limited to children over 15-20 kg (Baldwin 2006).

There are two devices, created in Germany, currently under review by the FDA for use in pediatric patients. FDA approval is pending for the Berlin Heart Excor® and the Medos HIA® extracorporeal pulsatile systems and permission to use these devices is granted on a case-by-case basis (Potapov 2007). The Berlin Heart® has achieved a 51% survival rate in a bridge-to-transplant and bridge-to-recovery study conducted on 45 pediatric patients. Of the successful operations, 18 received heart transplants and 5 were weaned from the device (Reinhartz 2002, Goldstein 2005). The MEDOS-HIA has a survival rate of 36.2% (Reinhartz 2002). Both systems have housings that consist of two chambers with a pneumatic compressor-operated diaphragm with valves. They both have transparent polyurethane pump housings that allow early thrombus detection and the external position of the ventricles enables fast and safe pump exchanges if required. The Berlin Heart VAD® consists of the components listed earlier, silicone cannulae, and the Ikus® stationary drive unit. The Ikus® drive unit is an electro-pneumatic drive that contains three separate drives which are able to operate independently of one another. One drive is required for each pump of the Berlin Heart VAD® and the third serves as an

emergency backup. Each drive consists of a compressor, pressure and suction limiters, pressure and vacuum cylinders, and control electronics and valves. The compressor and pressure and suction limiters allow the device to create constant pressure conditions in the pressure and vacuum cylinders (Berlin Heart 2004). The control valves at the outlet of each cylinder allow the overpressure and suction values to be optimally adjusted (Berlin Heart 2004). In the larger pumps and with driving pressures lower than 250 mmHg, the Excor® mobile driving unit can be used. The blood pumps available from Berlin Heart® include volumes of 10, 25, 30, 50, 60, and 80 mL. The pump consists of a translucent, semi-rigid housing of polyurethane and the pump chamber is divided into a blood chamber and an air chamber by a three-layered flexible diaphragm (Potapov 2007). Two air chamber facing layers act as driving membranes while the blood membrane is passively moved by the other two. There is a de-airing nipple integrated into the blood chamber, into which a cannula can be introduced to eliminate residual air after implantation. Trileaflet polyurethane valves are used for the pediatric pumps. All blood contacting surfaces consist of the same polyurethane and are coated with heparin via the Carmeda® process (Carmeda, Upplands Väsby, Sweden). Inflow and outflow connectors are made of polished titanium. This device uses cannulae covered in Dacron velour to encourage scar tissue growth and minimize infection risk. The maximum positive driving pressure provided is 250 mmHg and the maximum negative driving pressure is -100 mmHg. These high pressures are necessary to overcome the high flow resistance of the pediatric cannulae. The system has both univentricular and biventricular modes. During the entire period of mechanical support, small infants receive continuous heparin

infusion (Potapov 2007). Other advantages of the Berlin Heart VAD® over the ECMO include the ability of the patient to be extubated, fed orally, and mobilized.

Medos HIA® has less data currently available than there is for the Berlin Heart Excor® (Potapov 2007). The Medos VAD, which is also available for small children, has been shown to be successful with shorter support time (Potapov 2007).

Blood damage and thrombus formation are the largest issues associated with PVADs. Fully implantable PVADs would function until the patient outgrew it except for the chance of thrombosis and resulting stroke, heart attack, or other infarct. One of the most probable places of thrombus formation is on the blood sac of the device and this can cause the user to need a device replacement. If the clot embolizes, it can lead to the blockage of blood flow in the cardiovascular system leading to tissue damage or death. Therefore most research surrounding new PVADs focuses on the fluid flow within the device to assess the potential of blood damage.

1.2 Fluid Mechanics of Pulsatile Ventricular Assist Devices

The main goal for any cardiovascular prosthetic device is to avoid thromboembolic events. Pulsatile VADs have a larger probability of thrombus formation or embolization because of their complex flow patterns, implantation requirements for long term use, and their large surface area (Hanson 1993). The presence of mechanical heart valves (MHVs) within the device also significantly increases this probability. MHVs can cause hemolysis and platelet activation from high forward velocity flow, cavitation, and strong regurgitant jets that occur after closure (Deutsch 2006 and Lamson 1993). Most pulsatile

devices use MHVs so it is important to assume platelet activation has already taken place when studying the fluid dynamics. The technologies of both assist devices and flow measurement techniques for characterizing fluid dynamics of VADs have improved over the last 30 years. This has improved our analysis of VADs *in vitro*. A useful system for flow characterization is particle image velocimetry (PIV). PIV allows for a faster and more comprehensive look at the flow field patterns when compared to LDV and hot film anemometry (Gharib 2002). It also allows for wall shear rate calculations, as developed by Hochareon et al. (Hochareon 2004). Studies have confirmed that avoidance of low flow near the walls helps prevent deposition (Baldwin 1994). Also established is that wall shear rates less than 500 s^{-1} on segmented polyurethane can promote thrombus deposition (Hubbell and McIntire 1986). A design goal is to create a strong diastolic jet. From systole, the goal is to decrease blood damage, including hemolysis and platelet activation, during the high pressure gradient flow present in the flow near the VAD outlet.

1.3 Particle Image Velocimetry

Various flow techniques such as laser Doppler anemometry, hot film anemometry, and PIV have been used to measure flow in VADs. (Raffel 1998, Deutsch 2008) PIV was chosen here because it has the ability to visualize the entire planes of a VAD flow field, as first shown by Hochareon et al. (Hochareon 2004). PIV is preferred because of the faster data acquisition time, which is important during the design process. PIV analyzes a group of suspended particles as they pass into a light sheet plane. The movement of these particles is measured over a known time (ΔT), allowing for velocities to be calculated.

This study uses a 2-D planar PIV system as shown in Figure 2. A thin light sheet illuminates particles in a desired 2-D plane of view (Raffel 1998). Two light pulses resulting in two images of the illuminated plane are taken ΔT apart and the velocities of the particles are then computed in the x and y direction by the following equations:

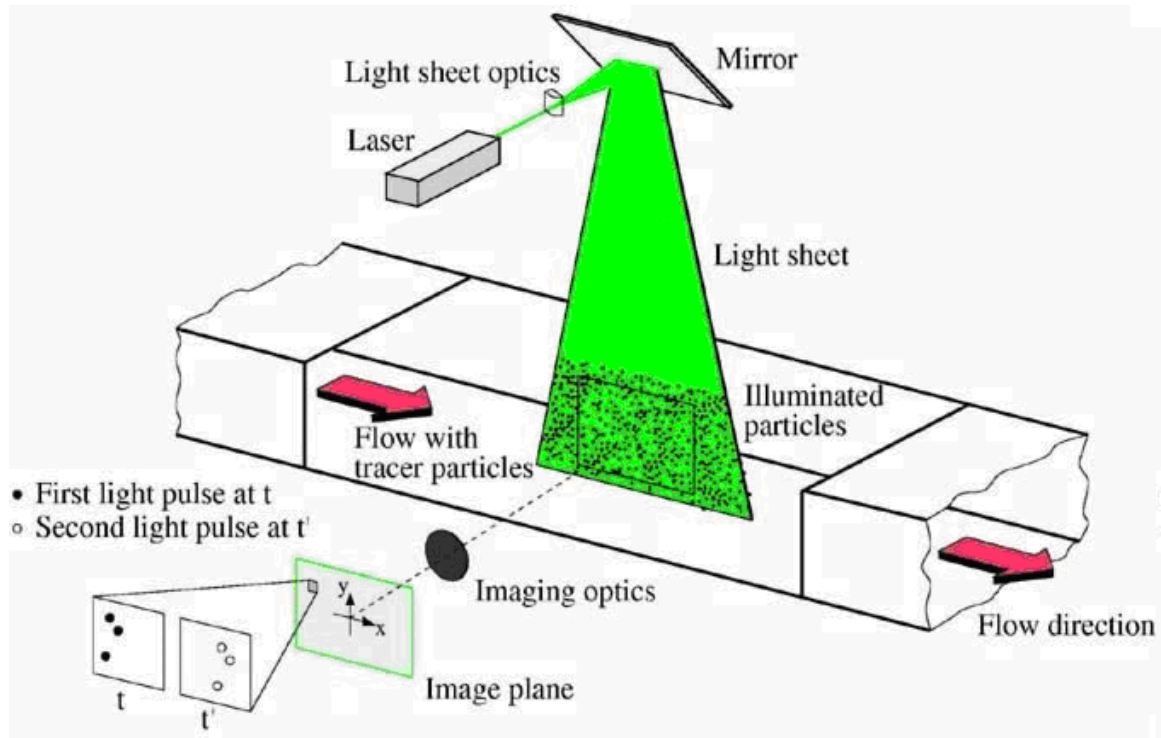$$U = \Delta x/\Delta T \quad (1a)$$

$$V = \Delta y/\Delta T \quad (1b)$$

Figure 2: PIV Representation. The particle illuminated by the plane of light are captured at time t and t'=t+Δt (Raffel 1998).

A modified Stokes number was used to confirm that the particles chosen follow the fluid movement. This number is defined as $\tau_s / \Delta T$ where ΔT is the laser pulse delay and τ_s is the particle relaxation time which is defined as:

$$\tau_s = d_p^2 * \rho_p /18\mu \quad (2)$$

where d_p and ρ_p are the diameter and density of the particle, respectively, and μ is the dynamic viscosity of the fluid. If $\tau_s / \Delta T$ is $<< 1$ then the particle matches the fluid path (Raffel 1998).

In digital PIV, velocities are found by dividing the images into "interrogation regions." These regions are cross-correlated by using pattern recognition of the particle displacement between the two images. A cross-correlation peak occurs where the group particle displacement shifts in the second image. The displacement is used in Equations 1a and 1b to calculate the velocity vectors (Raffel 1998). Error is associated with the ratio of particle diameter to pixel size, particle out-of-plane loss, projection error, and the size of the interrogation region, among other factors (Hochareon 2004, Cooper 2008, Raffel 1998).

1.4 Penn State Pediatric Ventricular Assist Device

Penn State began development of a pediatric version of the successful adult VADs in the late 1980s. The Penn State PVAD is a scaled down version of the 70 cc Pierce-Donachy device, with a volume of 12cc, as shown in Figure 3. The sac and the diaphragm of the device are made of segmented polyurethane. Animal models showed thrombus formation on the sac of the device, which was not previously seen in the adult device. There were also fibrin and platelet deposits throughout the sac infarcts of the kidneys of the animals due to thromboemboli (Daily 1996). Thrombus formation is associated with blood coagulation, the properties of the contacting surfaces, and the fluid mechanics of the device, which are parts of Virchow's triad. As the materials and animal models used in

the pediatric trials were the same as those used for testing the adult device, the increase in the thrombus was linked to the fluid mechanics within the device. There was one major difference between the devices, the MHVs used, which can be considered a fluid mechanics factor. While the 70cc device used adult sized tilting discs valves, the pediatric device was too small for commercial MHVs at the time. Therefore, the initial valves used were 6 mm ball and cage valves that were manufactured in-house. Later the switch was made to a 10 mm bileaflet valve. Daily et al. visualized the device and concluded that the advantages of using the bileaflet valves over the ball and cage valves included a more uniform inlet jet, a more organized diastolic vortex, and a greater volume of ejected fluid during systole (Daily 1996). Initial animal studies with the bileaflet valve showed that while there was still an increase in clot formation relative to the adult device, there was no embolization to the animal's kidneys, which indicates a reduction of both blood damage and thrombus development. More recently Cooper et al. investigated the use of two valves, the Björk-Shiley Monostrut valve (BSM) and the Carbomedics (CM) bileaflet valve and decided the BSM provided better flow for the device (Cooper 2008). In Figure 3 below, the BSM tilting disk valve can be seen, while the different valve types explored before choosing the BSM valve are shown in Figure 4.
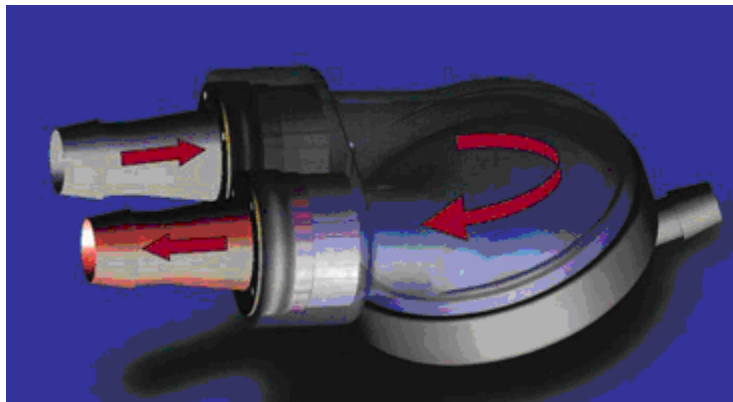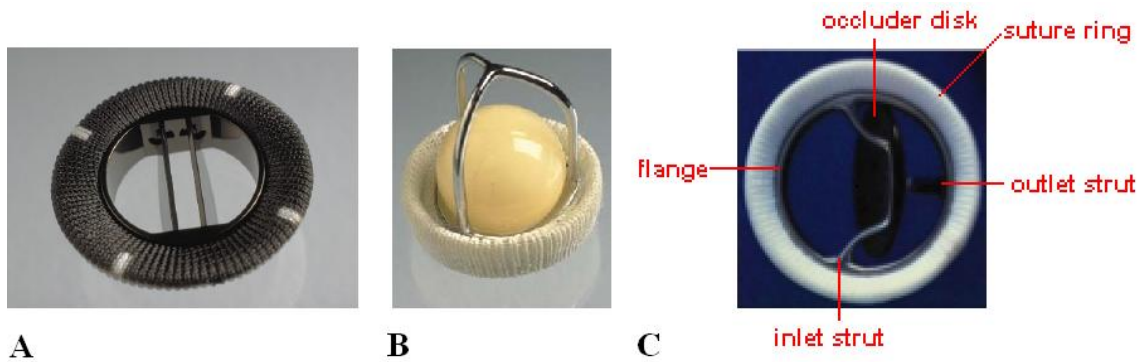

Figure 3: The Penn State PVAD (Cooper 2008).

Figure 4: Valve Types. (A) Carbomedics CPHV bileaflet valve (B) Starr-Edwards ball and cage valve (C) Björk-Shiley monostrut valve.

In 2000 Bachman et al. compared the PVAD to the 70 cc device through dimensional analysis and found the Strouhal (St) number (St = fL/V) was much higher in the PVAD (45.3 vs 8.3). The Strouhal number taken with the Reynolds (Re) number (Re=ρVL/μ) provides an indication of geometric similarity. Therefore, these devices are not geometrically similar. They also used laser Doppler velocimetry (LDV), a method that uses light scattering from particles in a flow, to characterize the internal flow field. They determined that the design of the device yielded an environment more prone to induce clot formation by the presence of wall shear below 500 s^{-1} at many locations (Bachmann 2000). It has been reported that scaling of the 70cc device to a size suitable for pediatric patients changes the flow, leading to an increase in thrombogenicity within the device (Daily 1996, Bachmann 2000).

Manning et al. was the first to investigate flow within the Penn State 12cc PVAD (Manning 2008). In the 12cc Penn State PVAD, Cooper et al. and then Roszelle et al. found a blockage region present within the device at the outlet, as shown in Figure 5

(Cooper 2008, Roszelle 2008). This blockage region causes fluid to travel at higher velocities along the sides of the port at a higher pressure gradient, which can result in blood damage and platelet activation. This blockage region is not seen within the adult VAD. Roszelle et al. found that the flow within the Penn State PVAD is more three dimensional compared to the adult VAD (Roszelle 2010). In addition to elements of the flow field found in two dimensional analysis of the flow such as the start of rotational flow, flow penetration of the bottom of the device, and the area of separation at the outlet, new information was obtained from the three dimensional analysis including areas of regurgitation and recirculation in the ports (Roszelle 2008). Therefore, planes were taken in both parallel and normal to the diaphragm so that the flow throughout the device could be better characterized. These planes are discussed more fully in Chapter 2.
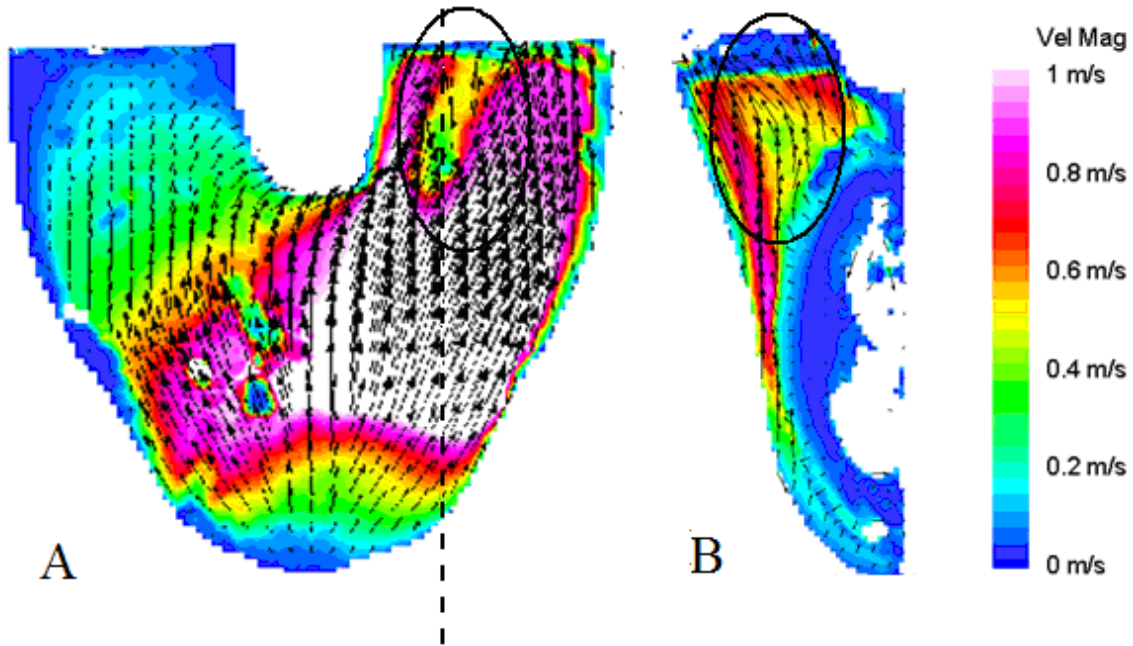

Figure 5: Blockage Region. The images, (A) 8.2 mm body parallel plane and (B) 3.75 mm outlet normal plane show the blockage region in the outlet of the PVAD. The dotted line shows where the plane in (B) is located in the plane shown in (A) (Roszelle 2008).

1.5 Purpose

In this study we explore moving the outlet valve to end of the acrylic extension to eliminate the outlet blockage. As a possible solution to this flow problem, the placement of the valve may allow the flow to adjust to the port before being forced through the major and minor orifices of the outlet valve, instead of experiencing these disruptions to the flow at the same point in the device. If the blockage observed in past experiments can be altered or eliminated, the hemocompatibility of the device can be improved. Secondary goals of this experiment are to confirm that the flow through the rest of the device remains similar. PIV will be used to analyze the flow with conditions that are standard operating conditions for the PVAD.

Chapter 2

MATERIALS AND METHODS

2.1 The PVAD Model

In order to gather PIV measurements, an acrylic model of the PVAD was constructed. The acrylic model was designed to represent the physical boundary of the sac of the device, contain an inlet and an outlet valve, and to contain a connection to the pneumatic driver. The acrylic is made of two pieces to allow placement of the diaphragm and the blood sac, which is made of segmented polyurethane. For these experiments, only the BSM valve with an effective orifice area (EOA) of 1.1 cm^2 was used in the model. The BSM valves were oriented in such a way that the major orifice opened to the outside wall of the device and the strut was parallel to the diaphragm. A schematic of this is shown in Figure 6 and a model of the PVAD is shown in Figure 7.
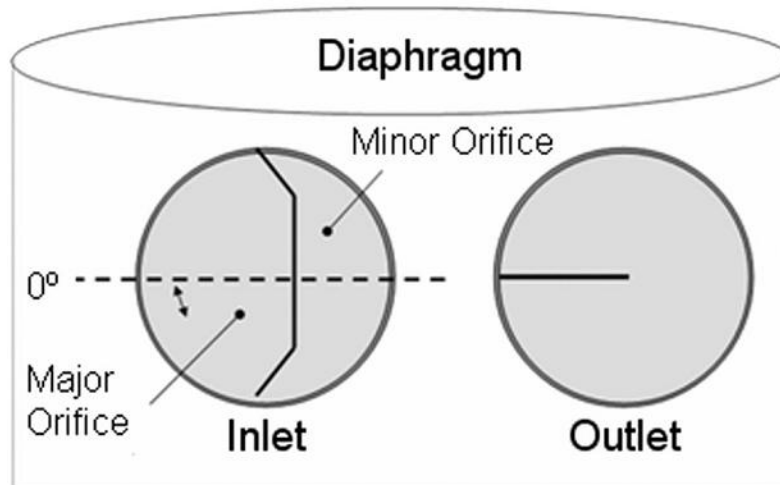

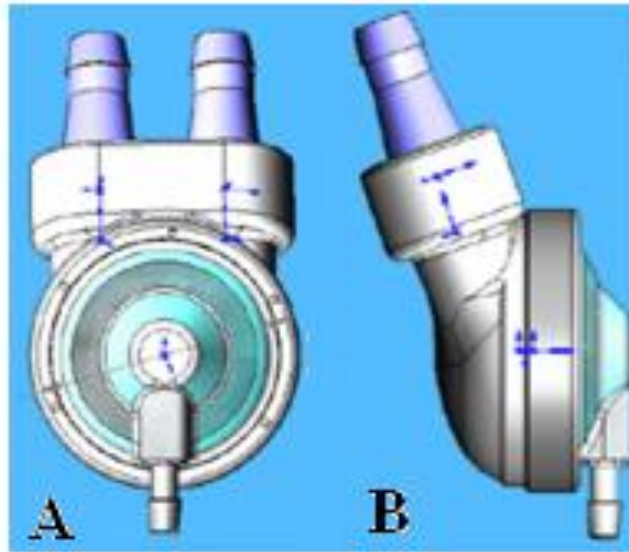**Figure 6:** BSM Valve Orientation Representation.

Figure 7: Solidworks Drawing of the PVAD Model Covering. (A) Back View (B) Side View

2.2 Port Extension and Valve Movement

The outlet port of the PVAD was lengthened using the extension shown in Figure 8. The extension has a height of 49.90 mm, a width of 76.35 mm, and a depth of 25.55 mm. The diameter of each extension is 14 mm in order to match the size of the port. One end of the extension fits where the valve used to reside in the model and the other end has a place that holds the outlet valve. The ports of the PVAD are inserted into the part of the extension at the bottom of the image and then the cannulae are attached to the extension at the part shown at the top of the image. The extension is held to the PVAD using methods similar to those used by the original design (Manning 2008). An image of the PVAD with the newly attached extension can be found in Figure 9.
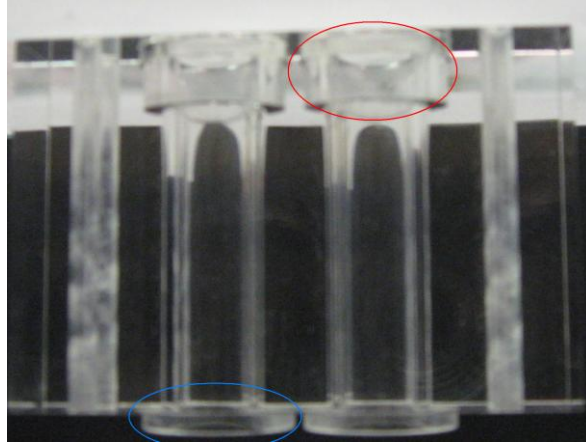
Figure 8: Port Extension. Circled in red is where the outlet BSM valve was placed. Circled in blue is where the extension fits onto the model right on top of the inlet valve.
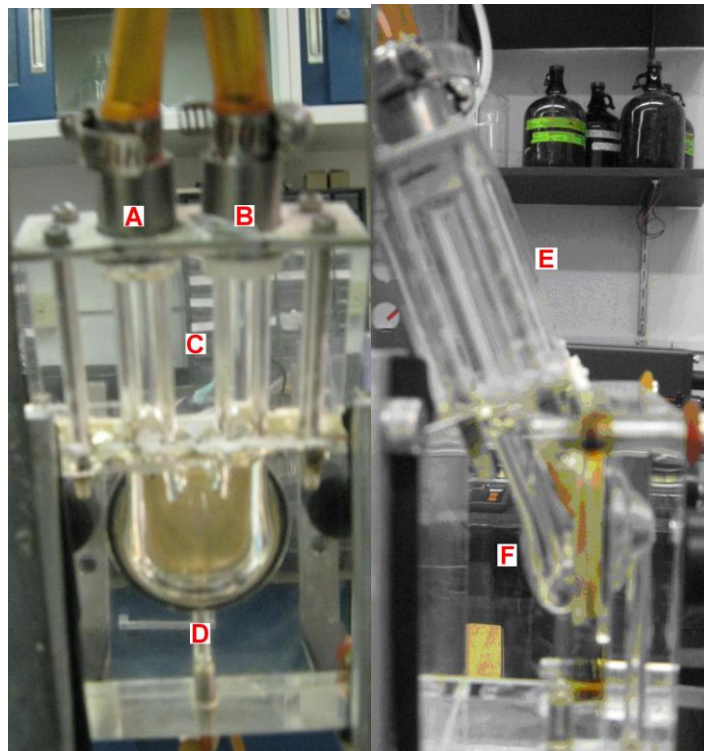

Figure 9: PVAD with Extension. Front view (left) with the inlet (A), outlet (B) extension (C) and the PVAD (D), Side view (right) with the extension (E) and the PVAD (F)

2.3 Mock Circulatory Loop

In addition to the PVAD model, the flow throughout the cardiovascular system must also be simulated through the use of a mock circulatory system. The mock circulatory loop is

based on the adult loop first developed by Rosenberg (Rosenberg 1972). In order to use the loop with the smaller pediatric model, the overall volume was reduced while the overall resistance was increased. The loop contains components that represent the resistance, compliance and inertance of the circulatory system. Figures 10 and 11 show a schematic and actual images of the flow loop, respectively. The two compliance chambers that represent arterial and aortic compliance are shown in Figure 12. The chambers have a piston resisted by a variable spring force which allows the chamber volume to fluctuate during pressure pulses. The cantilevered beams on these chambers may be adjusted to obtain the desired difference between the high and low pressures representing the systolic and diastolic pressures, respectively. The tubing used within the flow loop was flexible Tygon® 3603 tubing (Saint-Gobain Performance Plastics, Aurora, OH). In order to obtain the desired resistance, a section of the flow loop tubing was placed between two 10" x 6" plates, shown in Figure 12, which could be tightened or loosened to raise or lower the resistance, respectively. This resistance represents the systemic resistance of the body. The venous reservoir is shown in Figure 12. As fluid passed through the reservoir, it was mixed by a stir bar at 300 rpm to maintain a homogenous mixture within the loop. The pneumatic driver creates pulsatile flow throughout the loop using pressure and vacuum pumps on one side of the diaphragm of the device. The pressure and vacuum values could be changed, as could the beat rate and systolic duration.
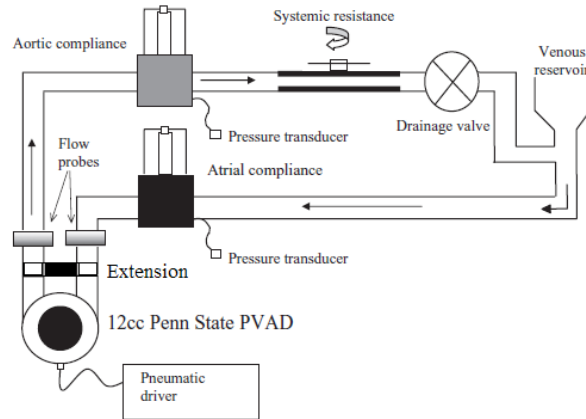
Figure 10: Mock Circulatory Loop Schematic (Adapted from Manning 2008)
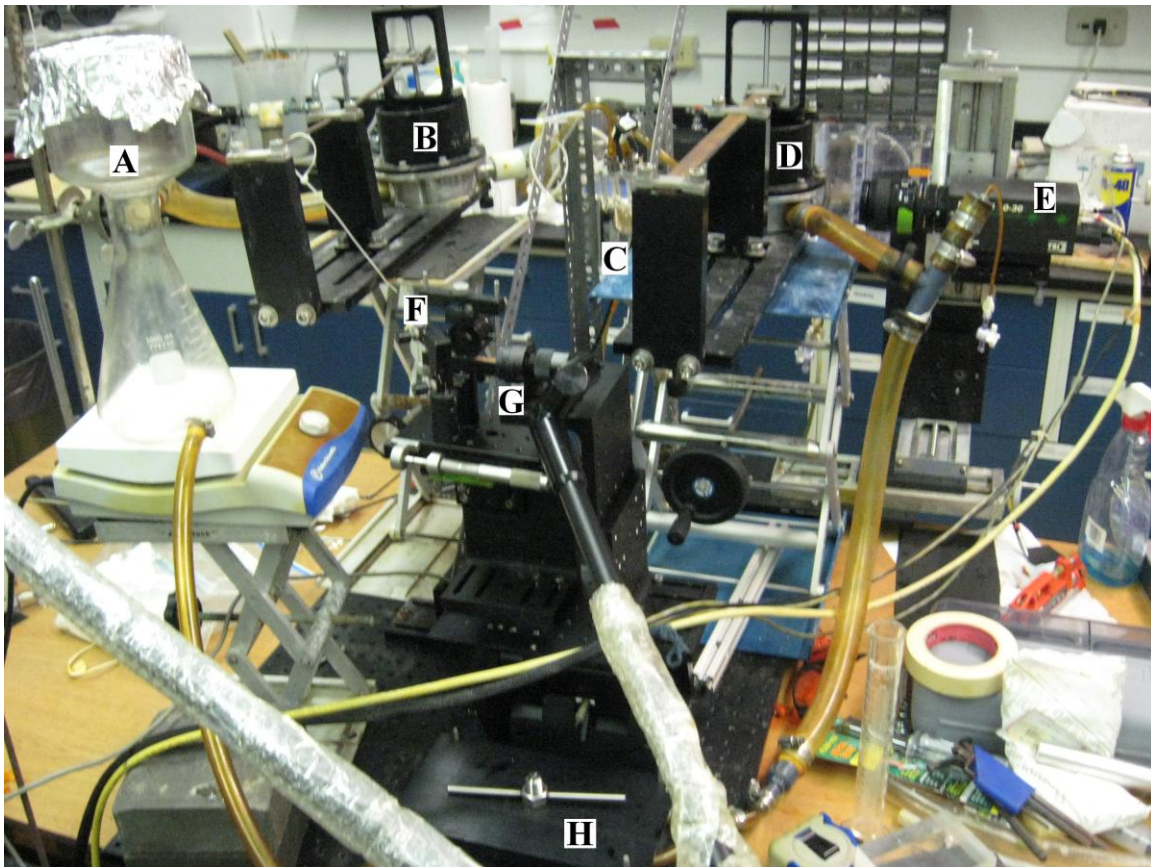

Figure 11: Mock Circulatory Loop. Shown above is the mock circulatory loop with the (A) venous reservoir, (B) atrial compliance, (C) PVAD with extension, (D) aortic compliance, (E) PIV Camera, (F) laser optics, (G) light source and (H) resistance plate.
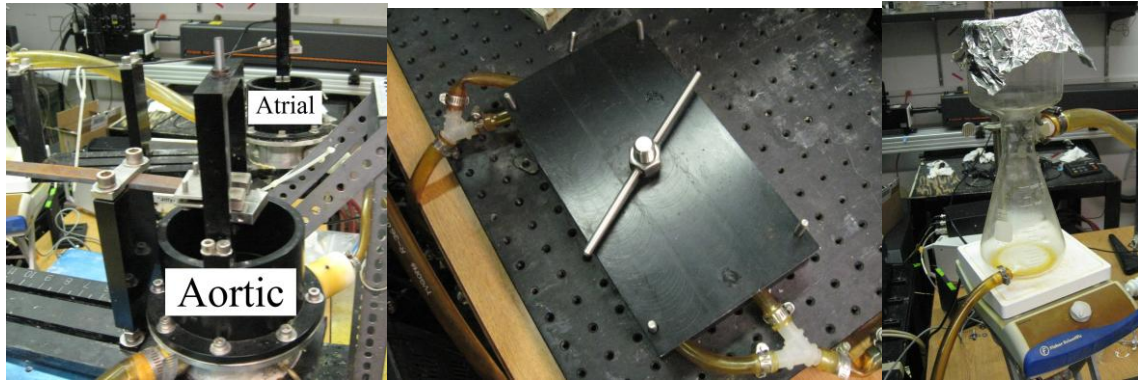
Figure 12: Loop Components. Aortic and Atrial Compliance Chambers (left), Resistance Plates (middle), and Venous Resevoir (right)

The loop conditions were chosen in order to match the conditions used clinically. The beat rate was set at 75 beats per minute (bpm) and systolic duration was set at 340 ms. The aortic or outlet pressure was set at 90/60 mmHg. The atrial or inlet pressure was set at 70/40 mmHg. The inlet pressure is set higher than values seen clinically, but it was discovered that this still allows for physiological behavior of the device. Inlet, outlet, and pneumatic pressures were measured using pressure transducers (Maxxim Medical, Athens, TX). Signals were converted and displayed using a Wavebook acquisition system and WaveView software (IOtech, Inc., Cleveland, OH).

The flow rate was obtained after the outlet and before the inlet of the PVAD using an ultrasonic flow probe system (Transonic Systems, Inc., Ithaca, NY). The average flow rate was maintained at 1.3 lpm. The drive pressure and vacuum were set to ensure complete filling and complete ejection of the pump. Complete filling is having the entire device fill before it ejects the fluid out of the outlet. This is shown on the waveforms in Figure 13, where inflow reaches zero prior to the increase in the drive pressure that starts the ejection period. These are the same conditions that were used when the blockage was

identified. In order to have complete ejection, the time period between the start of positive driveline pressure and zero outflow must be the same or less than the systolic duration. For consistency, the time period between the end of diastole and the beginning of systole, known as the end-diastolic delay, was kept between 0 and 10 ms.
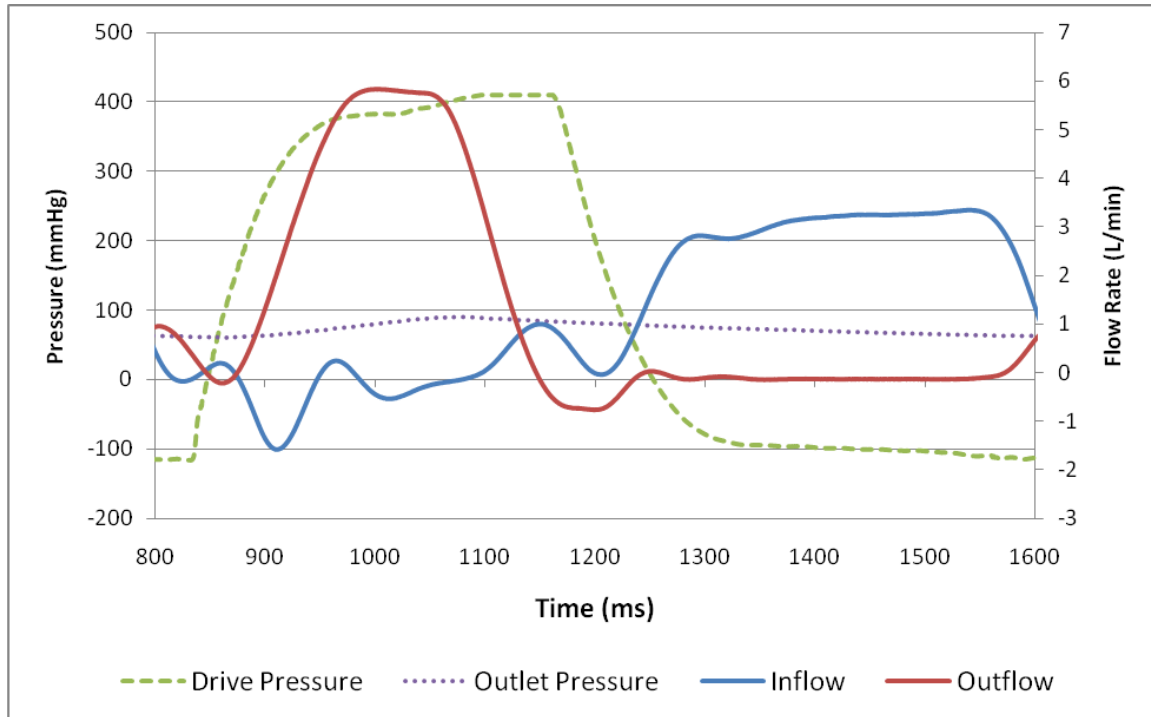

Figure 13: Flow Waveform

2.4 Fluid

For flow visualization, we use a viscoelastic blood analog that models 40% hematocrit pediatric blood. The blood analog used consists of Xanthan gum (0.03%), glycerin (16%), water (35%), and sodium iodide (50%) by weight and is described in detail by Long et al. (Long 2005). The Xanthan gum provides the elastic and shear thinning properties of the blood analog. The glycerin increases the viscosity of the fluid. The refractive index of acrylic is 1.49, and the sodium iodide is used to make the fluid match the acrylic refractive index. In order to perform PIV, the fluid was seeded with 10 µm

glass beads that function as light scatterers. The viscosity of the fluid was 3.5 cP and the density was 2.5 g/cm^3. A Stokes number much below 1 guarantees the particle path will match that of the fluid, which was 3.97 e^{-6} for this experiment.

2.5 PIV System

The laser system used was a Gemini PIV 15 system (New Wave Research, Inc., Fremont, CA), which includes dual Nd:YAG lasers to produce a 6 mm light beam that was shaped into a 200 µm light sheet using a -25 mm cylindrical lens coupled with a 25 mm diameter high-energy mirror and a 500 mm spherical lens. The images were captured using a one megapixel charge-coupled device (CCD) camera (TSI, Inc., Shoreview, MN) with a Micro-Nikkor 60mm f/2.8D lens (Nikon Corporation, Tokyo, Japan). A LaserPulse synchronizer (TSI, Inc., Shoreview, MN) and a personal computer (Dell, Inc., Round Rock, TX) were used in combination as part of a frame-straddling technique. The image acquisition software used in this experiment was INSIGHT™ 3G Global Image Acquisition, Analysis and Display Software (TSI, Inc., Shoreview, MN). A trigger delay box was used to capture the images at specific times in the cardiac cycle, based on the start of inflow of the device. The ΔT used between each image pair was 200 µs for all data acquistion. Images were captured every 50 ms throughout the cardiac cycle, except for early diastole and late systole when the diaphragm interferes with the laser sheet or the image. Two hundred images were taken at each of these time steps in order to provide a sufficient number to average during post-processing.

Due to the fact that 2-D PIV was used to look at a 3-D flow, we measured the flow using planes both normal and parallel to the diaphragm. The parallel planes, taken at 7, 8.2, and 11 mm from the edge of the ports, are shown in Figure 14. The planes normal to the diaphragm at 3.75, 7.5, and 11.25 mm from the edge of both the inlet and outlet port and in the center of the model, are shown in Figure 15.
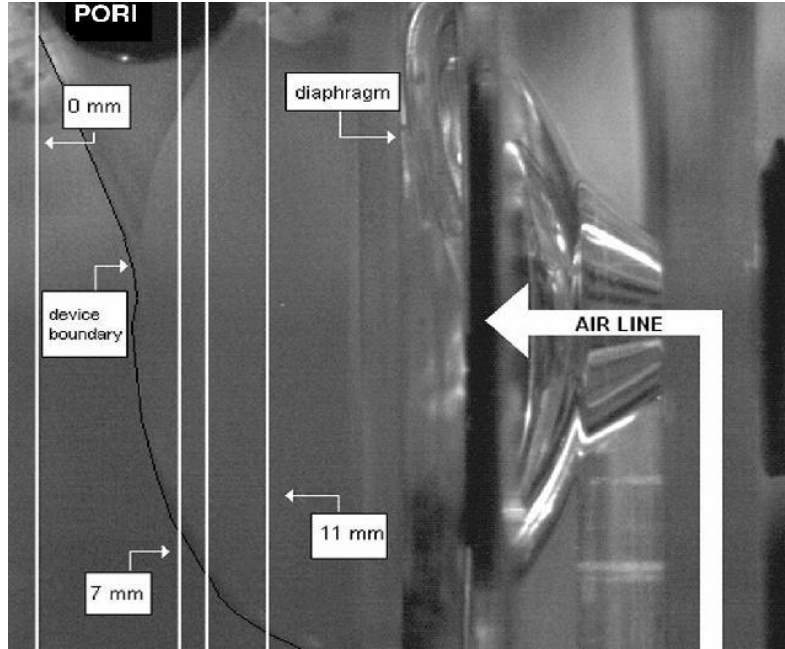

Figure 14: Parallel Body Planes. The 8.2 mm parallel plane is shown by the white line between the 7 mm and 11 mm labeled planes (Roszelle 2008).
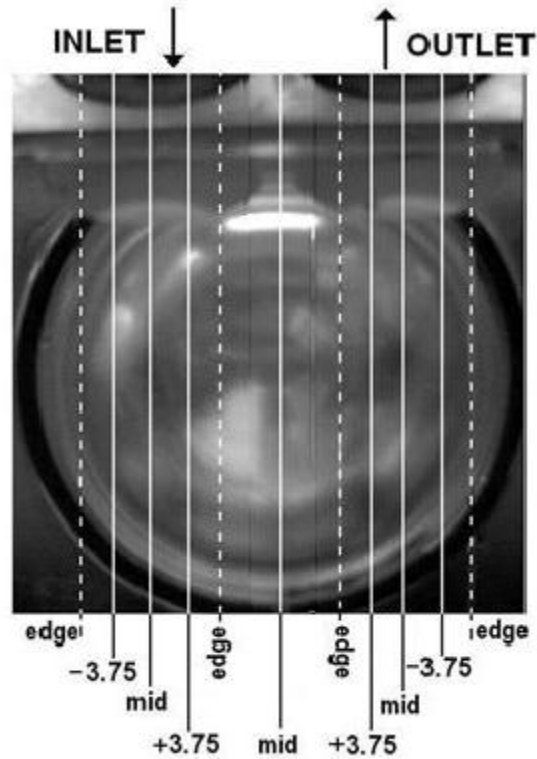
Figure 15: Normal Body Planes (Roszelle 2008).

Extension parallel planes were taken by orienting the camera at a 20º angle above the horizontal facing the extension. The laser light plane was angled as well by lining up the plane with the side of the extension. The image planes taken are shown in Figure 16. The extension inlet and outlet planes were acquired by firing the laser directly at the center of each port of the extension and 3.5 mm to either side of the center of each port. During the collection of these planes, the camera was aimed at the device from the inlet side for the inlet planes and the outlet side for the outlet planes. These planes are shown in Figure 17.
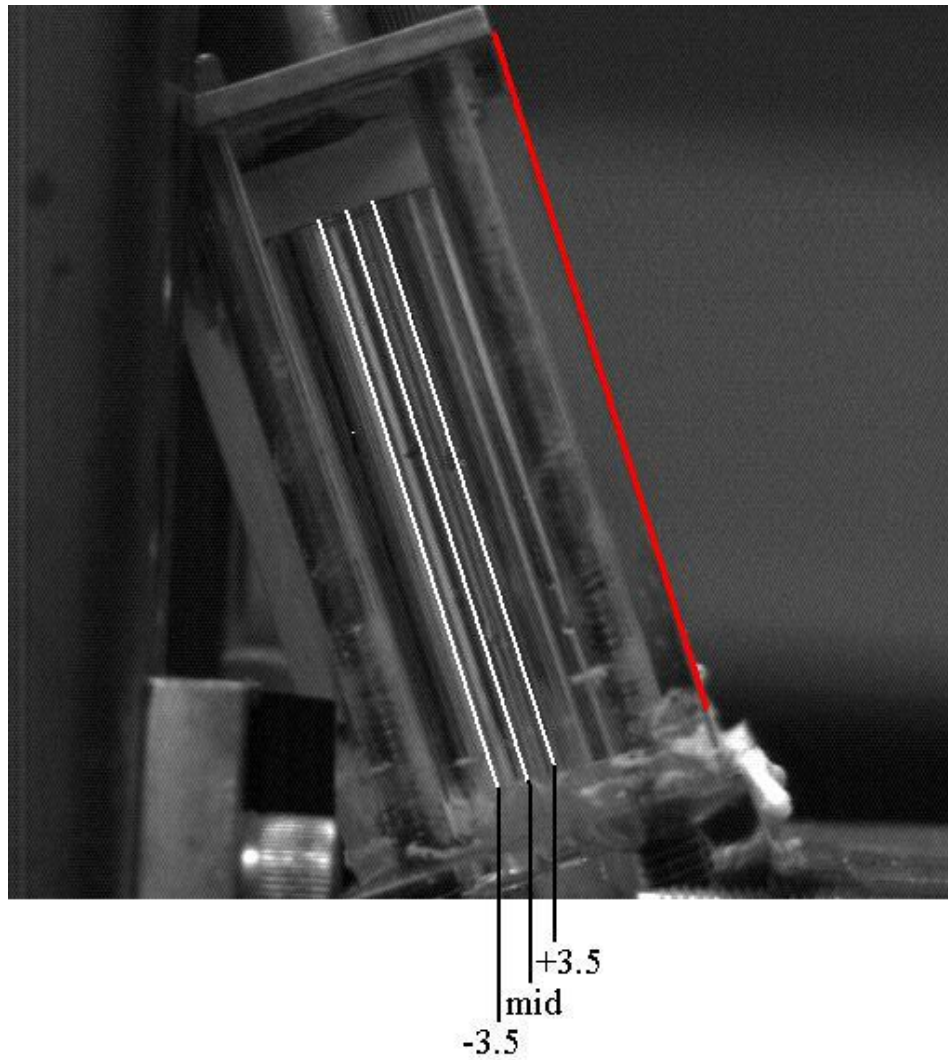
Figure 16: Parallel Extension Planes. The white lines representing the parallel extension planes. The red line shows the edge of the extension that the laser plane was angled to match before taking data.
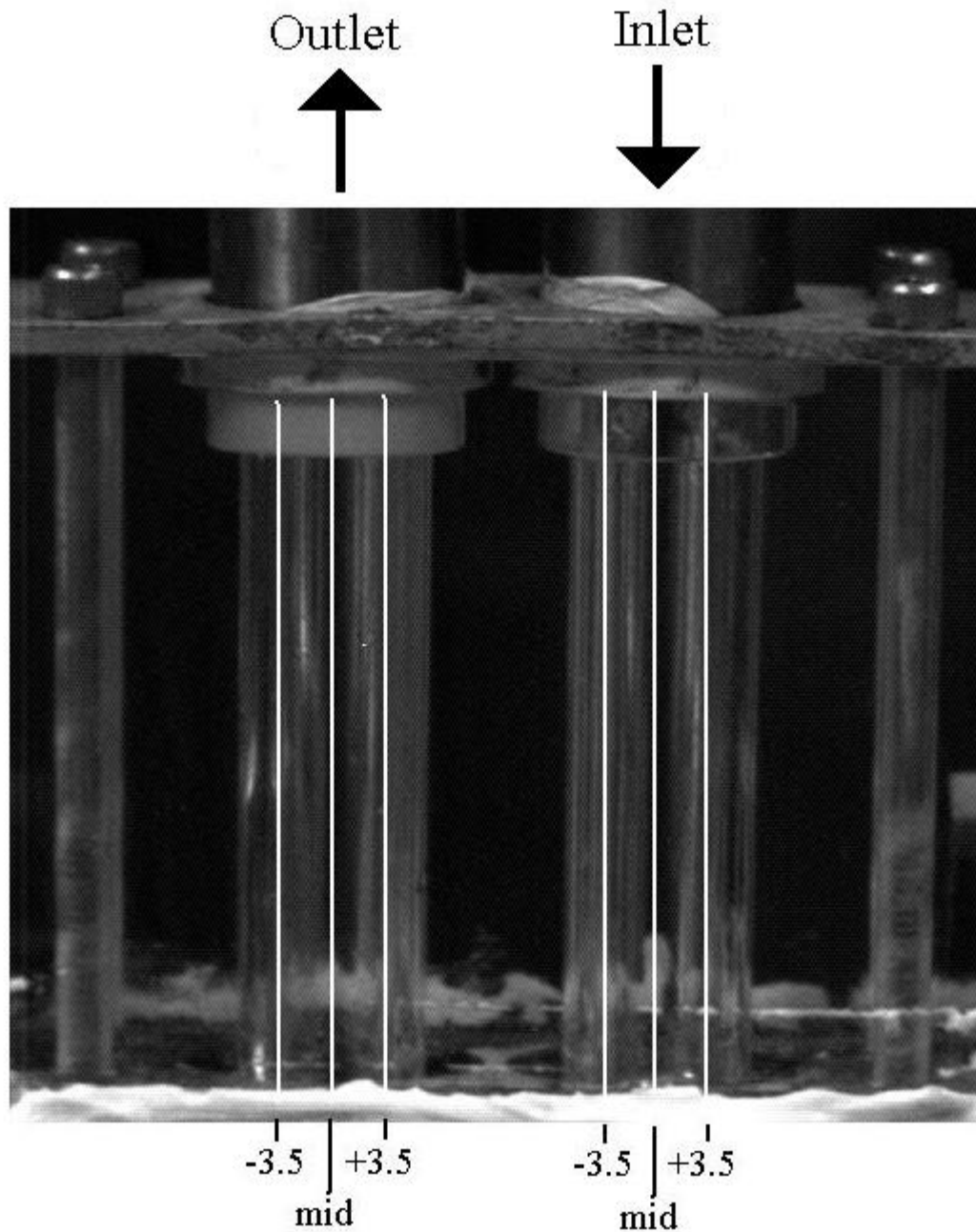
Figure 17: Normal Extension Planes.

2.6 Processing

First, the images are masked using a custom Matlab ® program (The MathWorks, Inc., Natick, MA) (Hochareon 2004). This program locates the fluid boundary of the image and removes the background noise surrounding the image. We then used INSIGHT ™ 3G

to calculate velocity vectors for each pair of PIV images. A deformation grid was used with an original interrogation region of 32 x 32 pixels and a final region of 16 x 16 pixels. For cross-correlation, the Hart Correlation algorithm was used because it efficiently uses information acquired from correlation algorithms that overlap interrogation regions (Hart 1999). The resolution was 50 μm/pixel for the parallel planes, 41 μm/pixel for the normal planes, 45 μm/pixel for the center of model plane, 55 μm/pixel for the extension outlet planes, 45 μm/pixel for the extension inlet planes, and 50 μm/pixel for the extension parallel planes. Once the vectors were all calculated, 200 vector files from each time step were averaged. This provides a single averaged velocity for each time step in each plane. Two hundred images were sufficient to provide a stable average velocity at each time step, as discussed in the work of Hochareon et al. (Hochareon 2004).

2.7 Error Analysis

A major source of error in our measurements is bias error associated with our PIV system (Cooper 2008). PIV error analysis has shown that measurements are sub pixel accurate up to 10-20% of the spatial resolution (Raffel 1998). Assuming 20%, this yields a minimum 10 μm for the parallel planes, 8.2 μm for the normal planes, 9 μm for the center of the model plane, 11 μm for the extension outlet planes, 9 μm for the extension inlet planes, and 10 μm for the extension parallel planes. By dividing minimum sub pixel accuracy values by the ΔT of 200 μs, the minimum accurate velocities were calculated to be 0.05 m/s for the parallel planes, 0.041 m/s for the normal planes, 0.045 m/s for the center of model plane, 0.055 m/s for the extension outlet planes, 0.045 m/s for the

extension inlet planes, and 0.05 m/s for the extension parallel planes. Pixel locking, for which displacement peaks are locked to integer velocities, has been thoroughly discussed by Raffel and others (Raffel 1998). It is likely to occur for particles that are too small relative to the pixel size or for unrealistically small ΔTs and has been shown by Cooper et al. to not be a factor here (Cooper 2008).

Other errors associated with PIV are due to out-of-plane loss and projection error. Observing vector counts of each flow map allowed out-of-plane loss to be tested. Any areas that showed vector counts less than 50 were considered inaccurate and not used. Projection error is associated with high magnification PIV, which was not used in this study (Raffel 1998).

Chapter 3

RESULTS

The results of PIV are shown as flow maps. The magnitude of the flow is indicated by the arrow length and the color legend. The orientation of arrows represents flow direction. Each of these maps is an averaged map of a particular PIV plane at a known time step in the cardiac cycle.

In the flow map in Figure 18, the valve which can be seen at the top of the image is causing pixilation. Pixilation can also be caused by interference by the diaphragm and can present itself as a dark blue or white area in the flow field. The pixilation seen in images in the Results and Discussion is blocked and replaced with a label to show what component of the PVAD is blocking visualization. Also, velocities closer to the top of the port are not measureable due to valve interference so the flow closer to the port can only be inferred from flow just downstream of the inlet valve.
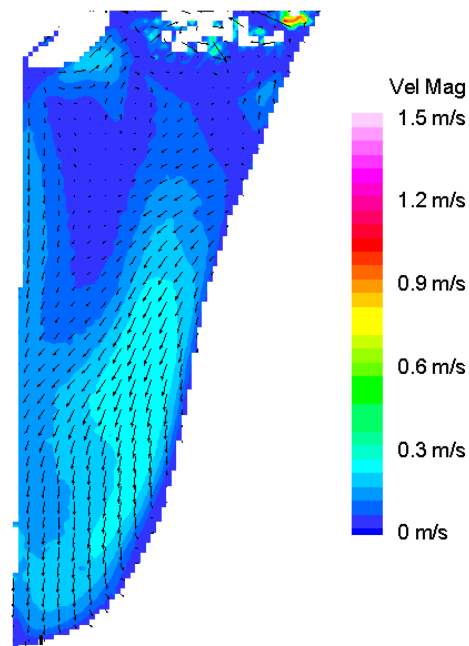
Figure 18: Sample Flow Map at the 450 ms time step.

3.1 Flow in the Body Inlet Port

As expected the inlet jet is of the highest velocity in the inlet normal plane towards the outside of the device, because most of the flow is through the major orifice of the valve. Figure 19 shows the start and early development of the inlet jet.
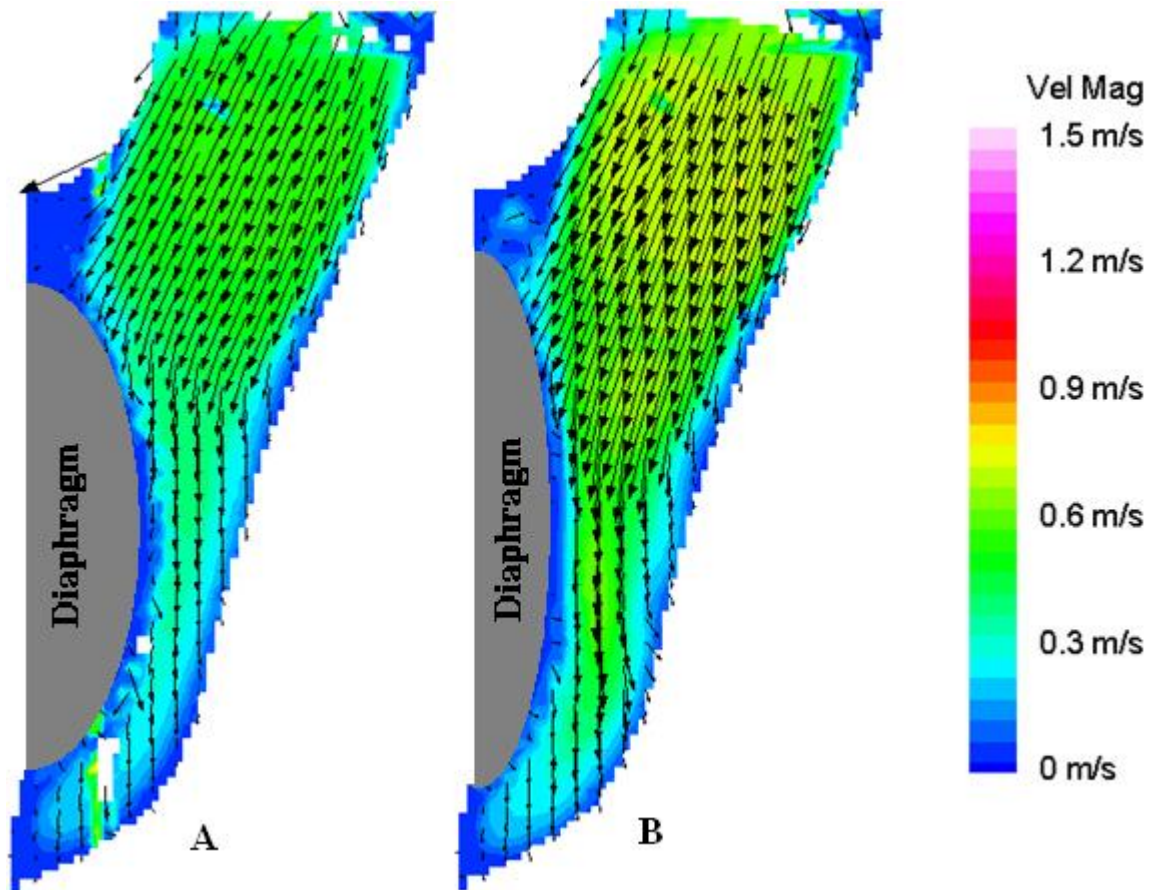

Figure 19: Inlet Port (Start of Diastole). These are both 3.75 mm normal body inlet plane images at timesteps (A) 50 ms and (B) 100 ms.

As the jet starts to form in the 3.75 mm plane, velocities above 0.7 m/s at 100 ms into the cycle occur. This jet formation is also seen in the 7.5 mm and the 11.25 mm planes. All three planes at 200 ms are shown in Figure 20. The peak velocities in the 3.75 mm, 7.5 mm, and 11.25 mm planes reach 0.9 m/s, 0.8 m/s, and 0.9 m/s, respectively. Downstream of the inlet of the PVAD is a wake caused by the BSM valve disk which is also shown in

Figure 20A and 20B. Figure 20B shows the inlet jet reaching the bottom of the device in early diastole. As the space the diaphragm takes up in device decreases, shown in Figure 20, more flow is allowed within the body. Figure 21A displays that the flow penetrates the bottom of the device at 200 ms instead of 150 ms. Also in Figure 21, the higher flow is closer to the valve, because the fluid is being forced through the smaller area of the valve until it is able to spread throughout the body of the device.
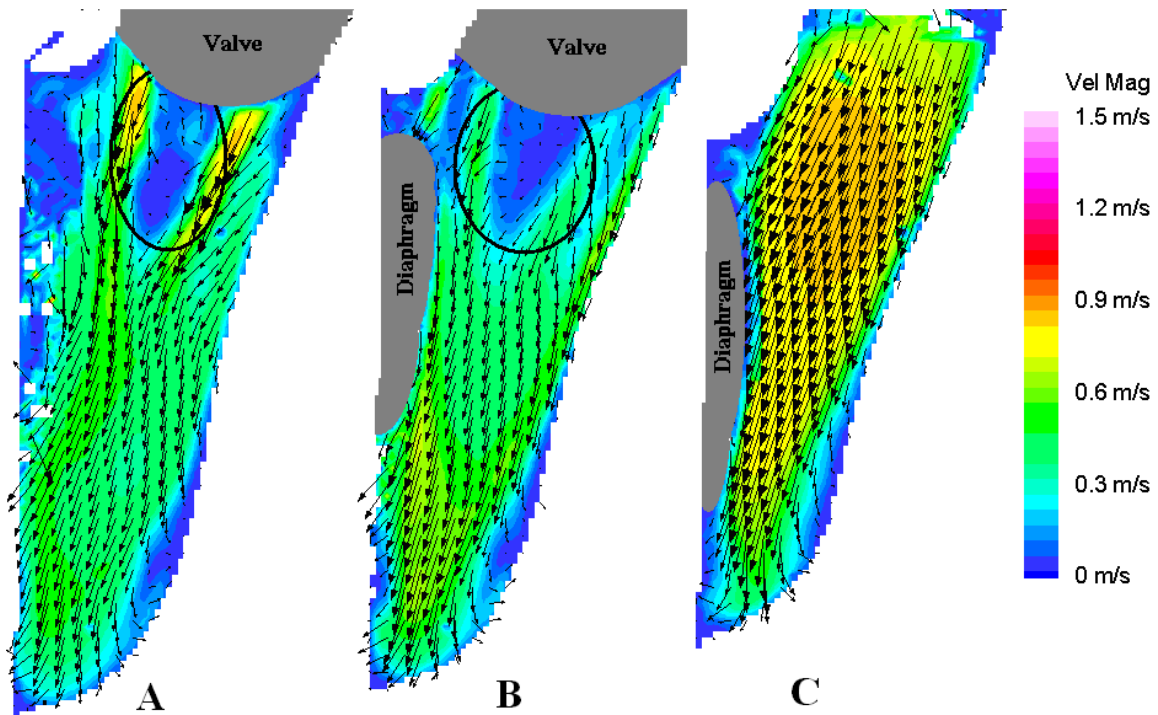
Figure 20: Developed Inlet Jet. All these images are all at 200 ms. (A) Inside. (B) Middle. (C) Outside planes. The velocity was highest in the outlet jet in (C) because the major orifice is located in this plane.
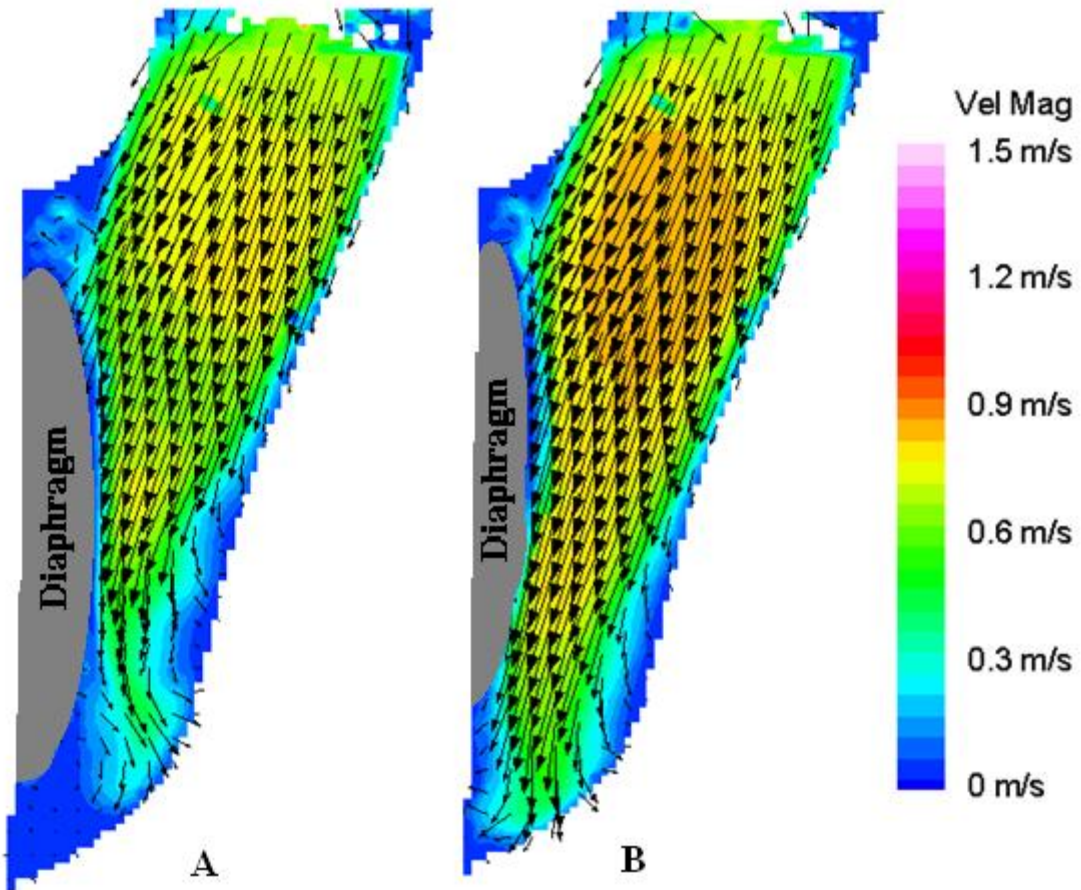
Figure 21: Inlet Port (Early Diastole). These are both 3.75 mm normal body inlet plane images at (A) 150 ms and (B) 200 ms.

Figure 22 shows both the presence of a low flow region at the bottom of the device and a stagnation region downstream of the port. The decrease of fluid velocity as it penetrates farther into the body of the device is also seen in Figure 22.
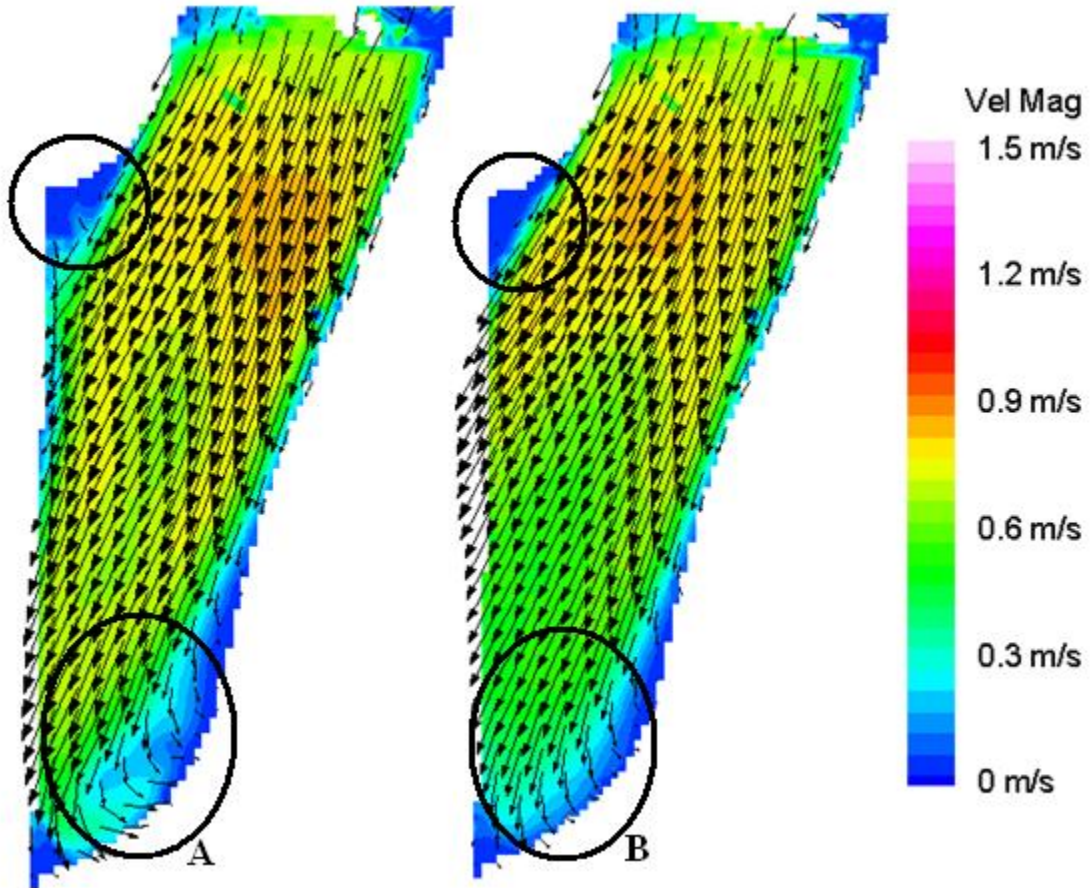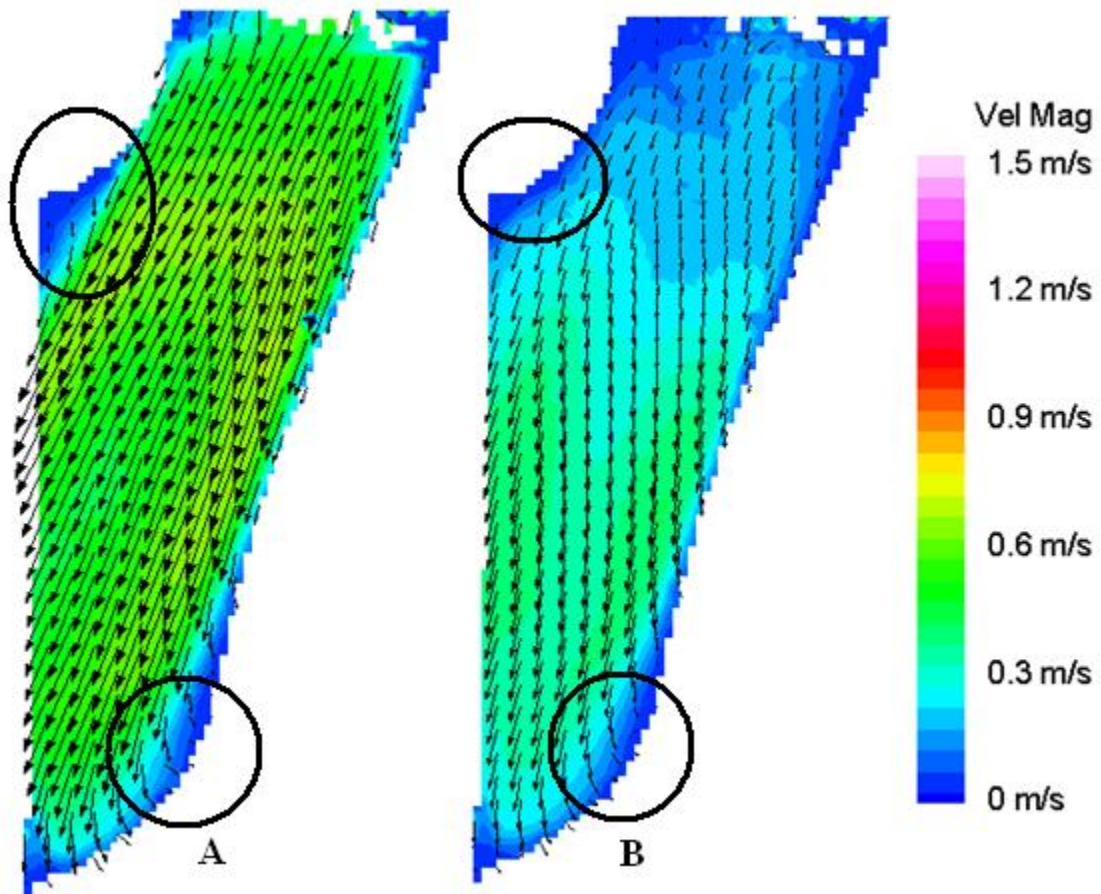

Figure 22: Inlet Port (Mid Diastole). These are both 3.75 mm normal body inlet plane images at (A) 250 ms and (B) 300 ms. The top circle in both images represents a stagnant flow region and the bottom circle in both images represents a low flow region.

Figure 23 shows that the previously noted stagnant flow region still exists in late diastole and low flow is still seen toward the bottom of the device. By 400 ms, the flow has slowed considerably due to the transition from diastole to systole. Also low flow is now discovered closest to the minor orifice side in Figure 23B.

Figure 23: Inlet Port (Late Diastole). These are both 3.75 mm normal body inlet plane images at (A) 350 ms and (B) 400 ms. The top circle in both images represents a stagnant flow region and the bottom circle in both images represents a low flow region.

The flow shown in Figure 24 illustrates some cross plane flow present within the inlet port of the device. In addition to this cross plane flow, a larger region of low flow is seen along the minor orifice wall and it extends out into the middle of the port in Figure 24B.
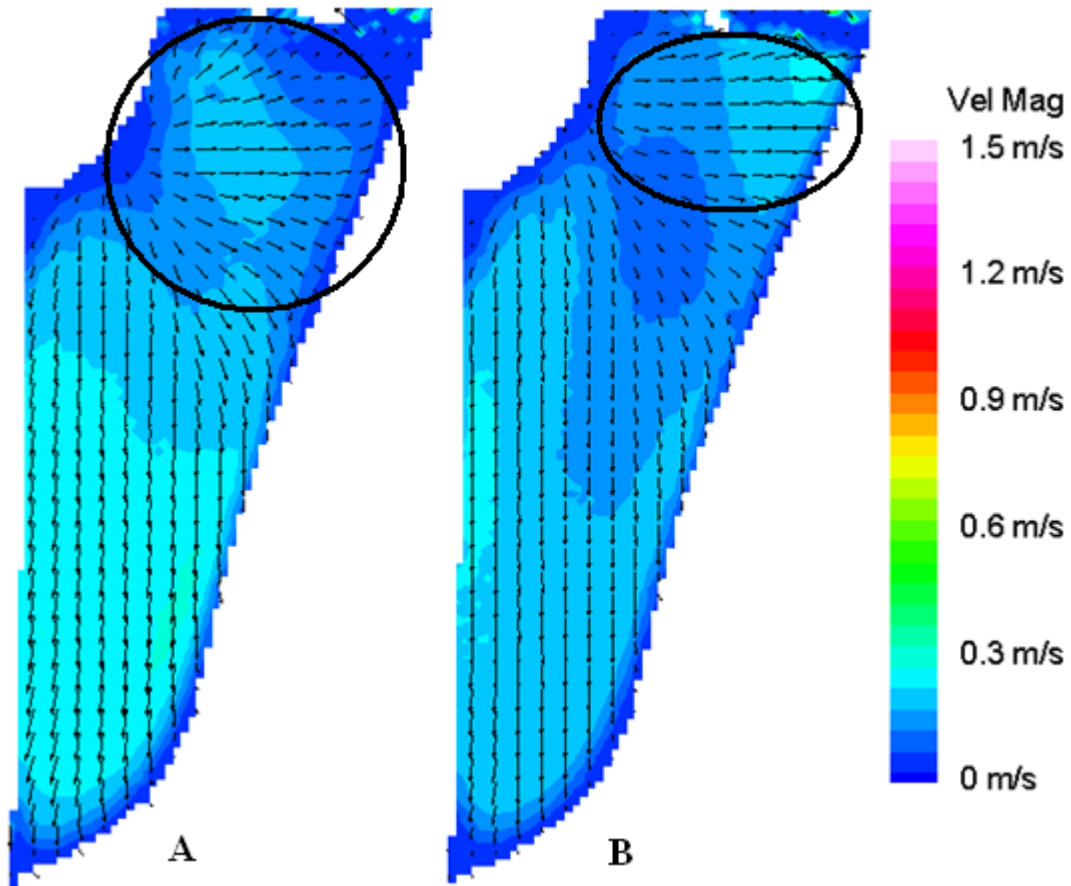
Figure 24: Inlet Port (Diastolic to Systolic Transition). These are both 3.75 mm normal body inlet plane images at (A) 450 ms and (B) 500 ms.

Figure 25 shows low flow in a few areas. However, at the top of both images, there is minor regurgitation into the inlet port. This could be caused by the diaphragm pushing into the cavity of the device, seen in Figure 25B. The low velocity flow seen towards the bottom of the device most likely has more three dimensionality with high flow toward the outlet port traveling along the surface of the diaphragm.
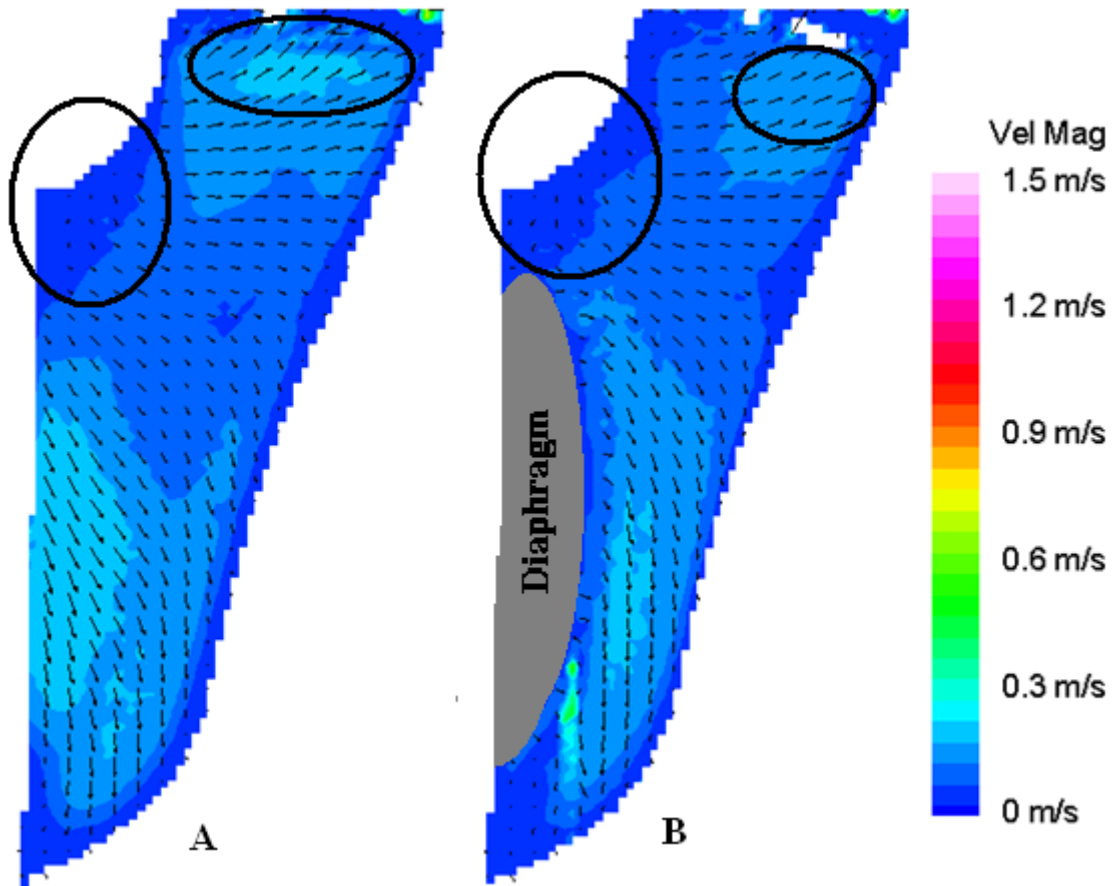
Figure 25: Inlet Port (Early Systole). These are both 3.75 mm normal body inlet plane images at (A) 550 ms and (B) 600 ms.

As expected, the diaphragm is moving further into the cavity of the PVAD and has forced the inlet valve closed, shown by the lack of flow on the inlet side of the device in Figure 26A. Little to no flow is seen at 700 ms (late systole) in the cardiac cycle as shown in Figure 26B.
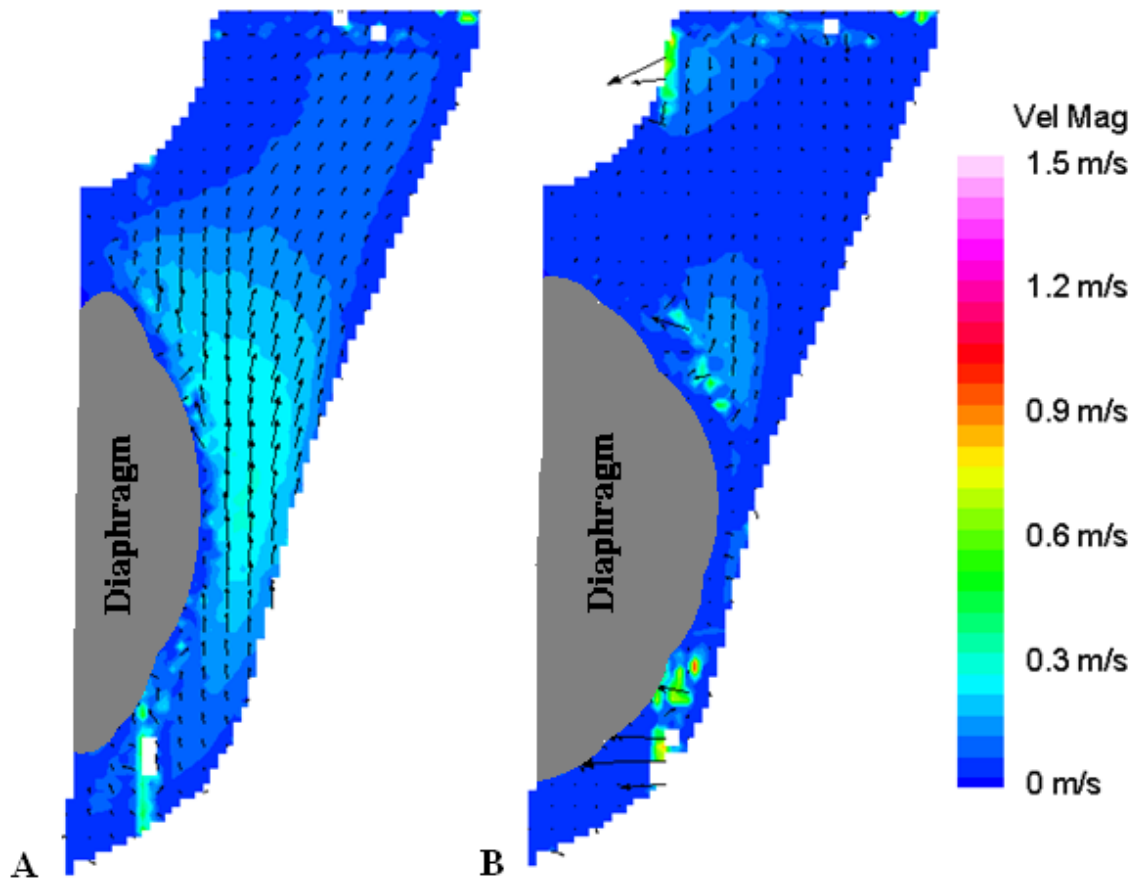
Figure 26: Inlet Port (Mid Systole). These are both 3.75 mm normal body inlet plane images at (A) 650 ms and (B) 700 ms.

As we enter late systole in Figure 27, the diaphragm has stopped pushing the fluid out of the device. Also, in Figure 27 the fluid begins to enter the device on the inlet side and the next cardiac cycle begins.
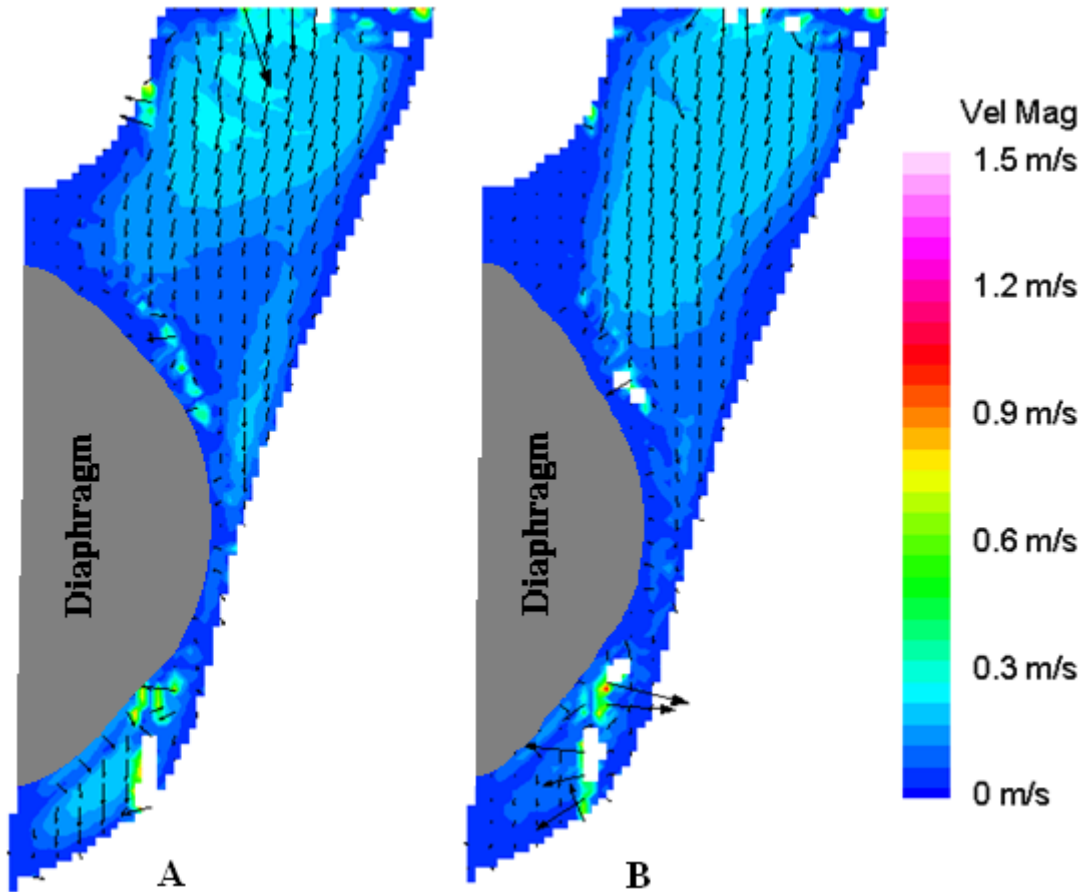
Figure 27: Inlet Port (Late Systole). These are both 3.75 mm normal body inlet plane images at (A) 700 ms and (B) 800 ms.

3.2 Flow in the Body Parallel Planes

It is clearly shown in all of the body parallel planes at the beginning of diastole that the flow is stronger toward the outside of the device where the BSM major orifice is located, as shown in Figures 28 and 29. The low flow, circled in black in Figure 28, is caused by the downstream wake of the valve. The valve within the plane, circled in red in Figure 28, is shown between the two inlet jets. There is pixilation on the outlet of the planes in Figure 28 because the inlet BSM valve creates a shadow that extends to the outlet side of the plane.
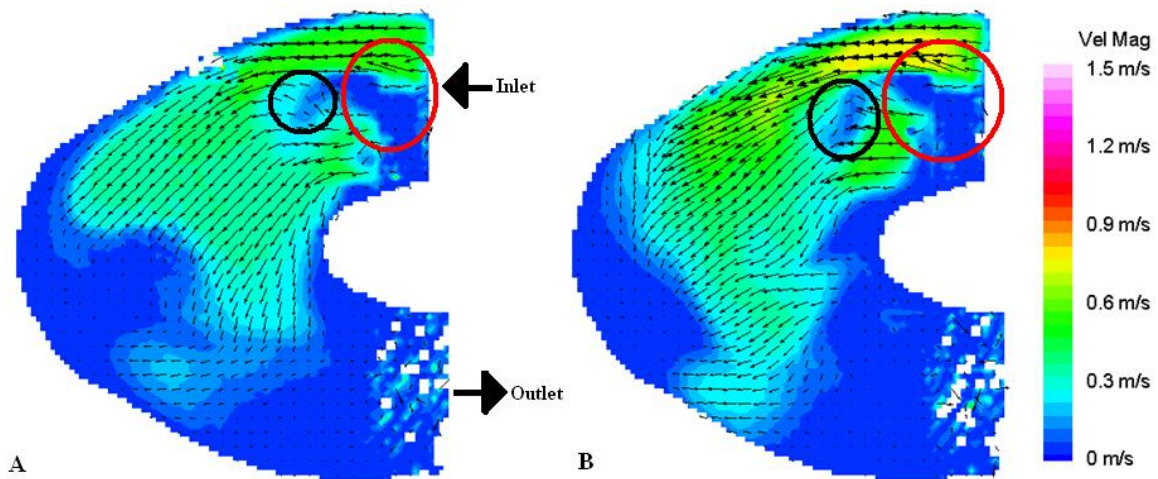
Figure 28: Body Parallel Plane 8.2 mm (Start of Diastole). These are both 8.2 mm parallel body plane images at (A) 50 ms and (B) 100 ms.

The major orifice is responsible for the jet seen on the outer edge of the device port. Another, weaker jet is formed on the inner edge of the port. The major (black circle) and minor (red circle) orifices are circled in Figure 29. The stagnant flow upstream of the minor orifice jet and the pixilation seen in the outlet are both caused by shadows cast by the open BSM valve. Therefore, we must look just downstream of that area as a guide for the flow through the minor orifice. Figure 29 shows the flow penetration to the bottom of the device as early as 100 ms in to the cardiac cycle.
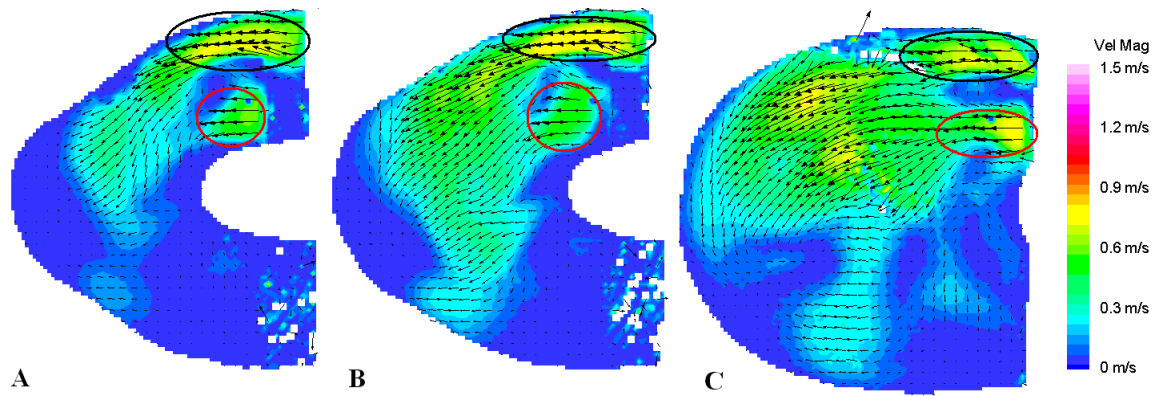
Figure 29: Major and Minor Orifice Jets. These are all parallel body planes at 100 ms. The major orifice jet is circled in black and the minor orifice jet is circled in red in each image. (A) 7.0 mm (B) 8.2 mm (C) 11.0 mm.

A low flow region can be seen in Figure 30A and 30C that was discovered earlier in the inlet normal planes. Also the velocity of the flow through the major orifice of the inlet valve has a near constant maximum of 0.75 m/s from 100 ms through 300 ms. A rotational flow is established as early as 250 ms shown by Figures 30A, 30B, and 30C. However, the 11.0 mm plane provides the best capture of the recirculatory flow because the plane shows the most body of the PVAD of the three parallel body planes.
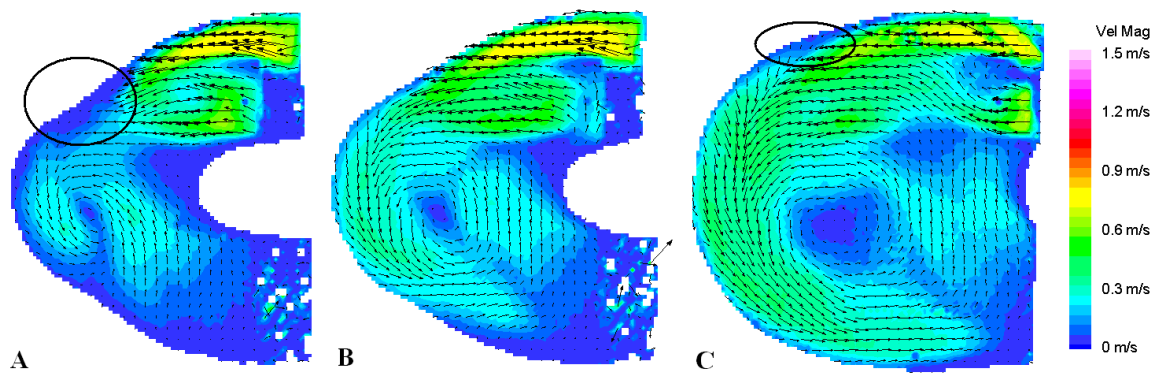

Figure 30: Low Flow Region. The low flow region is circled in black in each image. These images are at 250 ms. The planes are (A) 7.0 mm (B) 8.2 mm (C) 11.0 mm.

With this in mind, we will use the 11.0 mm body plane when looking for recirculating flow throughout the body of the device. Figure 31 shows the end of the recirculating flow that began at 200 ms and lasts through 450 ms. Figure 31 also shows two areas of low flow that exist in both displayed times of the cycle.
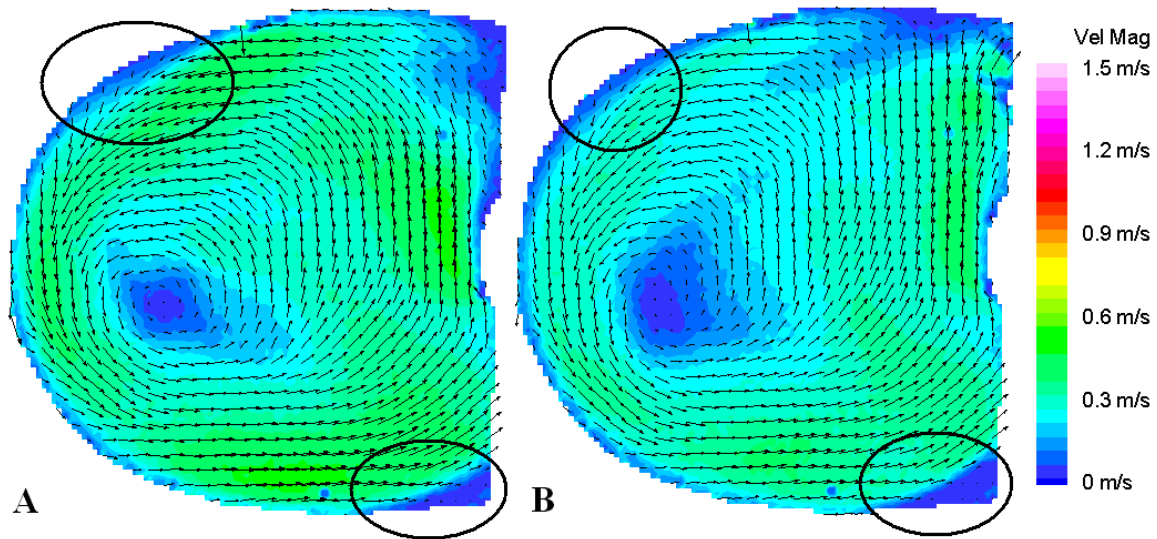

Figure 31: Recirculating Flow. These images are both from the 11.0 mm parallel body plane at times (A) 400 ms and (B) 450 ms.

As we enter early systole, the velocity of the flow becomes concentrated at the outlet of the PVAD, and the velocity is higher closer to the outside edge of the port where the BSM valve major orifice is located, reaching a maximum of 1.0 m/s, as displayed in Figure 32.
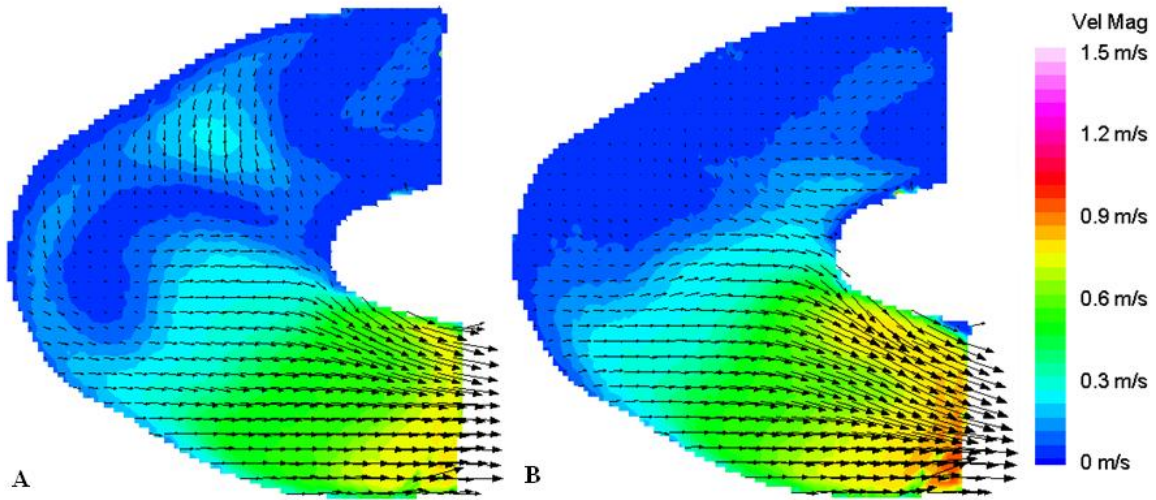
Figure 32: Body Parallel Plane 8.2 mm (Early Systole). These are both 8.2 mm parallel body plane images at (A) 550 ms (B) 600 ms.

Lastly, some regurgitation at the outlet port can be seen in all parallel body planes at the 750 ms, shown in Figure 33. The velocity in the regurgitation does not exceed 0.3 m/s. Also some fluid enters the BSM major orifice at the inlet during late systole, circled in red in Figure 33.
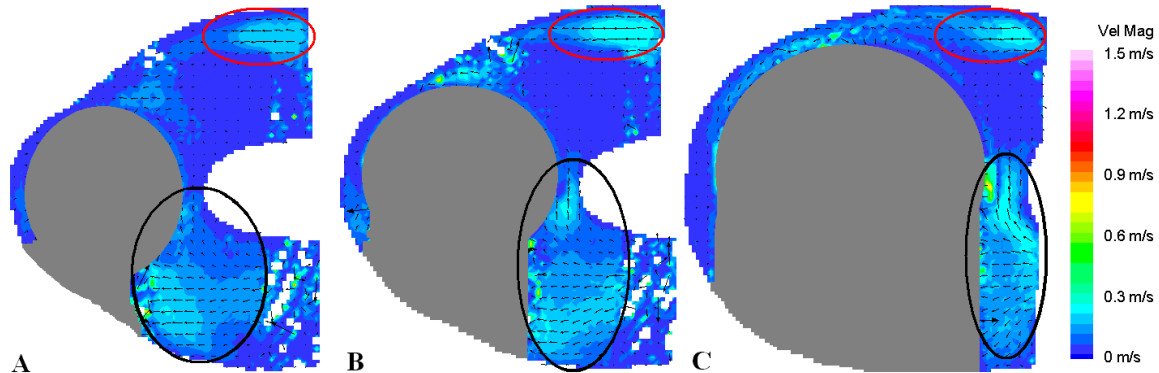

Figure 33: Regurgitation in the Parallel Body Outlet. The regurgitation regions are circled in black on the above figures. These images are all at 750ms. (A) 7 mm (B) 8.2 mm (C) 11 mm.

3.3 Flow in the Body Outlet Port

There are no remarkable features present in the start of diastole for the normal outlet planes, shown in Figure 34A. Circled in black in Figure 34B is a recirculating flow region in the normal outlet plane.
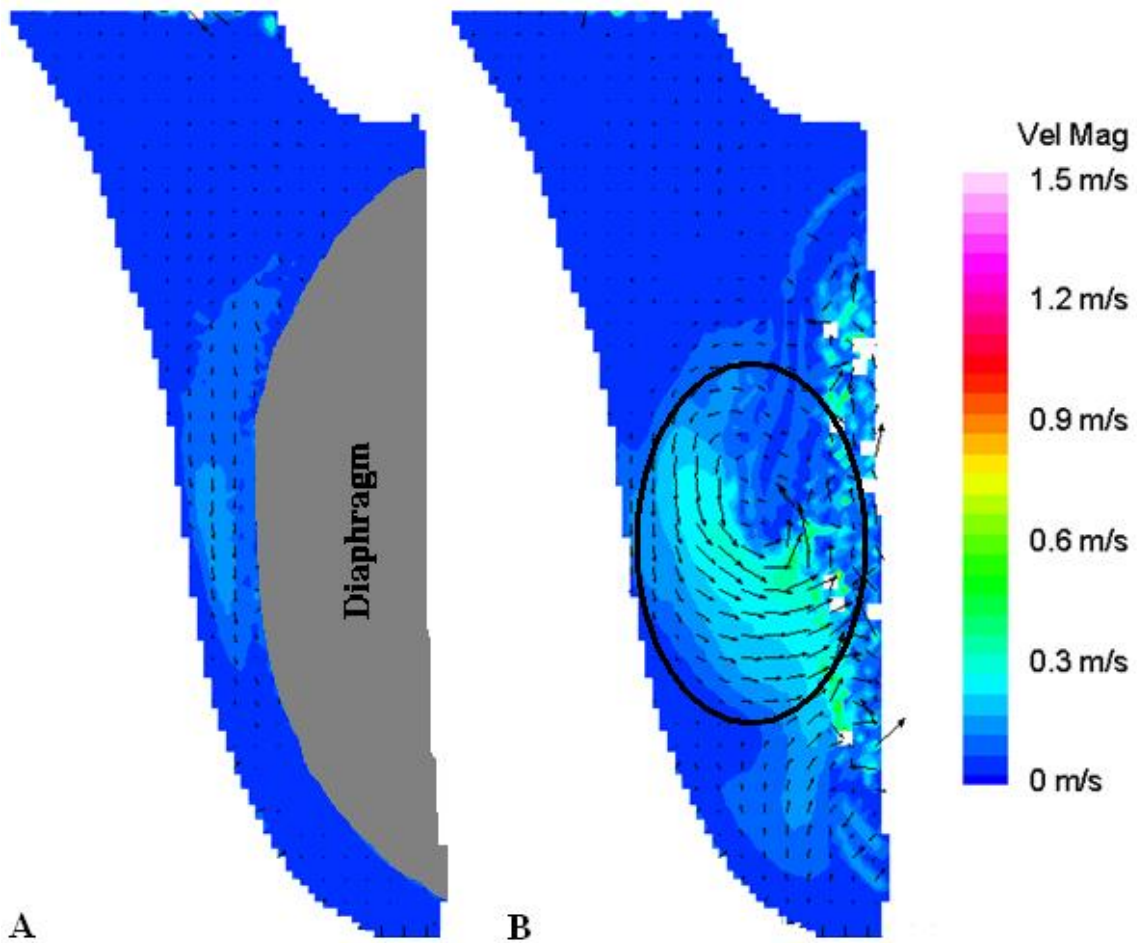

Figure 34: Outlet Port (Start of Diastole). These are both 11.25 mm normal outlet body plane images at (A) 50 ms (B) 100 ms.

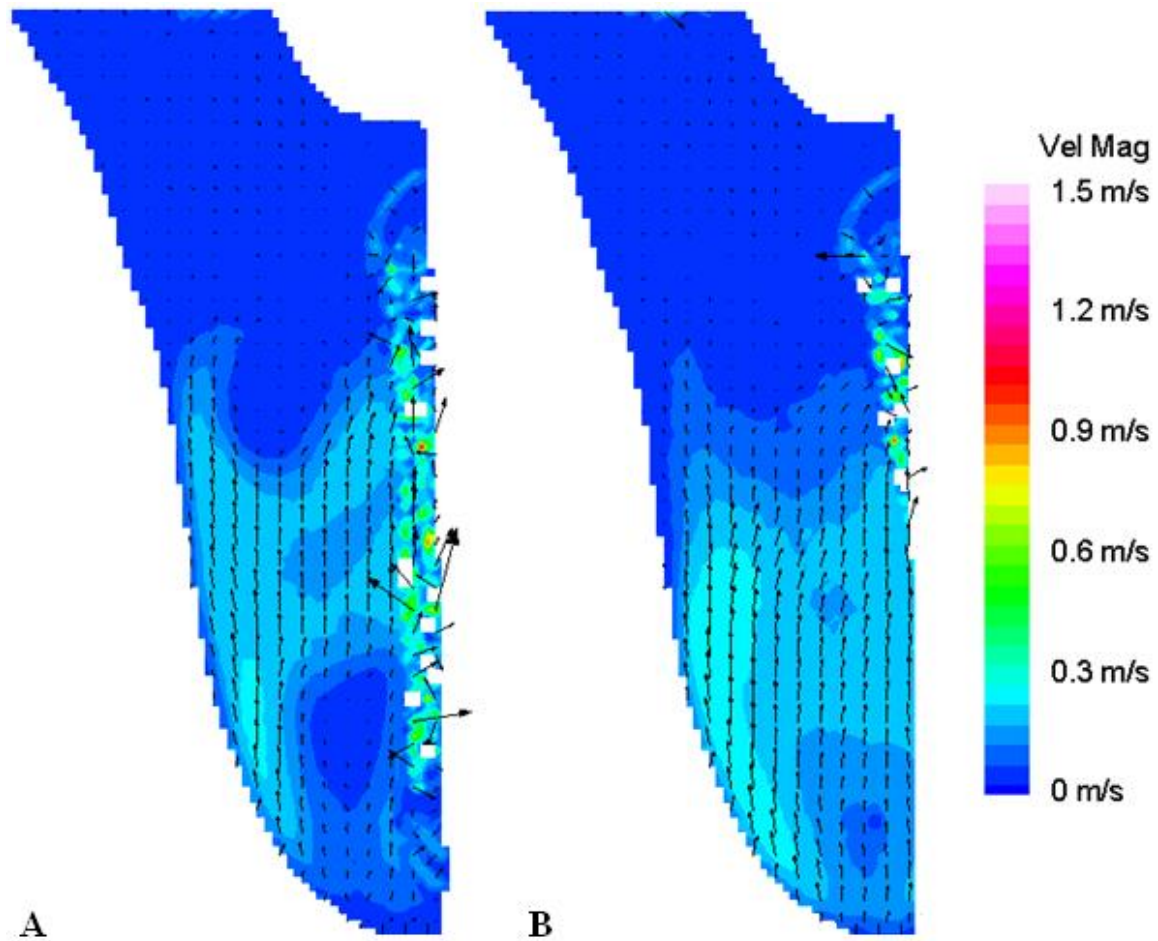Soon after this recirculatory flow appears, the inlet jet reaches the outlet side of the device, seen in Figure 35.

Figure 35: Outlet Port (Early Diastole). These are both 11.25 normal outlet body plane images at (A) 150 ms and (B) 200 ms.

There continues to be an increase in the flow within the outlet planes due to diastole. These slight increases in velocity and cross plane flow are circled in black in Figure 36. This cross plane flow brings fluid more toward the diaphragm side of the device but as it makes its way to the outlet, it is then forced away from the diaphragm side. In Figure 36B, there is part of a recirculating flow region, circled in red.
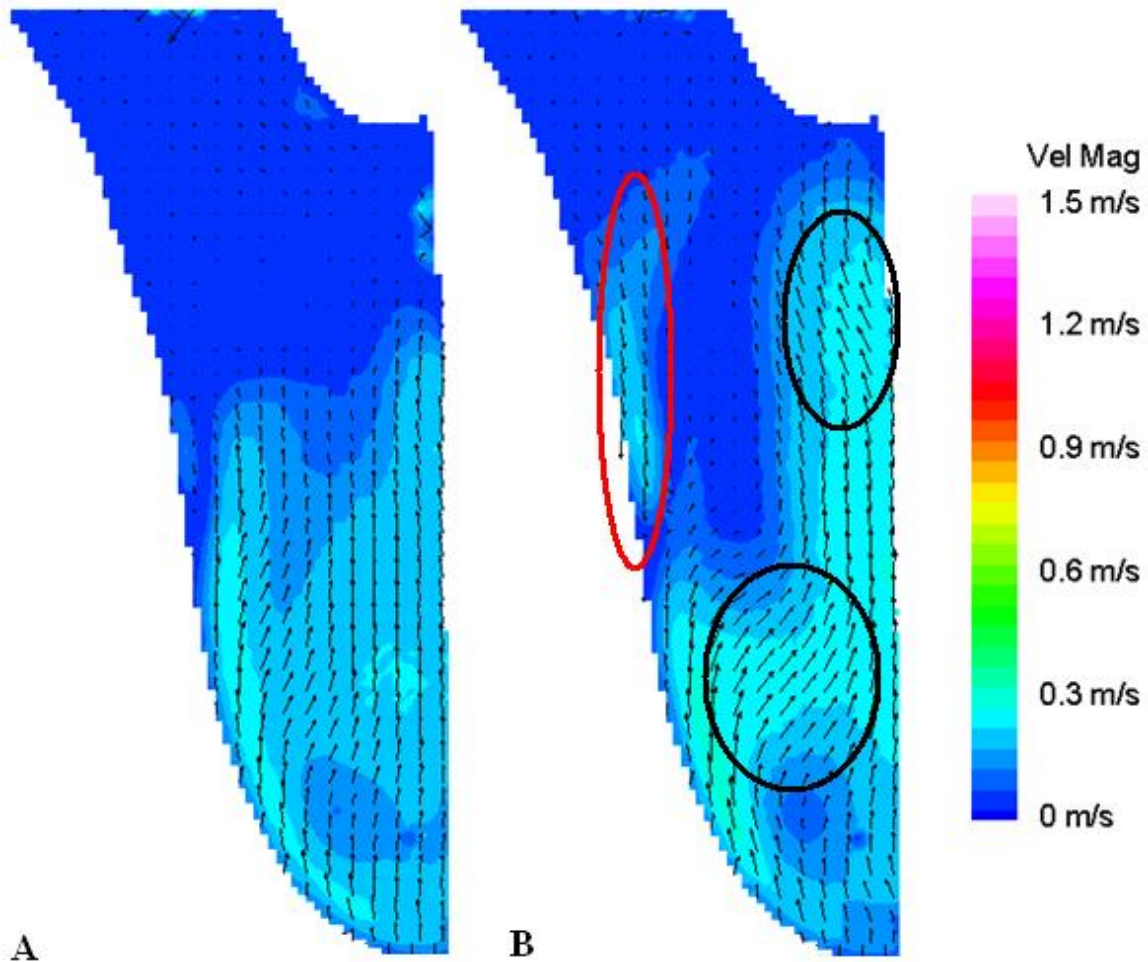

Figure 36: Outlet Port (Mid Diastole). These are both 11.25 mm normal outlet body plane images at (A) 250 ms and (B) 300 ms.

As operation of the PVAD enters late diastole, a recirculation region appears at 400 ms and is circled in black in Figure 37B.
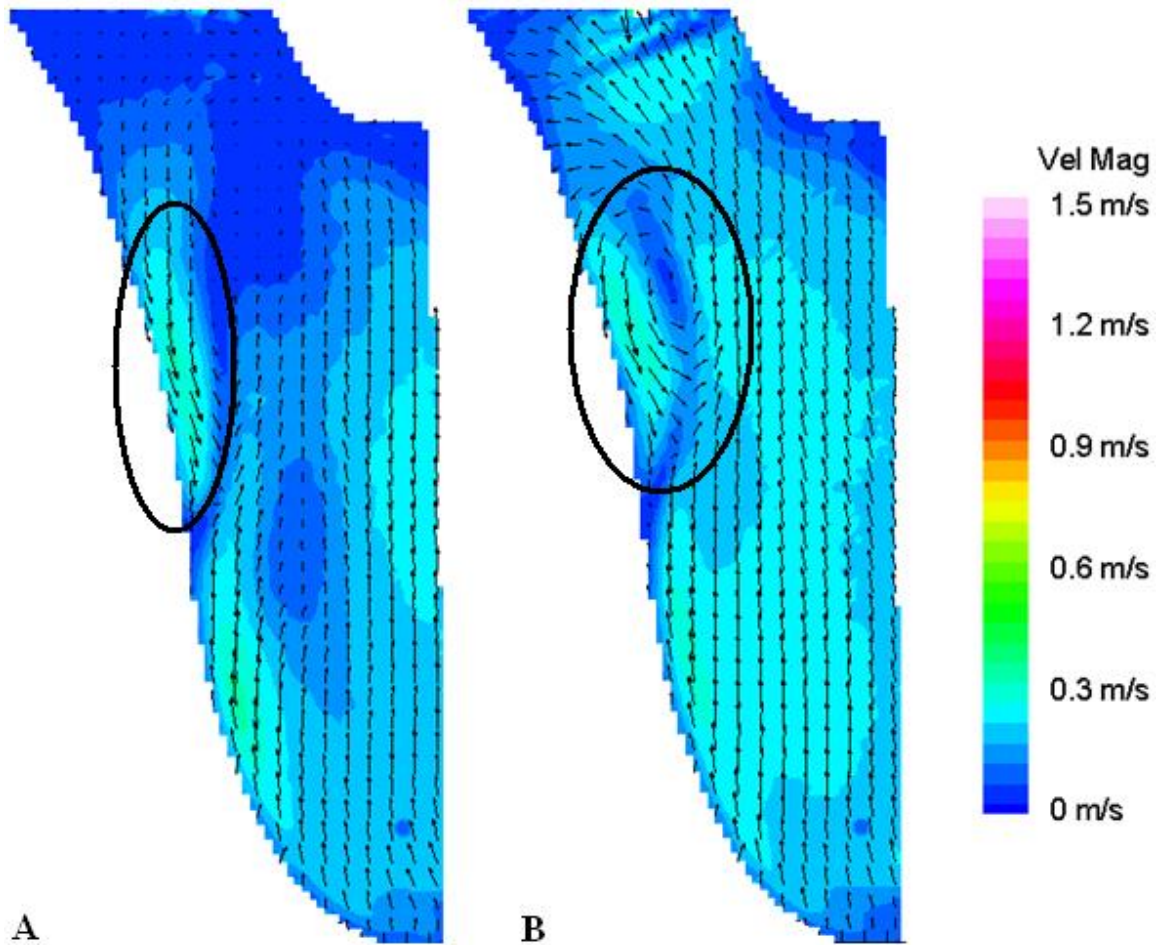

Figure 37: Outlet Port (Late Diastole). These are both 11.25 mm normal outlet body plane images at (A) 350 ms and (B) 400 ms.

The recirculation region lasts to 450 ms and is circled in pink in Figure 38A. A stagnant flow region is below the recirculation region at 450 ms, circled in red in Figure 38A. By 500 ms the flow is uniform and exiting the outlet port, shown in Figure 38B. As the recirculation region disappears, it leaves a stagnant flow region in its absence, circled in red in Figure 38B. Also there is a region of stagnant flow present upstream of the outlet, circled in yellow in Figure 38A, which is eliminated at 500 ms, seen in Figure 38B. The third stagnant flow region in Figure 38A, circled in black at the bottom of the image, grows in size as diastole transitions to systole, circled in black in Figure 39A and 39B.
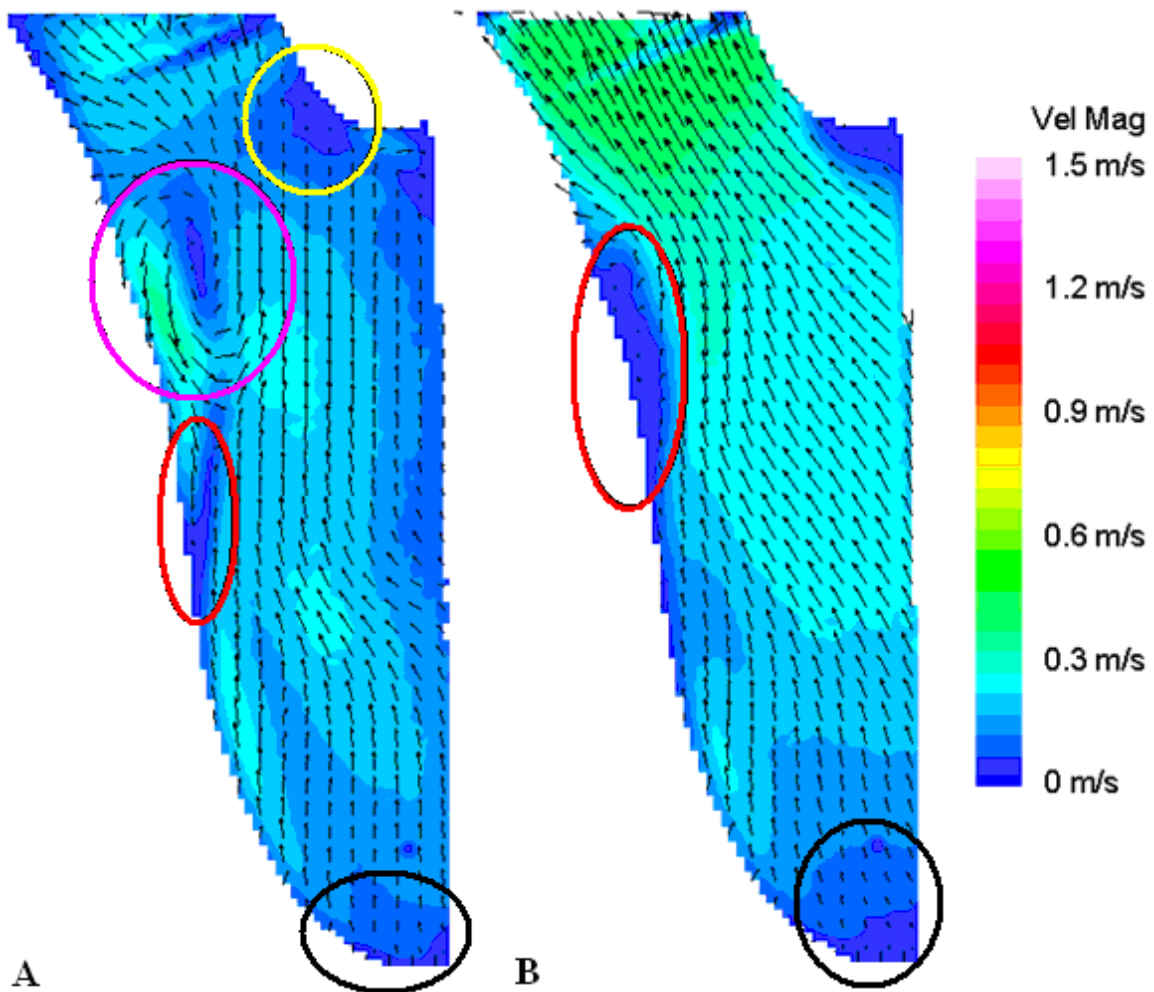

Figure 38: Outlet Port (Diastolic to Systolic Transition). These are both 11.25 mm normal outlet body plane images at (A) 450 ms and (B) 500 ms.

The flow peaks at 600ms at a velocity of 1.1 m/s, as shown in Figure 39. Also the stagnant flow region at the bottom of the plane grows in size from 600 ms to 650 ms.
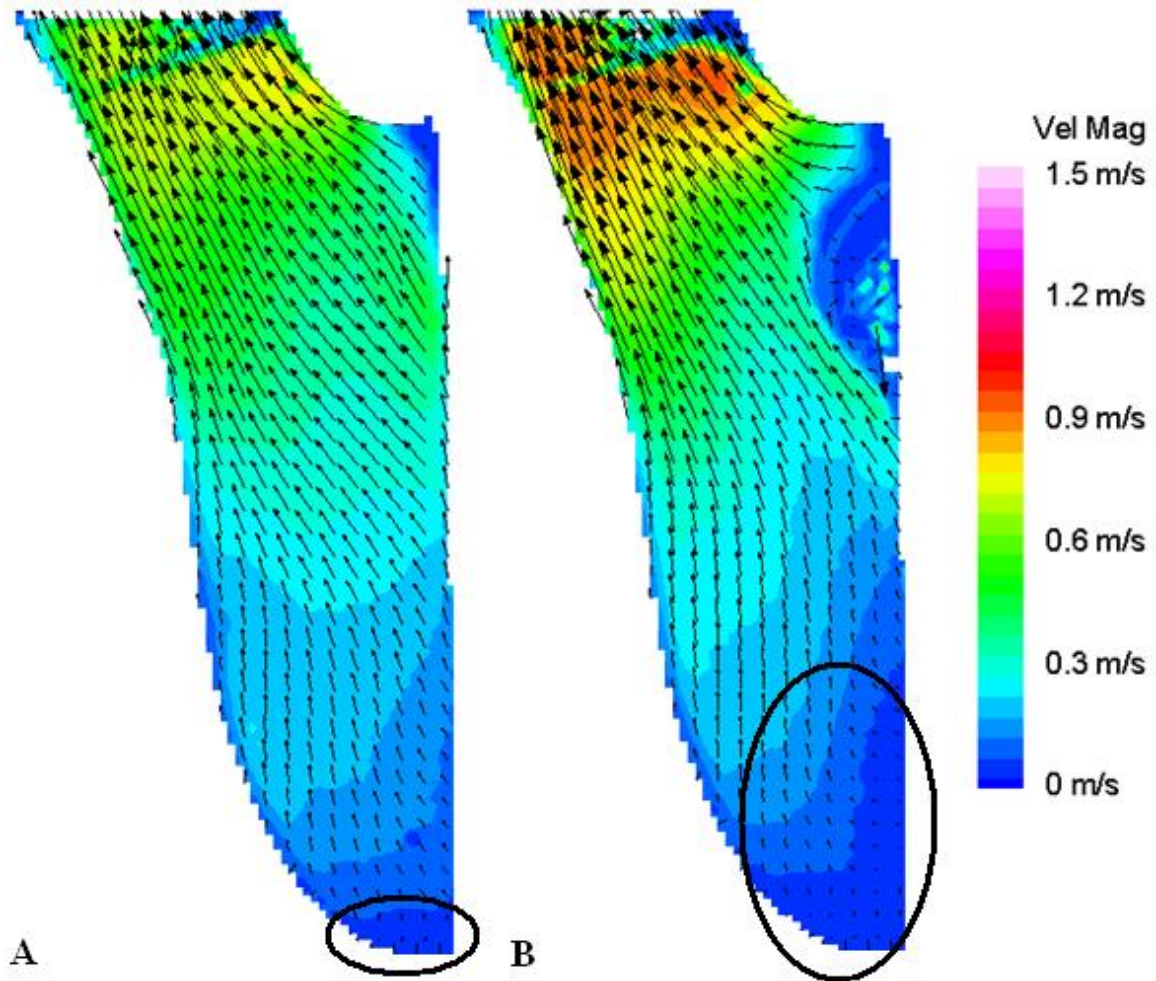

Figure 39: Outlet Port (Early Systole). These are both 11.25 mm normal outlet body plane images at (A) 550 ms and (B) 600 ms.

After peak systole at 600 ms, the flow velocity decreases (at 650 ms) and then the outlet port experiences outflow on the sides of the port and retrograde flow in the center of the port, circled in black in Figure 40. The backflow does not have velocities larger than 0.3 m/s.
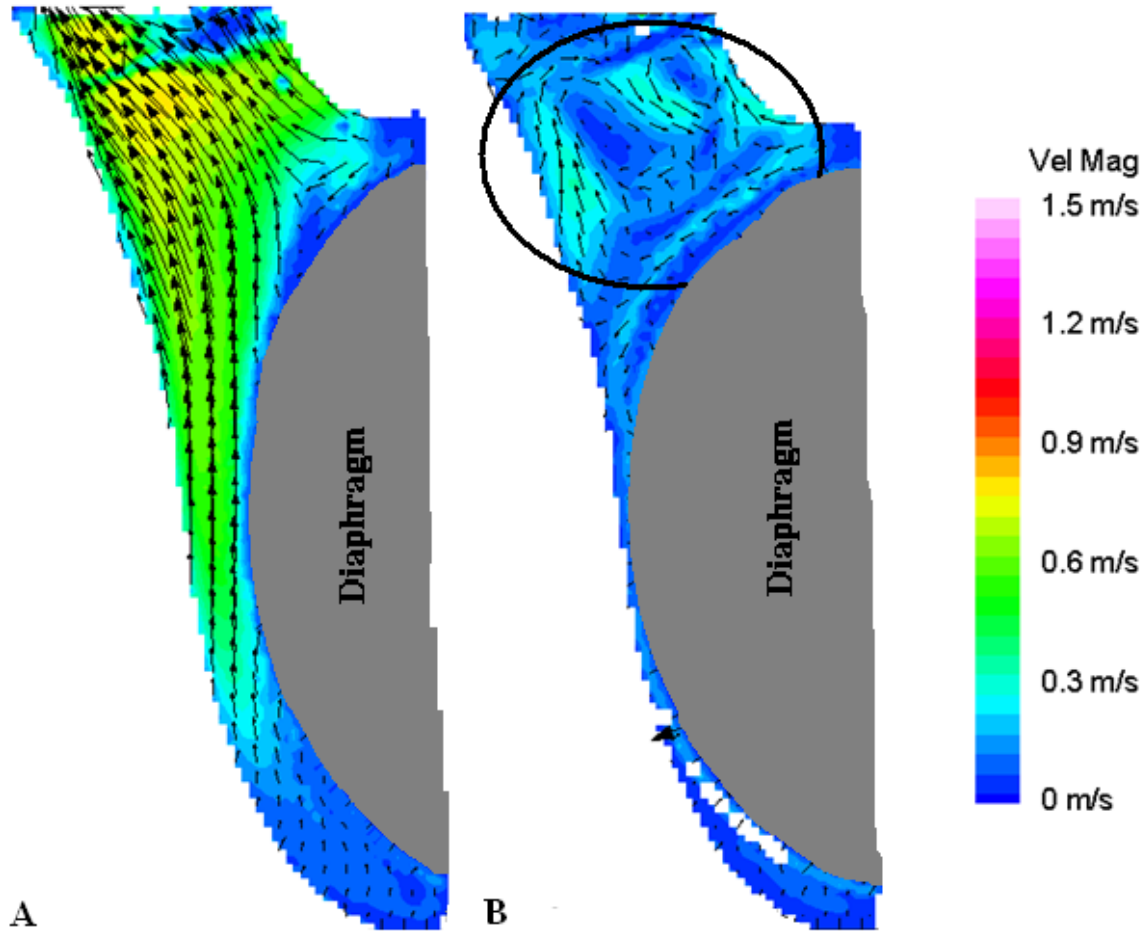

Figure 40: Outlet Port (Mid Systole). These are both 11.25 mm normal outlet body plane images at (A) 650 ms and (B) 700 ms.

Figure 41 shows late systole and a large regurgitant jet, circled in Figure 41A, enter the model from the outlet port in the 11.0 mm plane. This is not seen at 800 ms for the 7.5 mm normal body plane.
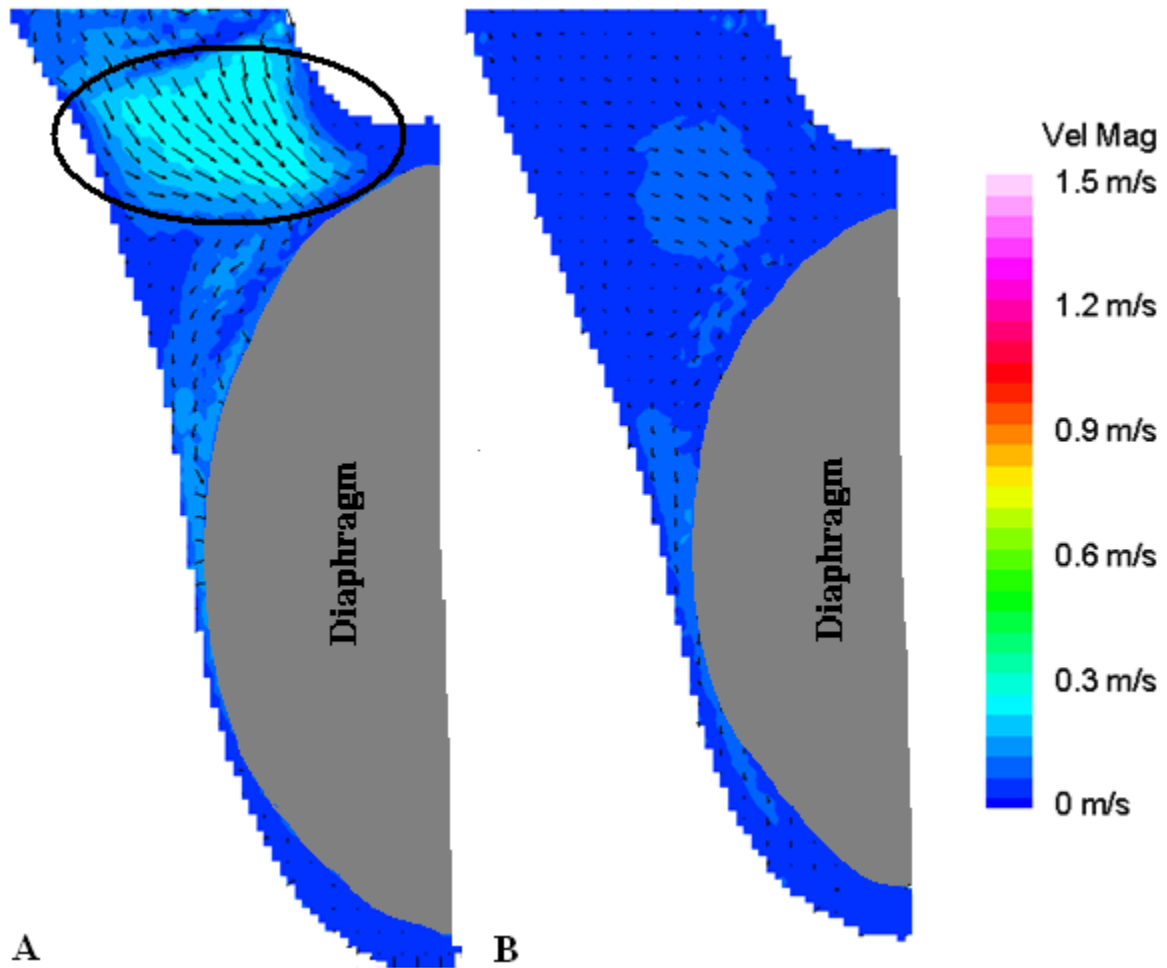

Figure 41: Outlet Port (Late Systole). These are both normal outlet body plane images with locations and time steps (A) 11.25 mm 750 ms and (B) 7.5 mm 800 ms.

Chapter 4

DISCUSSION

4.1 Outlet Blockage Flow Comparison

The change in flow within the outlet port of the PVAD has significantly changed with the addition of the outlet extension. Figure 42 shows outlet normal planes at the peak of systole with black lines drawn to show the line of data points that represent the velocity plots in Figure 43.
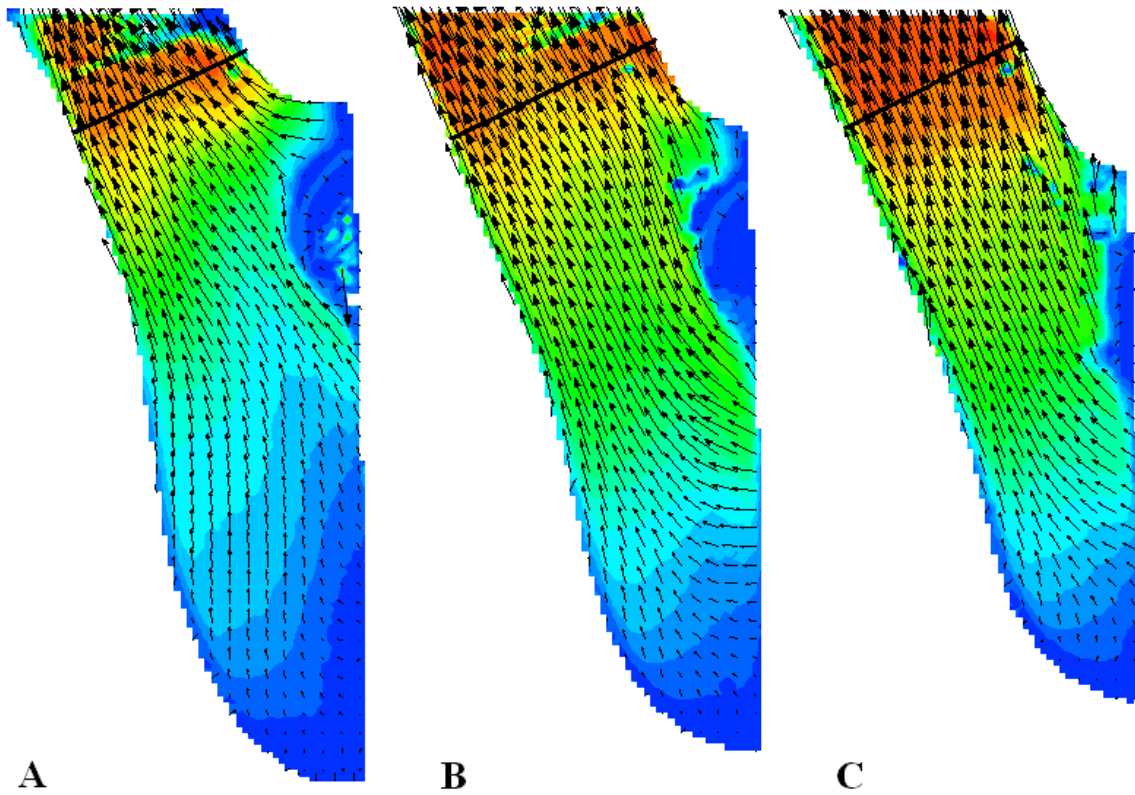

A **B** **C**

Figure 42: Line Plot Lines for Body Normal Outlet Planes (A) 11.25 mm (B) 7.5 mm (C) 3.75 mm.

Figure 43 shows the velocity locations along the outlet port for each of the body normal outlet planes. The velocity within the outlet does not vary more than 1.25 m/s throughout the length of the port. The lack of peaks or valleys present within the graph shows that the separation region is not apparent in the outlet port of the device with the extension.
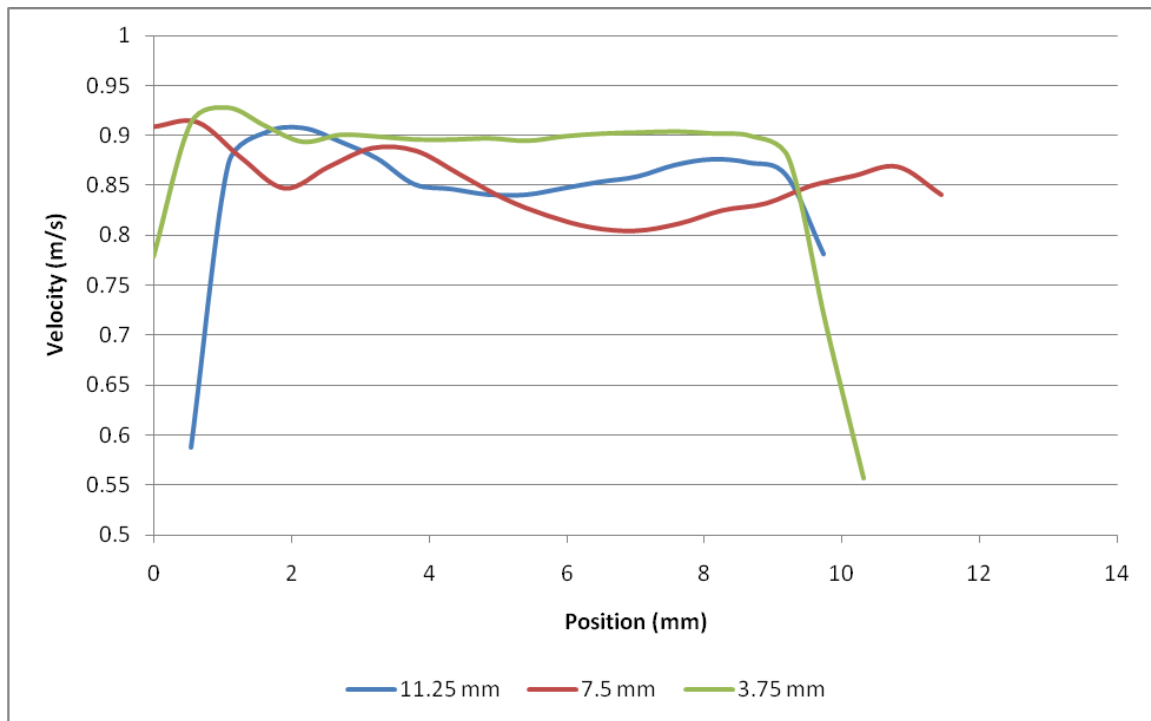

Figure 43: Velocity Line Plots for Body Normal Outlet Planes: 11.25 mm (blue line), 7.5 mm (red line), and 3.75 mm (green line).

Figure 44 displays the flow within the parallel body planes at 600ms. Figure 45 shows the same planes within the experiment conducted by Roszelle et al. (Roszelle 2010). The blockage region is circled in pink in Figure 45C. The black lines in the outlet portion of each image in Figures 44 and 45 show the lines used to extract and plot the velocity profiles shown in Figures 46, 47, and 48, where the red line will represent flow velocity in the PVAD and the blue line will represent flow in the PVAD with the outlet extension
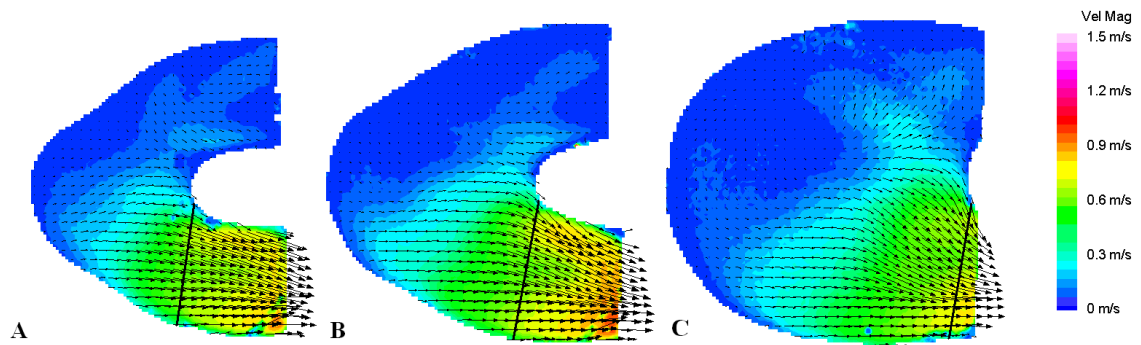

Figure 44: Parallel Body Planes from PVAD with extension. All images were from 600 ms. (A) 7.0 mm. (B) 8.2 mm. (C) 11.0 mm.
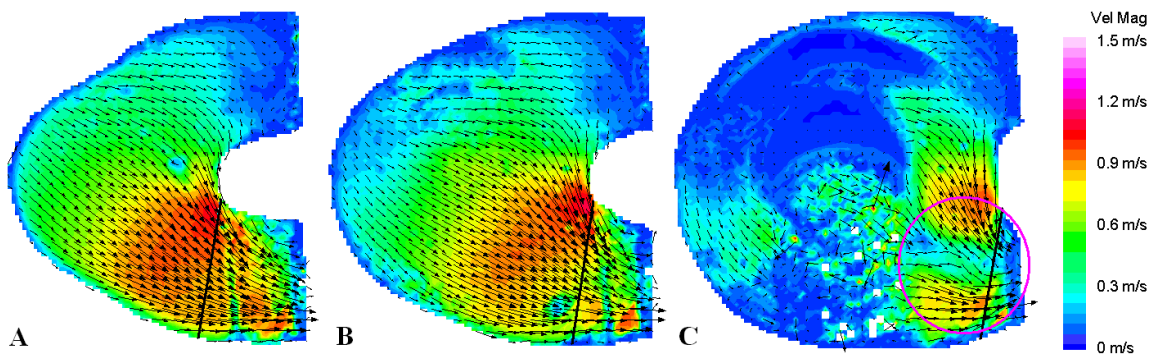

Figure 45: Parallel Body Planes from PVAD without extension. All images were from 650 ms. (A) 7.0 mm. (B) 8.2 mm (C) 11.0 mm.

The velocity within the 7.0 mm body plane depicted in Figure 46 shows that the velocity

has a range similar to the PVAD without the extension but with overall lower flow.
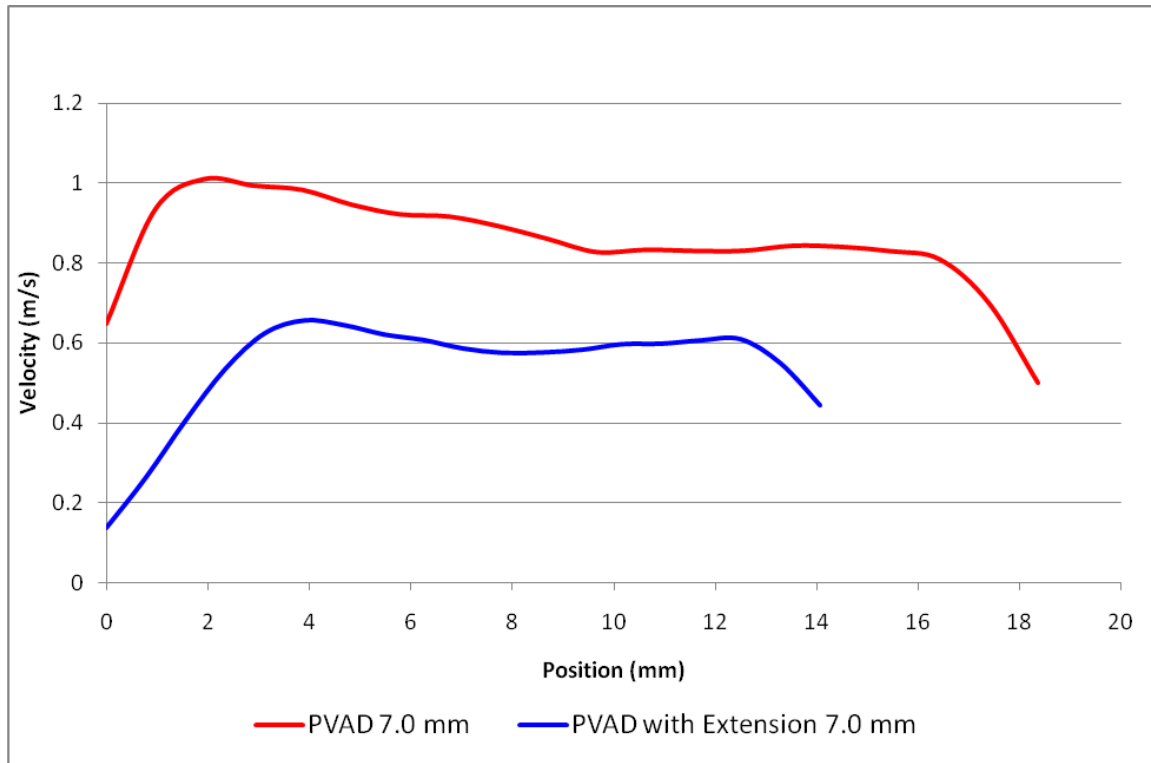

Figure 46: Body Parallel 7.0 mm Outlet Velocity Profile Comparison between the PVAD (red line) and the PVAD with extension (blue line).

In Figure 47, the 8.2 mm body parallel plane for the PVAD with the extension does not change as much throughout the port for the PVAD alone. The velocity changes 0.25 m/s throughout the length of the port for the PVAD alone and changes about 0.1 m/s for the device with the extension.
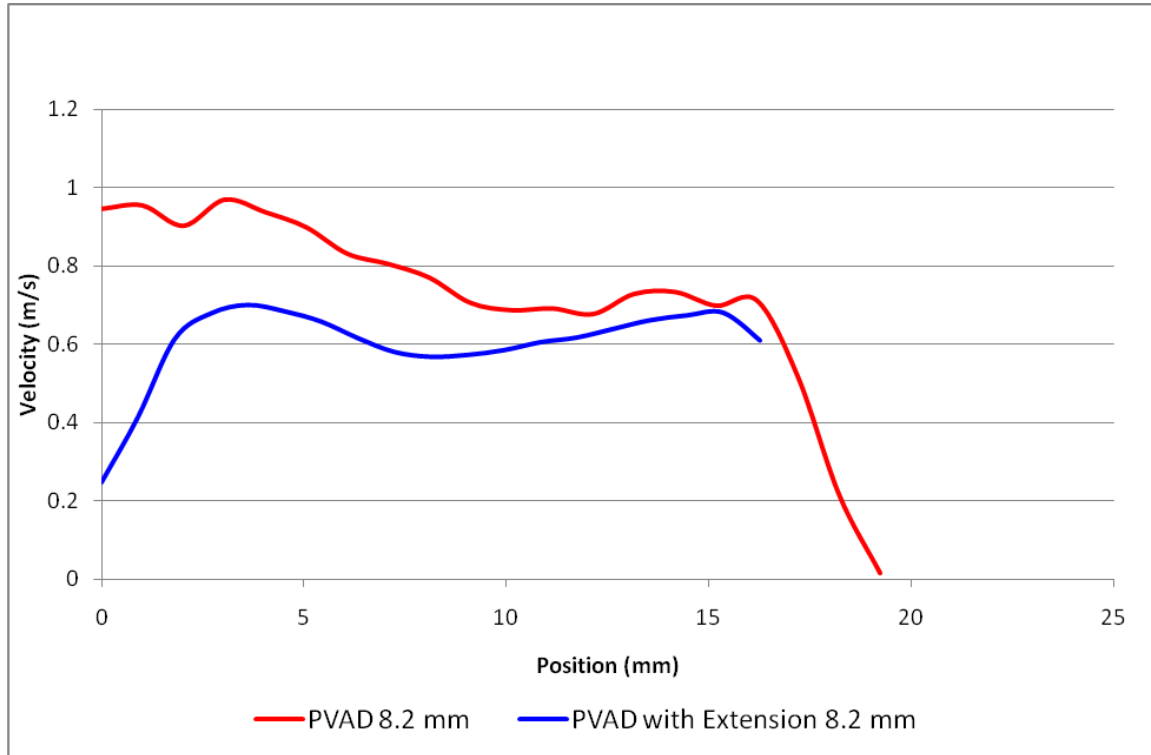

Figure 47: Body Parallel 8.2 mm Outlet Velocity Profile Comparison between the PVAD (red line) and the PVAD with extension (blue line).

Of all the parallel body planes, the 11.0 mm plane shows the greatest difference between the PVAD alone and the device with the outlet extension, shown in Figure 48. The PVAD alone has a velocity range from around 0.2 m/s to almost 0.9 m/s along the length of the outlet port. The relative minimum in the graph at 6.5 mm followed by the peak at 12 mm shows this drastic change in flow velocity, which is indicative of the blockage region. The PVAD with the extension, however, only shows flow velocities ranging from 0.6 m/s to 0.75 m/s across the entire cross section of the port.
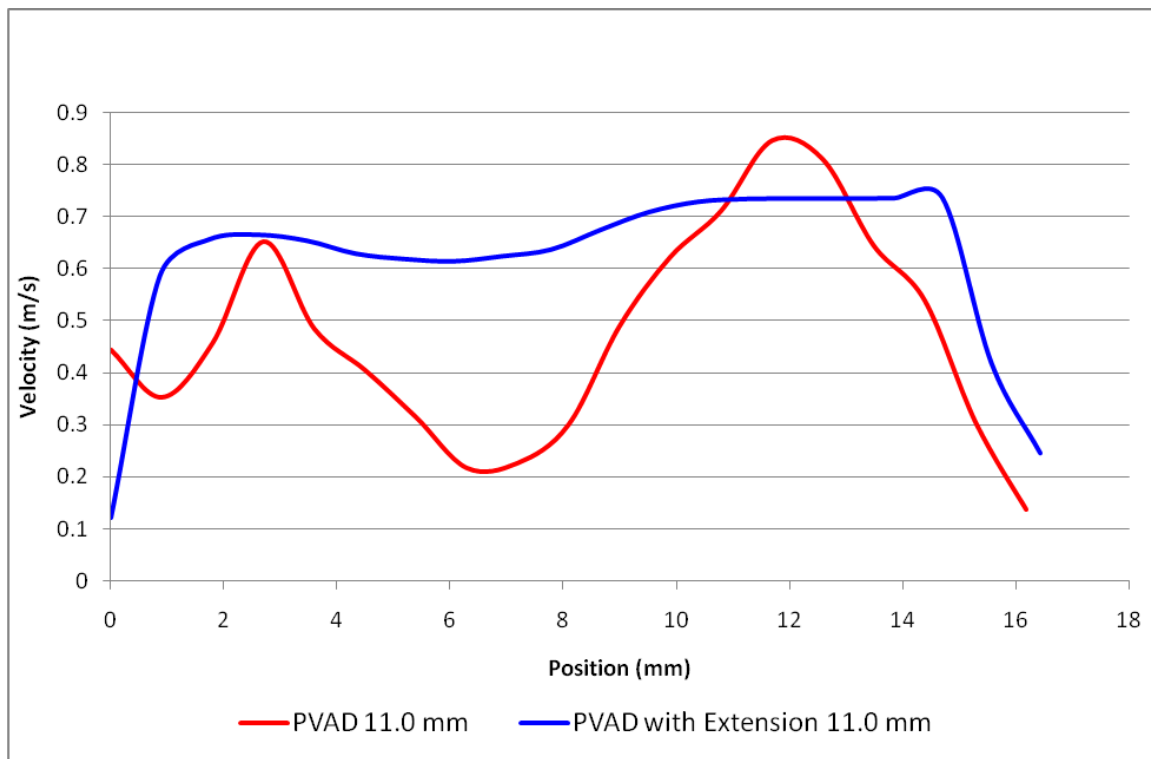

Figure 48: Body Parallel 11.0 mm Outlet Velocity Profile Comparison between the PVAD (red line) and the PVAD with extension (blue line).

It is evident that the velocity does not change drastically during the length of the outlet port of the PVAD with the extension. This constant velocity across the outlet greatly decreases the probability of blood damage in this region of the device.

Chapter 5

CONCLUSION

5.1 Conclusions

Observations of the flow within the PVAD, after the displacement of the BSM valve two inches away from the PVAD, were made for the first time. Important elements of the flow seen in previous experiments, using the BSM valve in the 12cc Penn State PVAD, were seen again including rotational flow, the flow penetration of the bottom of the device, and recirculatory flow upstream of the outlet in late diastole. The most noticeable areas of concern in the flow were the recirculation region upstream of the outlet and stagnant flow regions along the bottom of the device on the inlet. Also data was gathered on flow within the outlet extension and the flow upstream of the inlet BSM valve which was not discussed in this thesis.

After data analysis, line plots showed flow uniformity within the outlet port of the PVAD and the elimination of the outlet blockage region was most strongly supported by the 11.0 mm body parallel plane with the outlet extension attached.

5.2 Future Studies

As shown by Roszelle et al., the 15° degree angle valve orientation in both the inlet and outlet valve of the PVAD shows better flow throughout but a larger blockage region. The use of this new valve orientation with the extension may improve the overall function of the device (Roszelle 2010).

Also, when preparing pulsatile devices, patients must be weaned from the device. This is usually accompanied by lower flow rates, which in the case explored by Roszelle et al., rotational flow is lost earlier, blood residence time is increased, and an overall reduction in wall shear rates at the outer walls (Roszelle 2008). Even though weaning with the extension was not investigated in this experiment, it should be considered as a future experiment for this model.

References

1. American Heart Associate: *Statistic Reference Book*, Texas, 2005.

2. Bachmann C, Hugo G, Rosenberg G, Deutsch S, Fontaine A, Tarbell JM: Fluid dynamics of a pediatric ventricular assist device *Artificial Organs* 25:362-372, 2000.

3. Baldwin JT, Borovetz HS, Duncan BW, Gartner MJ, Jarvik RK, Weiss WJ, Hoke TR. The National Heart, Lung, and Blood Institute Pediatric Circulatory Support Program. *Circulation* 2006;113:147-155.

4. Baldwin JT, Deutsch S, Geselowitz DB, Tarbell JM. 1994. LDA measurements of mean velocity and Reynolds stress fields within an artificial heart ventricle. *J. Biomech. Eng.* 116:190-200.

5. Berlin Heart® : Excor® VAD with Stationary Driving Unit Ikus. Berlin, Berlin Heart AG, 2004.

6. Black MD, Coles JG, Williams WG, Rebeyka IM, Trusler GA, Bohn D, Gruenweld C, Freedom RM. Determinants of successes in pediatric cardiac patients undergoing extracorporeal membrane oxygenation. *Ann Thorac Surg* 1995 60: 133-138.

7. Cooper BT, Roszelle BN, Long T, Manning KB, Deutsch S: The 12 cc Penn State pulsatile pediatric ventricular assist device: fluid dynamics associated with valve selection. *J Biomech Eng* 130:2008.

8. Daily BB, Pettitt TW, Sutera SP, Pierce WS. Pierce-Donachy pediatric VAD: Progress in development. *Ann Thorac Surg* 1996;61:437-43.

9. Deutsch S, Tarbel JM, Manning KB, Rosenberg G, Fontaine AA. Experimental Fluid Mechanics of Pulsatile Artificial Blood Pumps. *Annu Rev Fluid Mech* 2006;38:65-86.

10. ECMO System http://emedicine.medscape.com/article/904996-overview.

11. Gharib M, Pereira F, Dabiri D, Hove JR, Modarress D; Quantitative Flow Visualization: Toward a Comprehensive Flow Diagnostic Tool. *Integr Comp Biol*. 2002 42: 964-970.

12. Goldstein DJ, Zucker M, Arroyo L, Baran D, McCarthy PM, Loebe M, Noon GP. Safety and feasibility trial of the MicroMed DeBakey ventricular assist device as a bridge to transplantation. J. American College Cardiology. 45(6): 962-963, 2005.

13. Hanson SR: Device thrombosis and thromboembolism *CardioVasc Pathol* 2:157S-165S, 1993.

14. Hart DP: Super-Resolution PIV by Recursive Local-Correlation *Journal of Visualization,* The Visualization Society of Japan, Vol. 10, 1999

15. Health Resources and Services Administration, Healthcare Systems Bureau, Division of Transplantation, Annual Report of the U.S. Organ Procurement and Transplantation Network and the Scientific Registry of Transplant Recipients: Transplant Data 1996-2005, Maryland, 2006.

16. Hochareon P, Manning KB, Fontaine AA, Tarbell JM, Deutsch S. Correlation of in vivo clot deposition with the flow characteristics in the 50cc penn state artificial heart: a preliminary study. *ASAIO J.* 2004 Nov-Dec;50(6):537-42. (1)
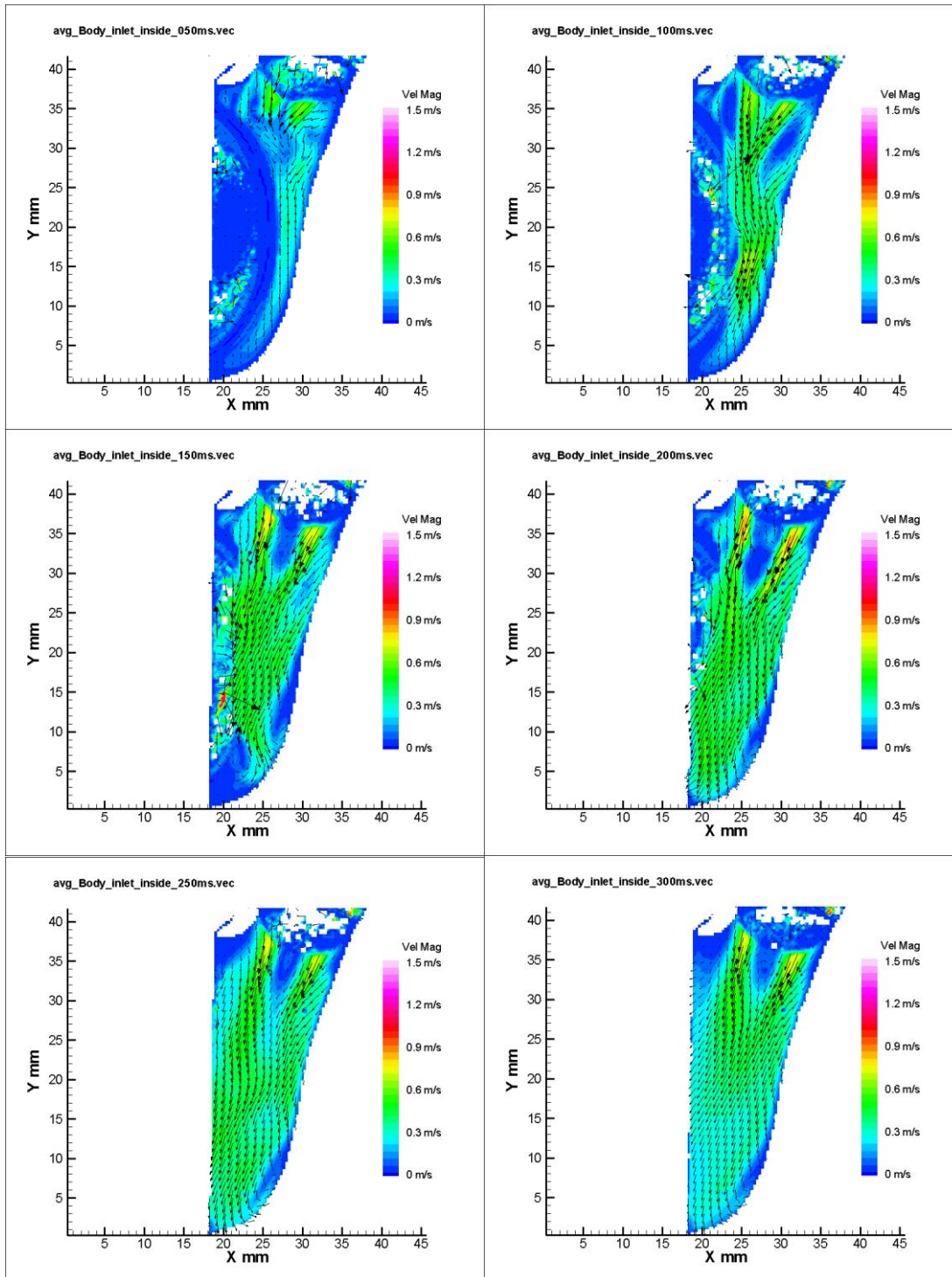
17. Hochareon P, Manning KB, Fontaine AA, Tarbell JM, Deutsch S. Fluid dynamic analysis of the 50cc Penn State artificial heart under physiological operating conditions using particle image velocimetry. *J Biomech Eng.* 2004 Oct;126(5):585-93. (2)

18. Hubbell JA, McIntire LV. Visualization and analysis of mural thrombogenesis on collage, polyurethane and nylon. *Biomaterials* 1986 7:354-363.

19. Karl TR and Horton B: Options for Mechanical Support in Pediatric Patients, in Goldstein DJ and Oz MC (eds) Cardiac Assist Devices, New York, Futurea Publishing Co, 2000, pp. 37-62.

20. Kawahito S, Maeda T, Motomura T, Ishitoya H, Takano T, Nonaka K, Linneweber J, Ichikawa S, Kawamura M, Hanazaki K, Glueck J, Nose Y. Hemolytic characteristics of oxygenators during clinical extracorporeal membrane oxygenation. *ASAIO J.* 2002;48(6):636-9.

21. Lamson TC, Rosenberg G, Geselowitz DB, Deutsch S, Stinebring DR, Frangos JA, and Tarbell JM: Relative blood damage in the three phases of a prosthetic heart valve flow cycle *ASAIO J* 39: M626-M633, 1993.

22. Long JA, Undar A, Manning KB, and Deutsch S: Viscoelasticity of pediatric blood and its implications for the testing of a pulsatile pediatric blood pump *ASAIO J* 51:563-566, 2005.

23. Manning KB, Wivholm BD, Yang N, Fontaine AA, Deutsch S: Flow behavior within the Penn State 12cc pulsatile pediatric ventricular assist device: an experimental study of the initial design. *Artificial Organs* 32:442-452, 2008.
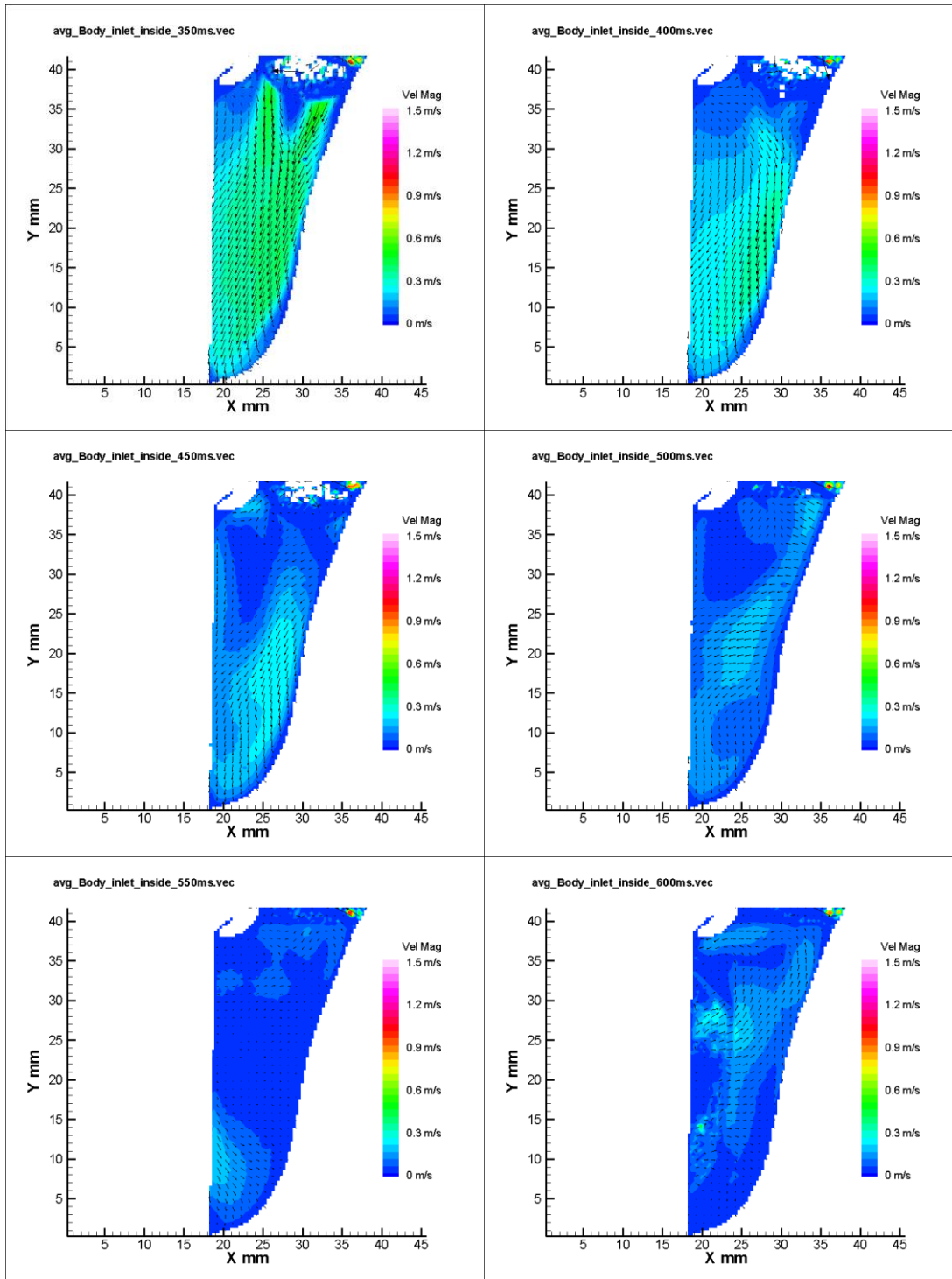
24. Potapov EV, Stiller B, Hetzer R. Ventricular assist devices in children Current achievements and future perspectives.Pediatr Transplantation 2007: 11: 241–255.

25. Raffel M, Willert CE, Kompenhans J: Particle Image Velocimetry: A Practical Guide. Berlin, Springer-Verlag, 1998.

26. Reinhartz O, Stiller B, Eilers R, Farrar DJ. Current clinical status of pulsatile pediatric support. ASAIO J. 48:455-459, 2002.

27. Rose EA, Gelijns AC, Moskowitz AJ, Heitjan DF, Stevenson LW, Dembitsky W, Long JW, Ascheim DD, Tierney AR, Levitan RG, Watson JT, Meier P, Ronan NS, Shapiro PA, Lazar RM, Miller LW, Gupta L, Frazier OH, Desvigne-Nickens P, Oz MC, Poirier VL; Randomized Evaluation of Mechanical Assistance for the Treatment of Congestive Heart Failure (REMATCH) Study Group. Long-term use of a left ventricular assist device for end-stage heart failure. *N Engl J Med.* 2001 Nov 15;345(20):1435-43.

28. Rosenberg G: A mock circulatory system for in vitro studies of artificial hearts, The Pennsylvania State University, 1972.

29. Roszelle, BN. Flow Visualization of Three-Dimensionality Inside the 12 cc Penn State Pulsatile Pediatric Ventricular Assist Device. *Annals of Biomedical Engineering*, Accepted 2010. (1)

30. Roszelle, BN: An Investigation of Three-Dimensionality in the Penn State Pulsatile Pediatric Ventricular Assist Device Masters Thesis, Penn State University, 2008. (2)
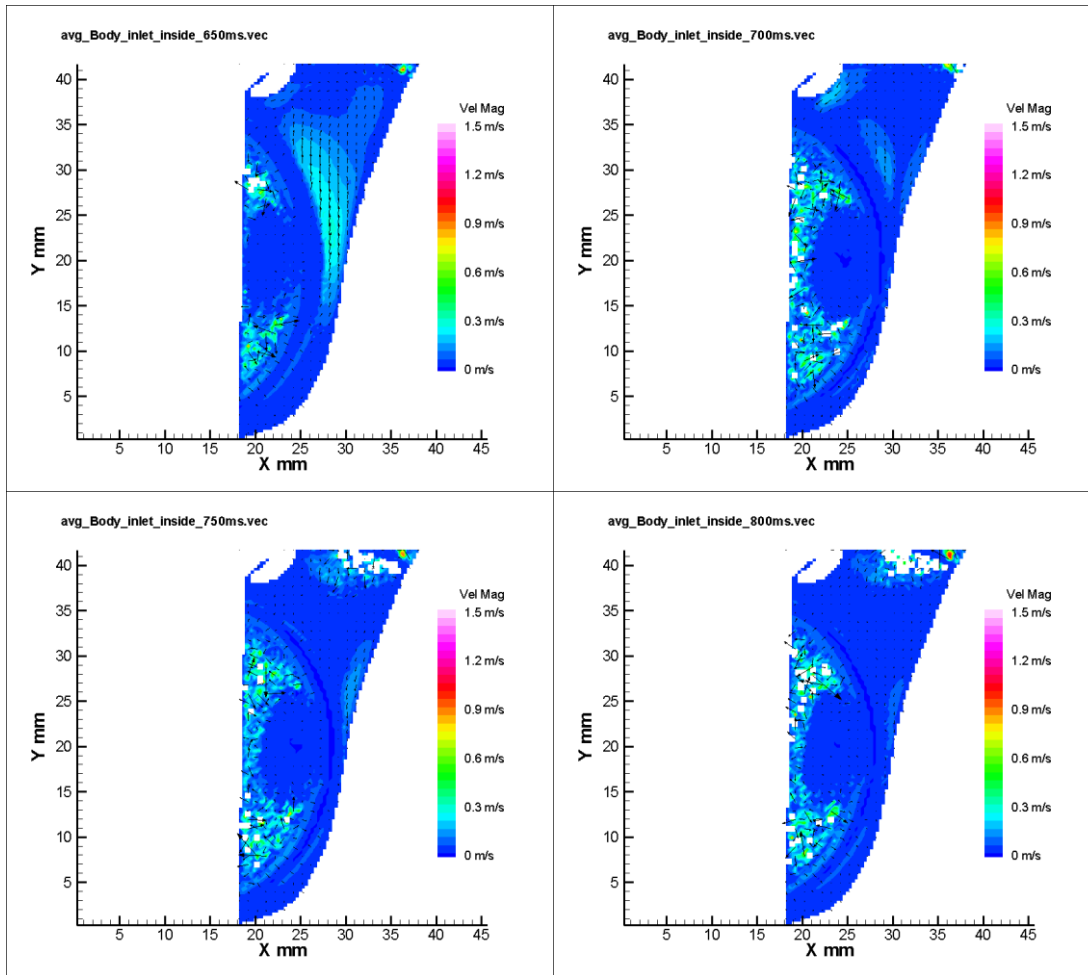
31. Roszelle BN, Cooper BT, Long TC, Deutsch S, and Manning KB: Penn state 12 cc pulsatile pediatric ventricular assist device: flow field observations at a reduced beat rate with application to weaning. *ASAIO J* 54:325-331, 2008. (3)

32. The Organ and Transplantation Procurement Network Web site 2005. Available at: http://www.optn.org. Accessed April 9, 2010.
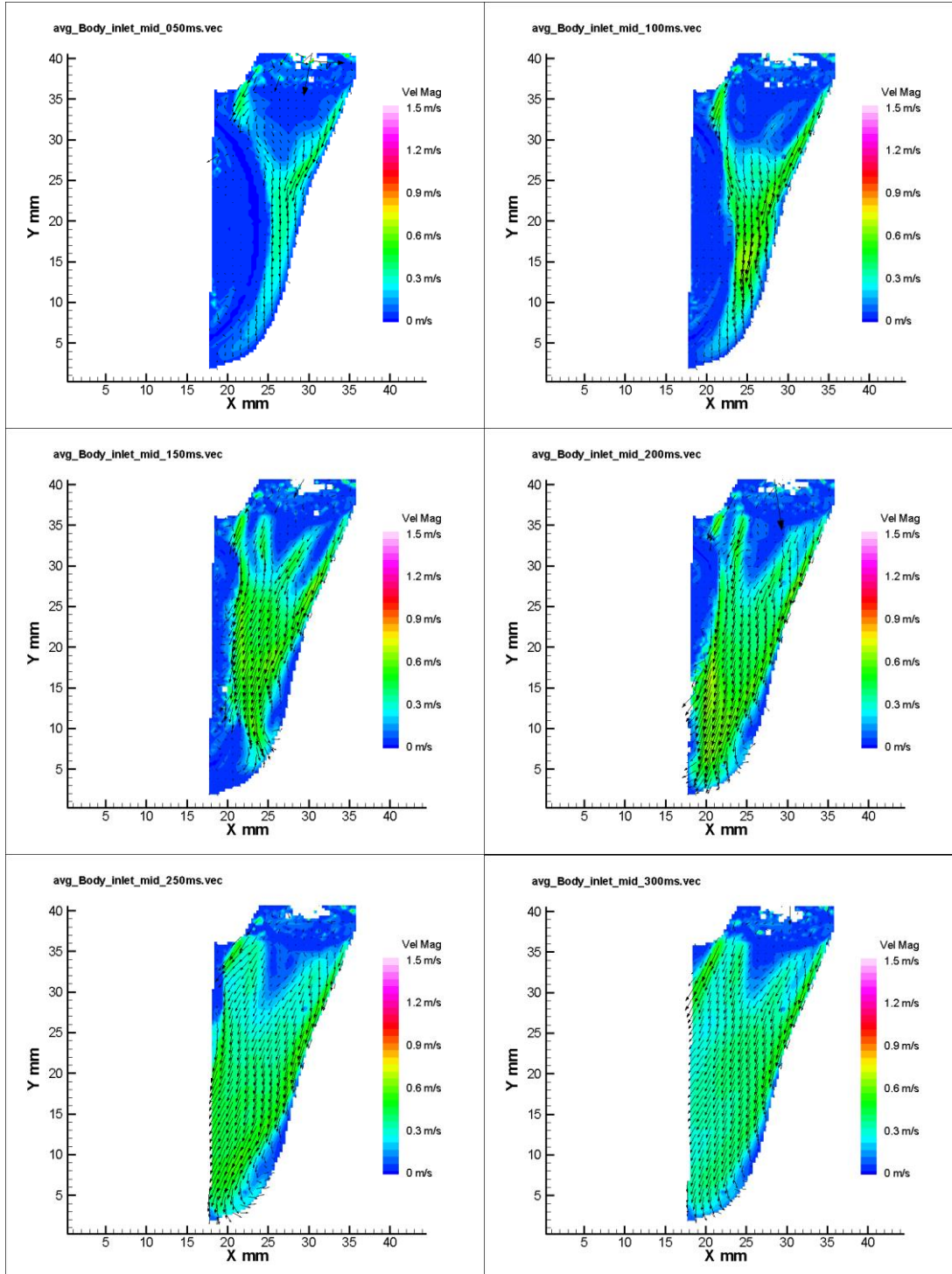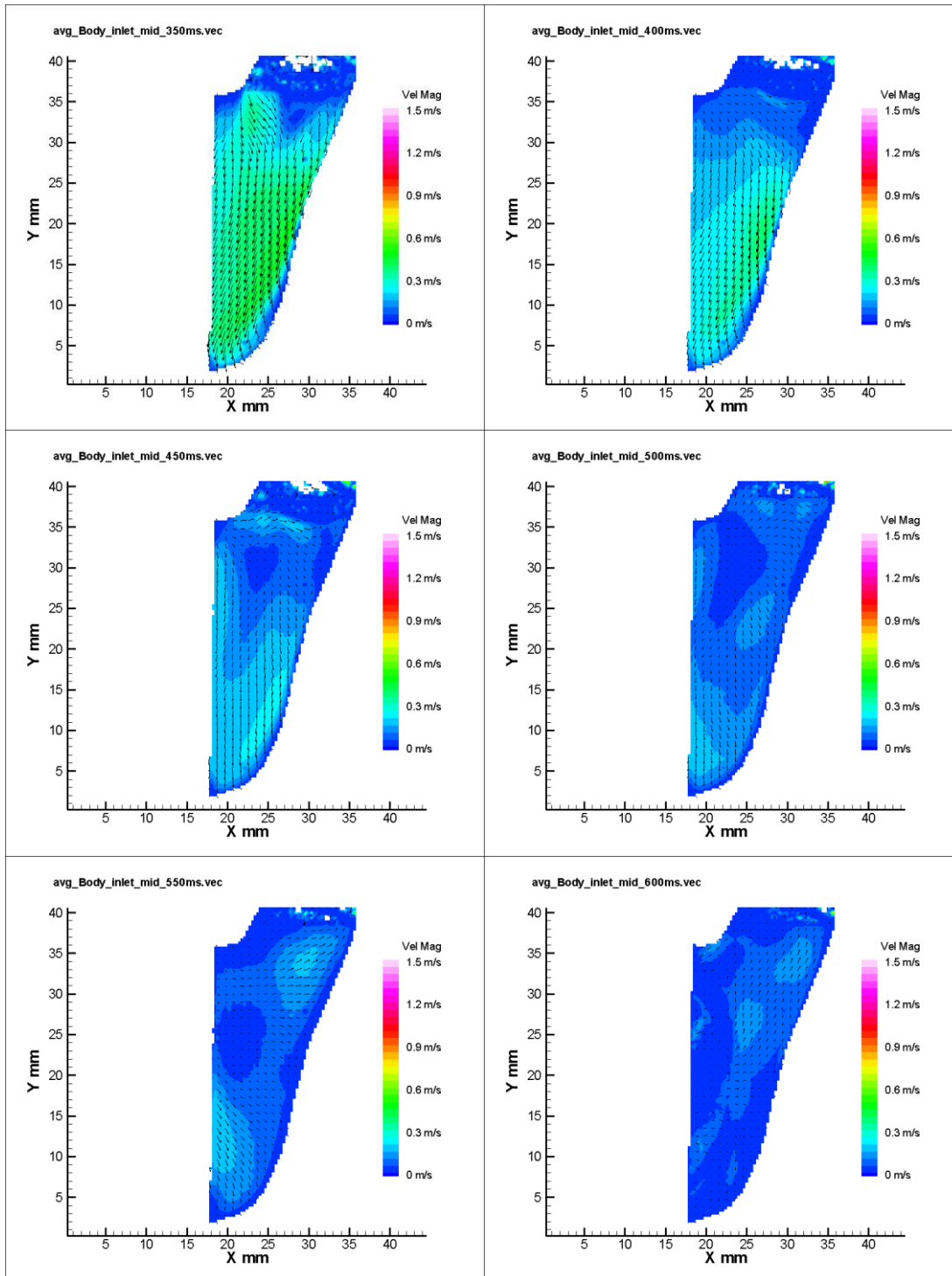
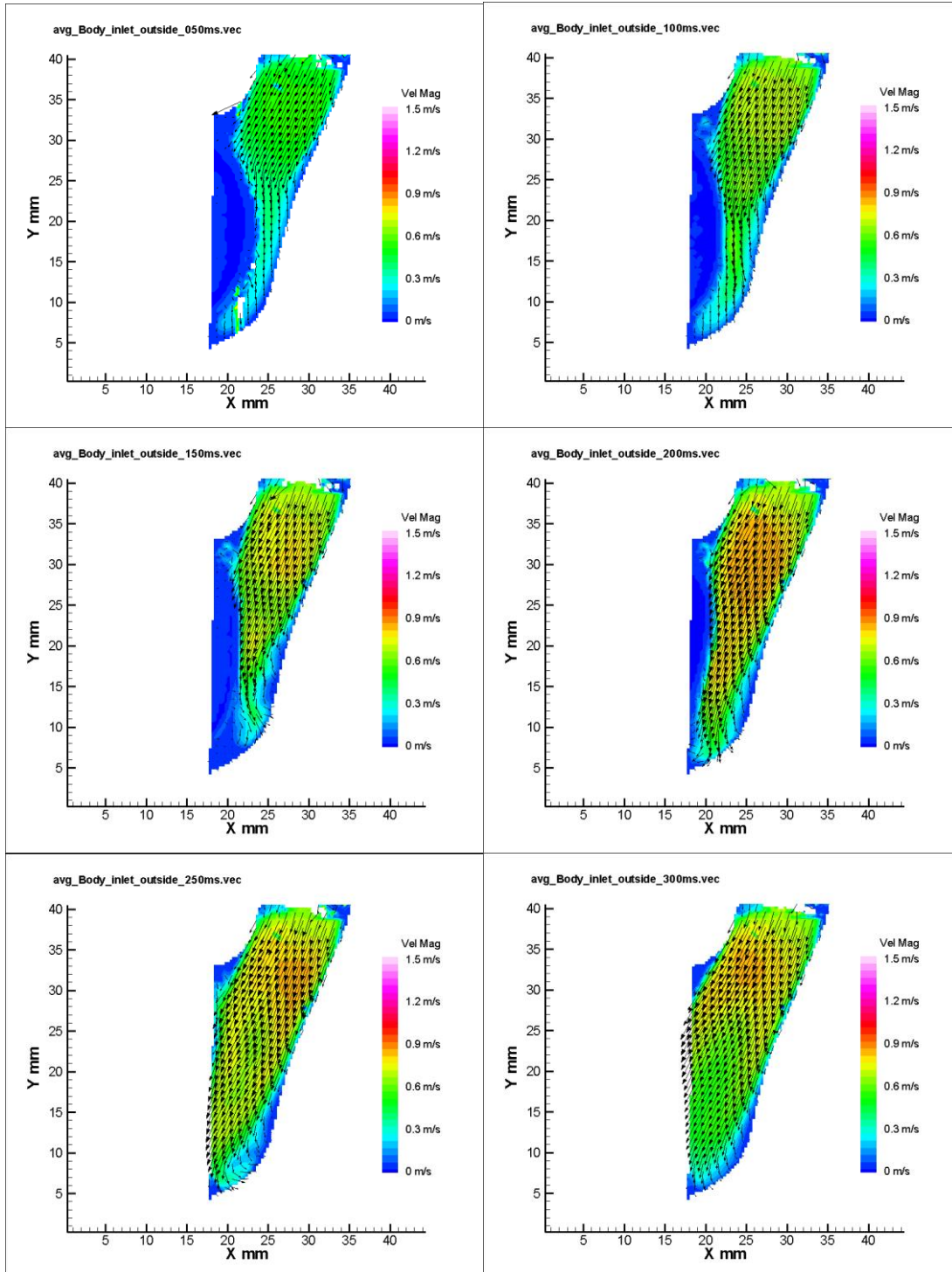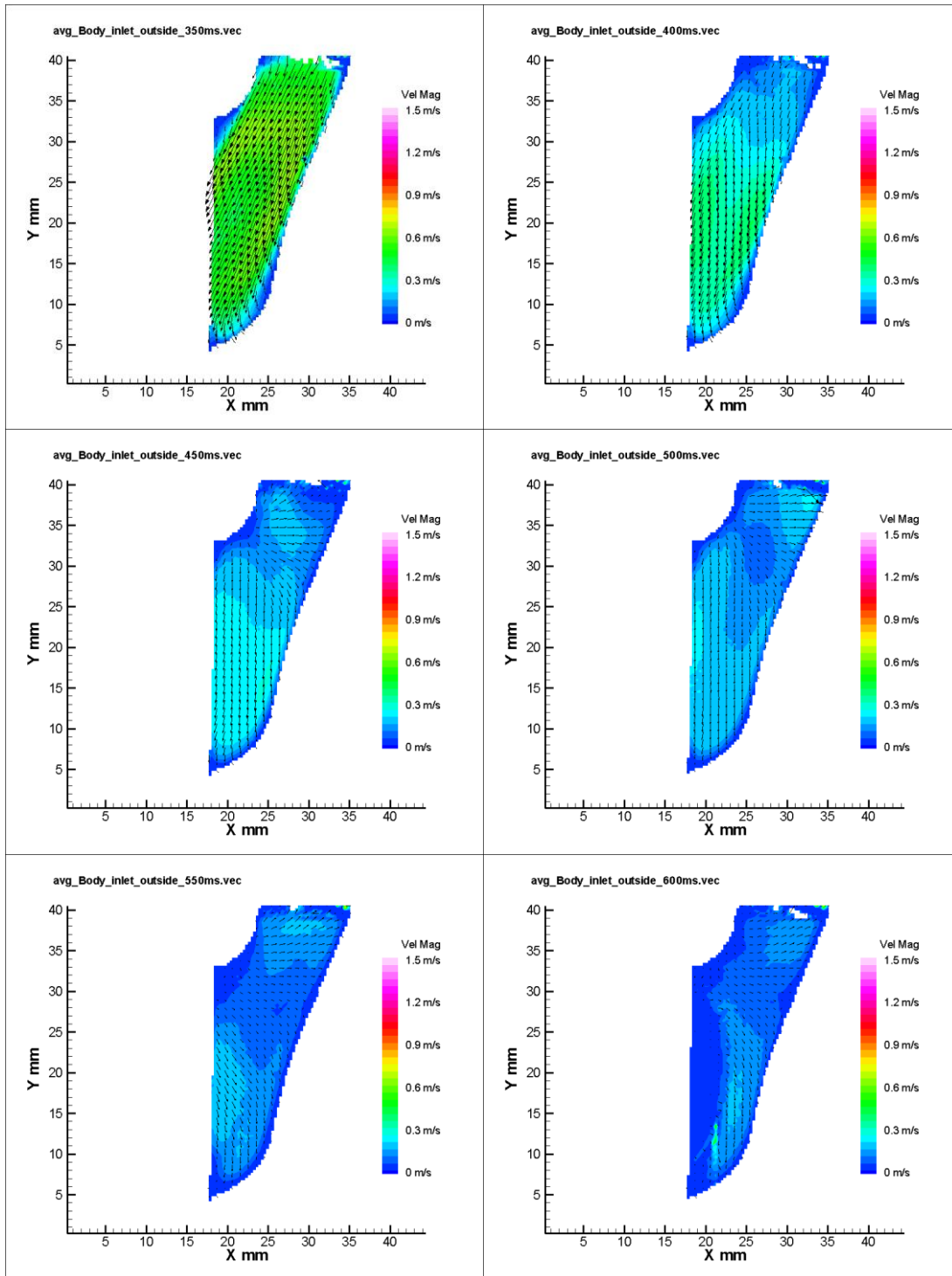# Appendix A – Body Normal Inlet Planes Flow Maps

11.25 mm Inlet Normal Plane

avg_Body_inlet_inside_350ms.vec

avg_Body_inlet_inside_400ms.vec

avg_Body_inlet_inside_450ms.vec

avg_Body_inlet_inside_500ms.vec

avg_Body_inlet_inside_550ms.vec

avg_Body_inlet_inside_600ms.vec

7.5 mm Inlet Normal Plane

avg_Body_inlet_mid_650ms.vec

avg_Body_inlet_mid_700ms.vec

avg_Body_inlet_mid_750ms.vec

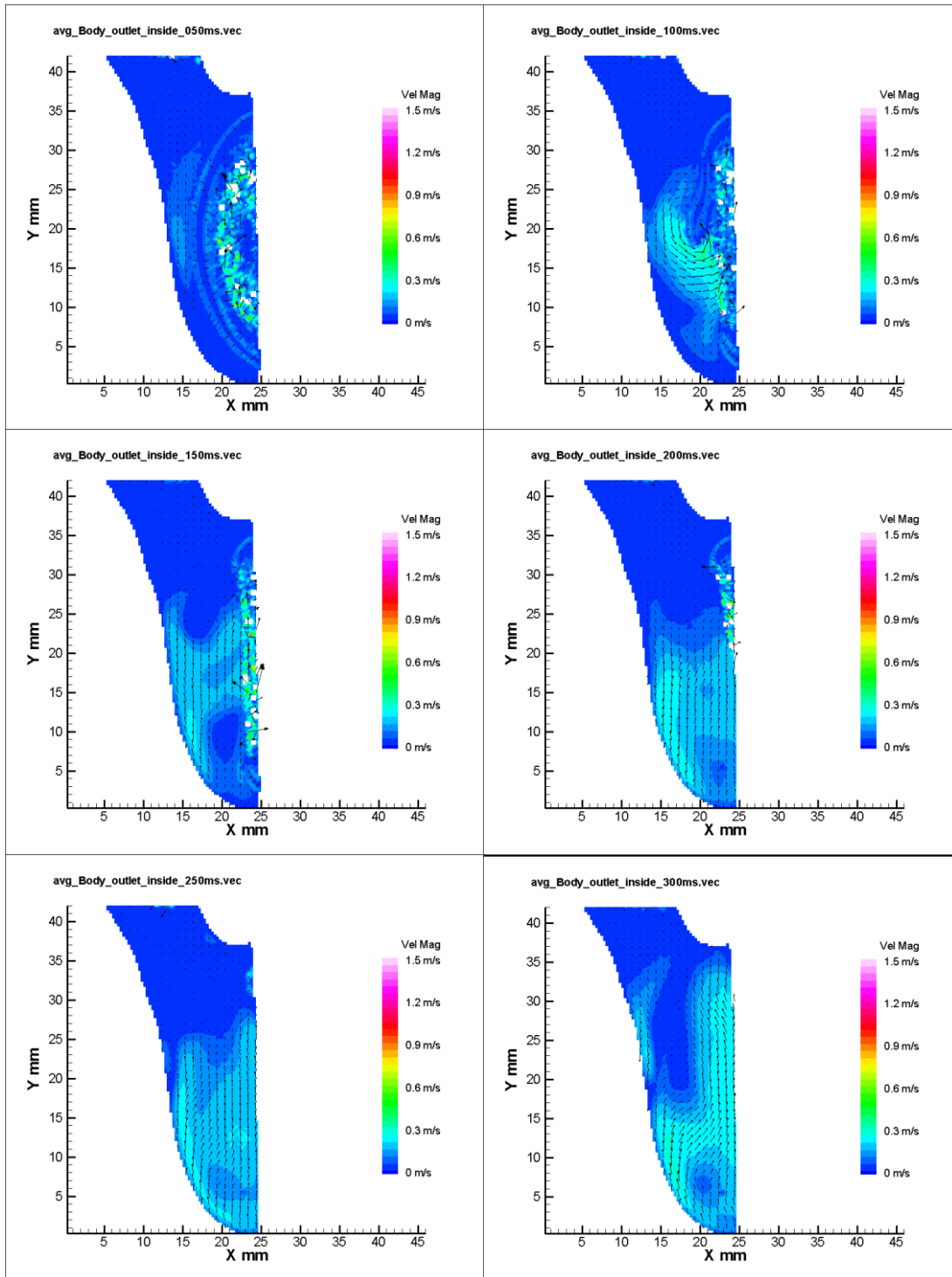avg_Body_inlet_mid_800ms.vec
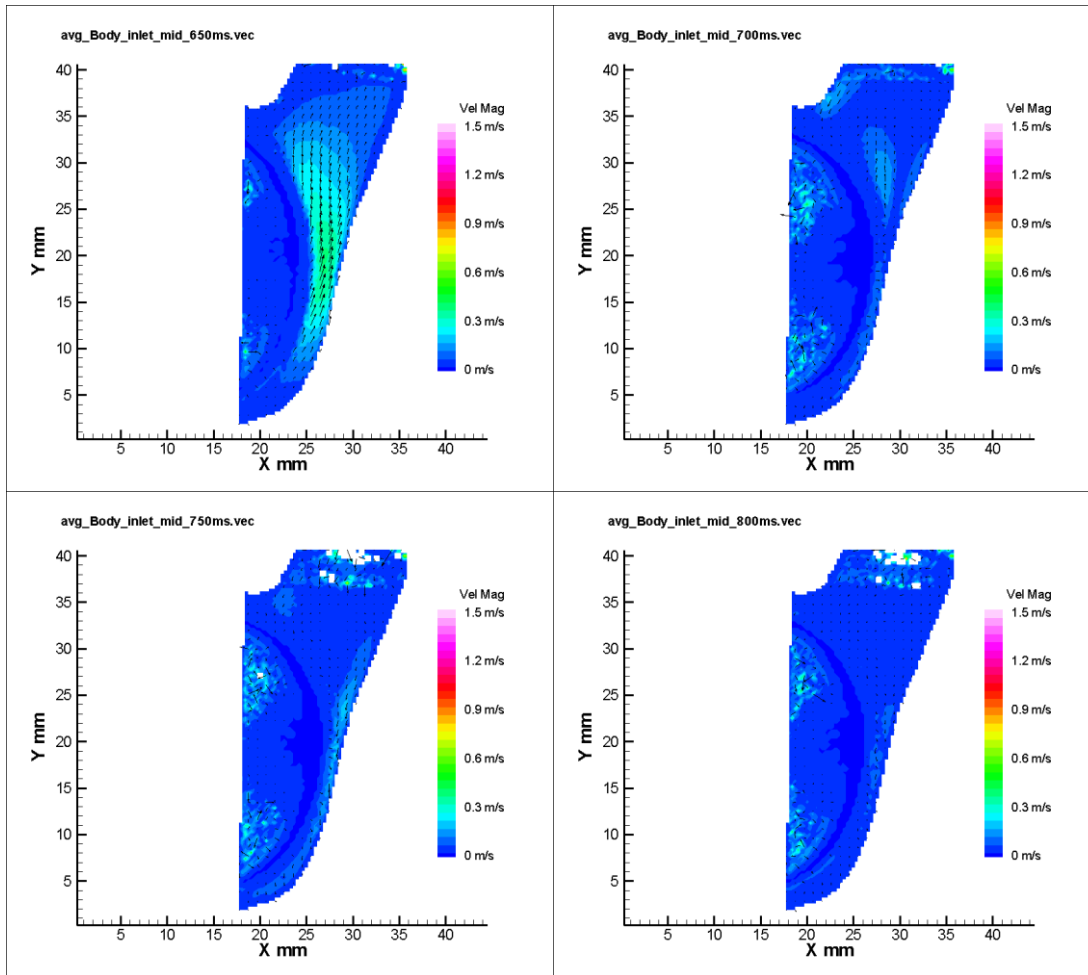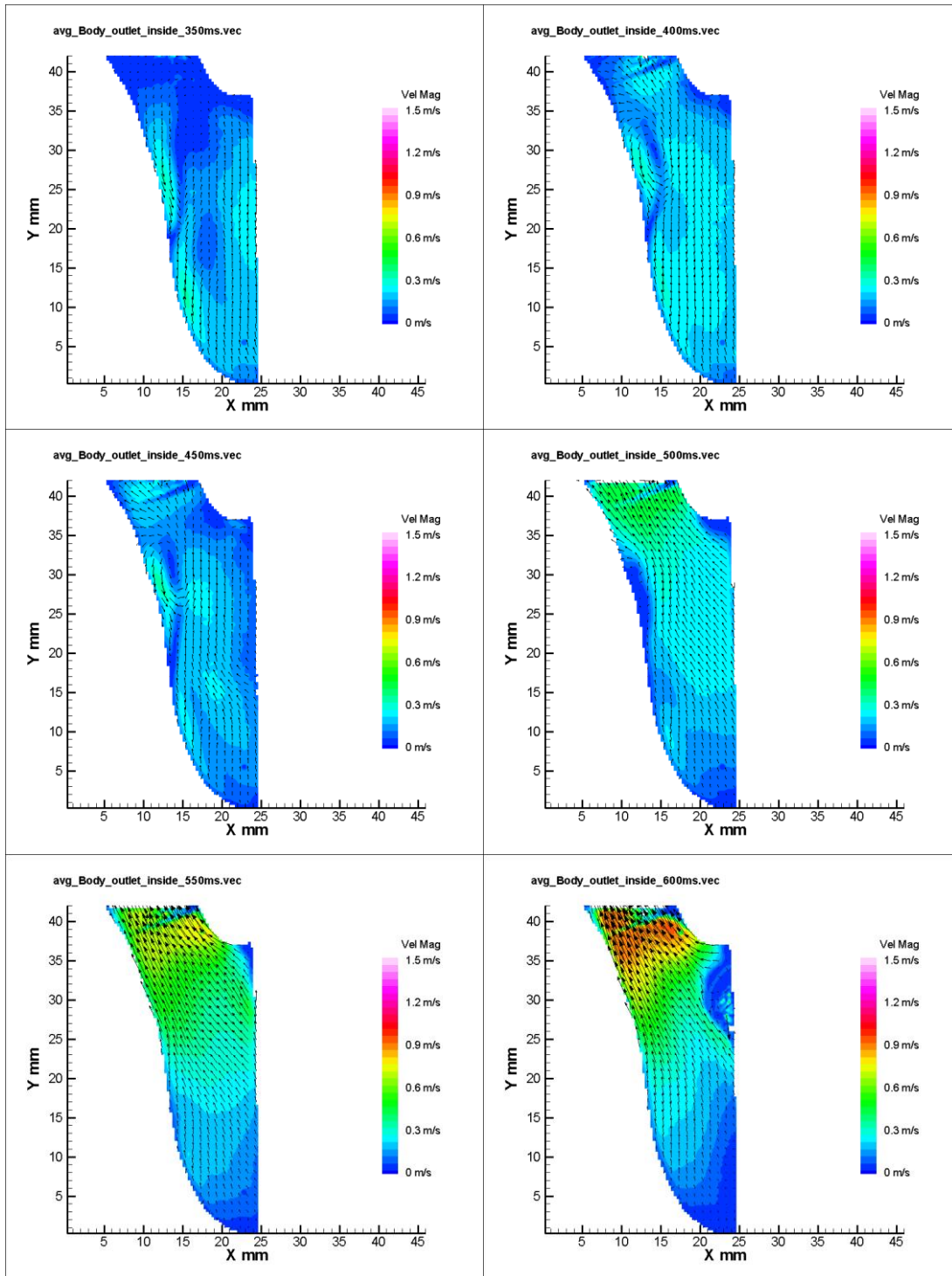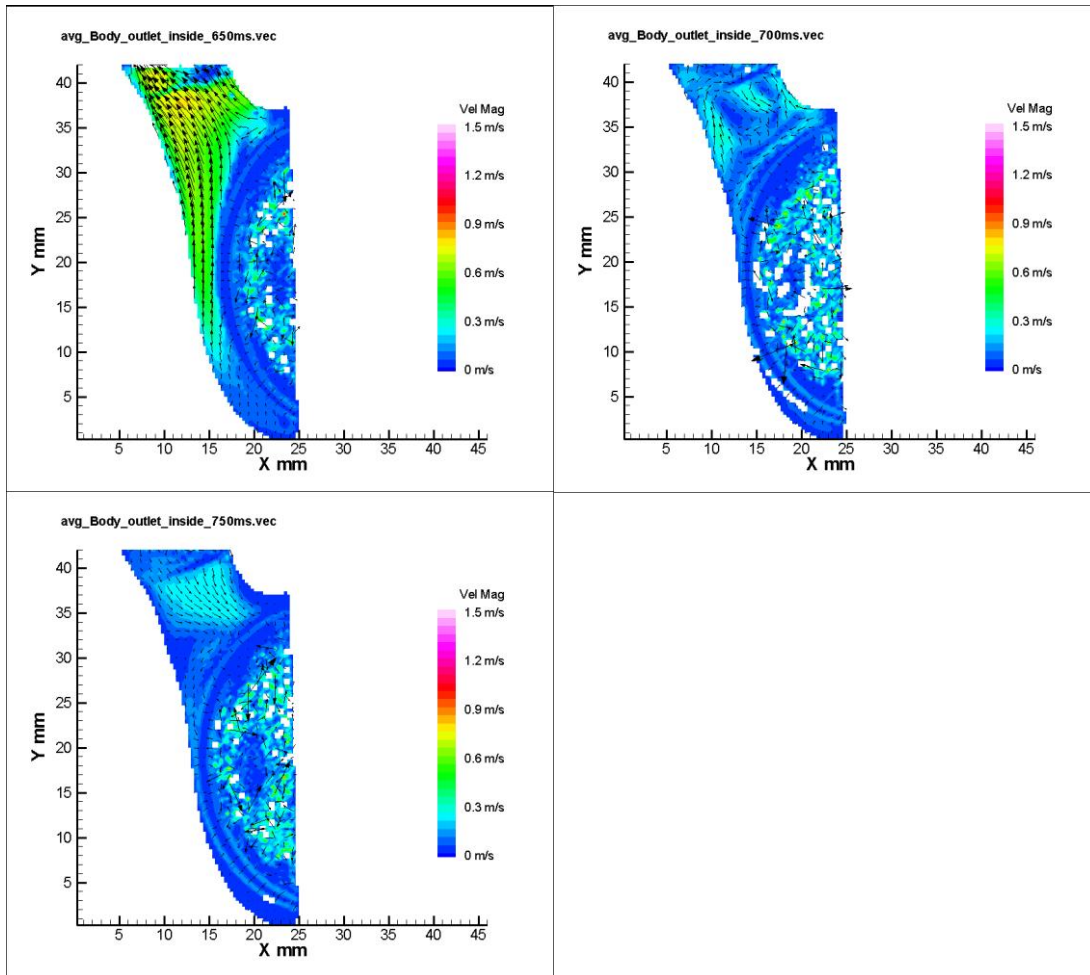
3.75 mm Inlet Normal Plane
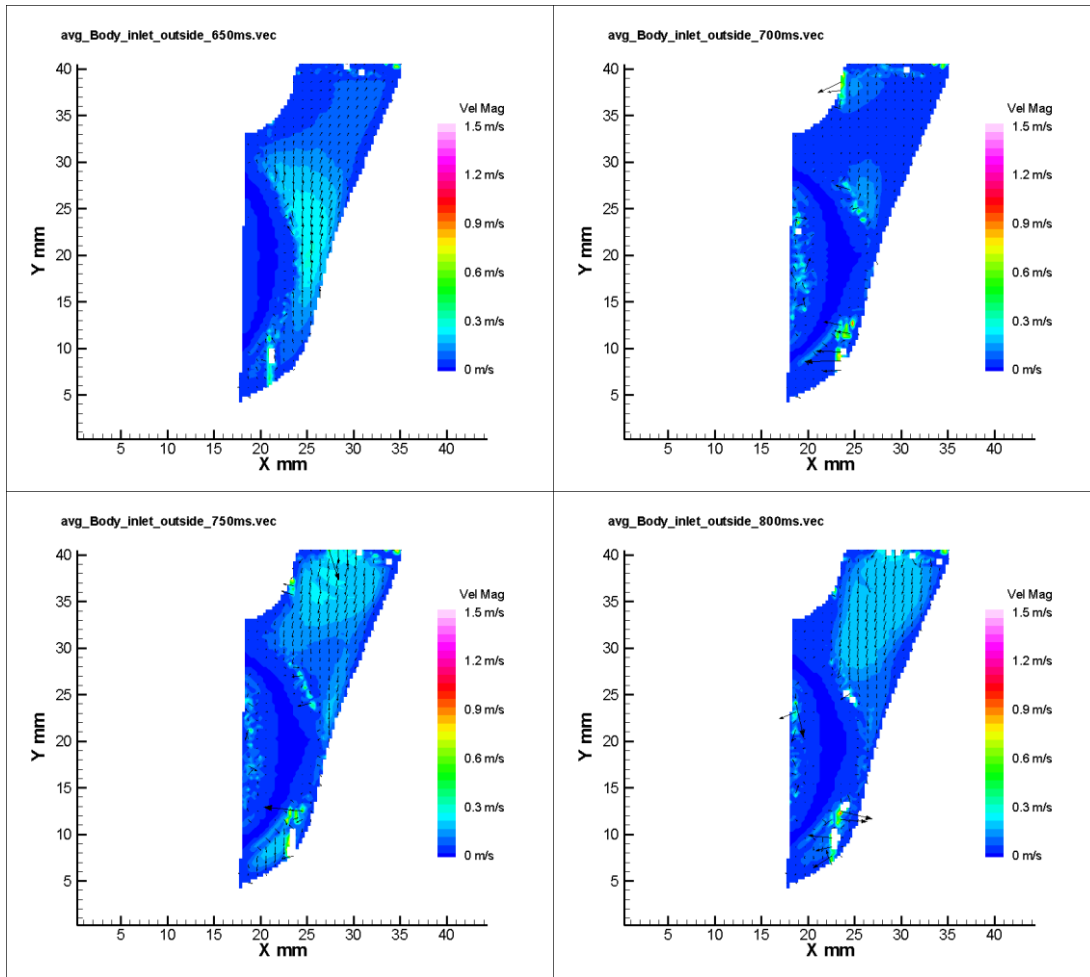
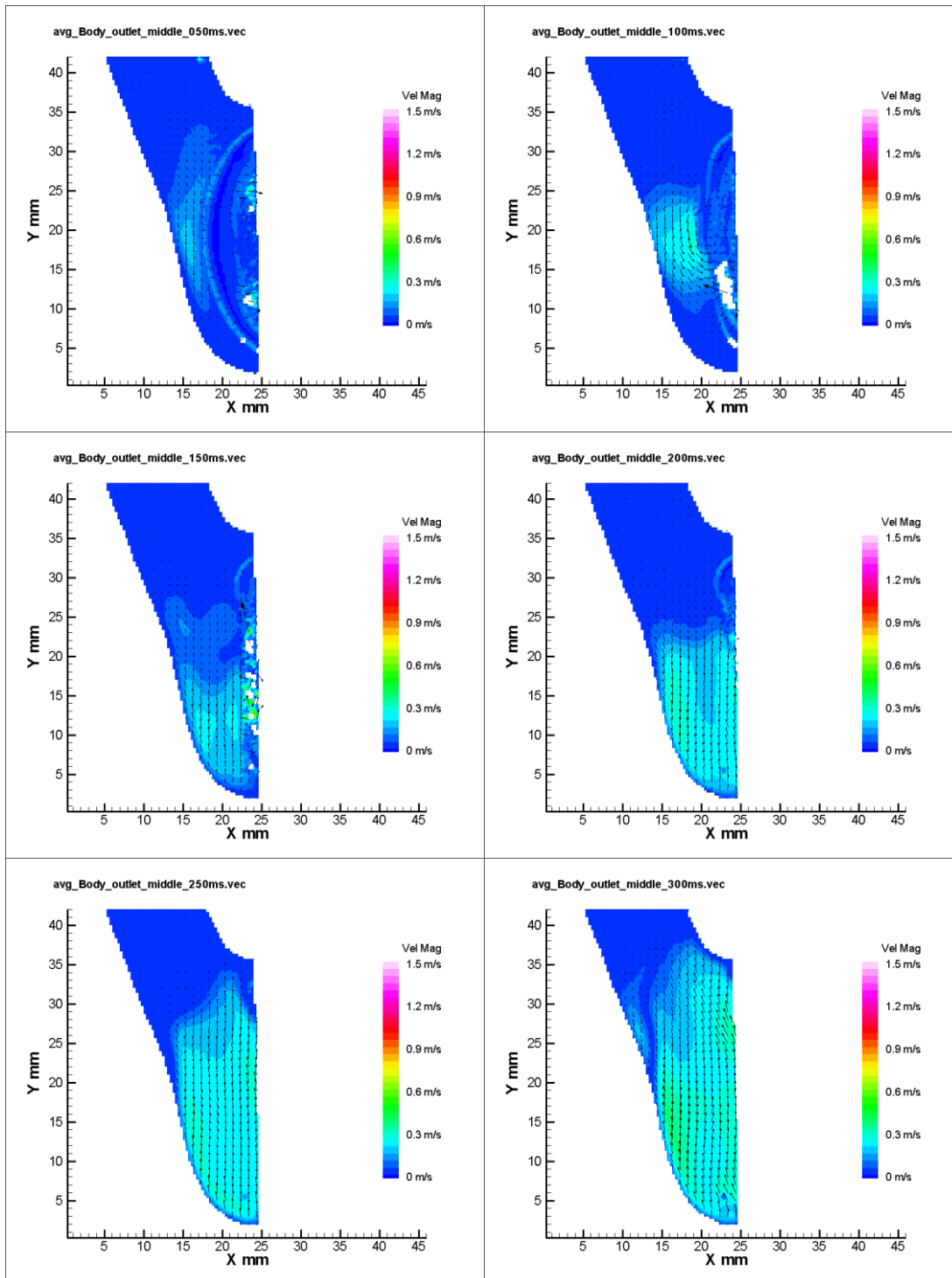# Appendix B – Body Normal Outlet Planes Flow Maps

11.25 mm Outlet Normal Plane

avg_Body_outlet_inside_650ms.vec

avg_Body_outlet_inside_700ms.vec

avg_Body_outlet_inside_750ms.vec

7.5 mm Outlet Normal Plane

avg_Body_outlet_middle_350ms.vec

avg_Body_outlet_middle_400ms.vec

avg_Body_outlet_middle_450ms.vec

avg_Body_outlet_middle_500ms.vec

avg_Body_outlet_middle_550ms.vec

avg_Body_outlet_middle_600ms.vec

avg_Body_outlet_middle_650ms.vec
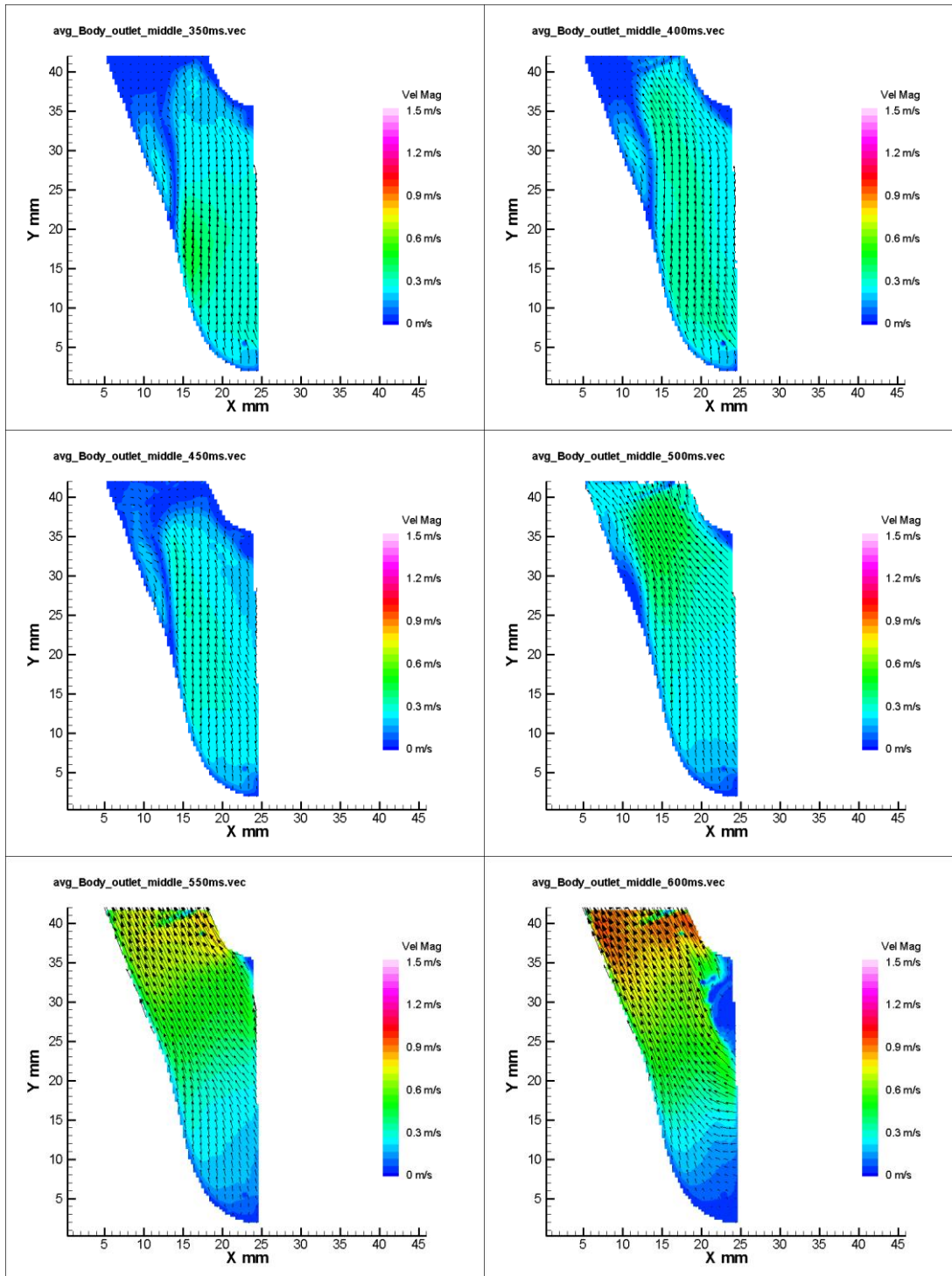
avg_Body_outlet_middle_700ms.vec

avg_Body_outlet_middle_750ms.vec

avg_Body_outlet_middle_800ms.vec

3.75 mm Outlet Normal Plane

avg_Body_outlet_outside_650ms.vec

avg_Body_outlet_outside_700ms.vec

avg_Body_outlet_outside_750ms.vec

avg_Body_outlet_outside_800ms.vec

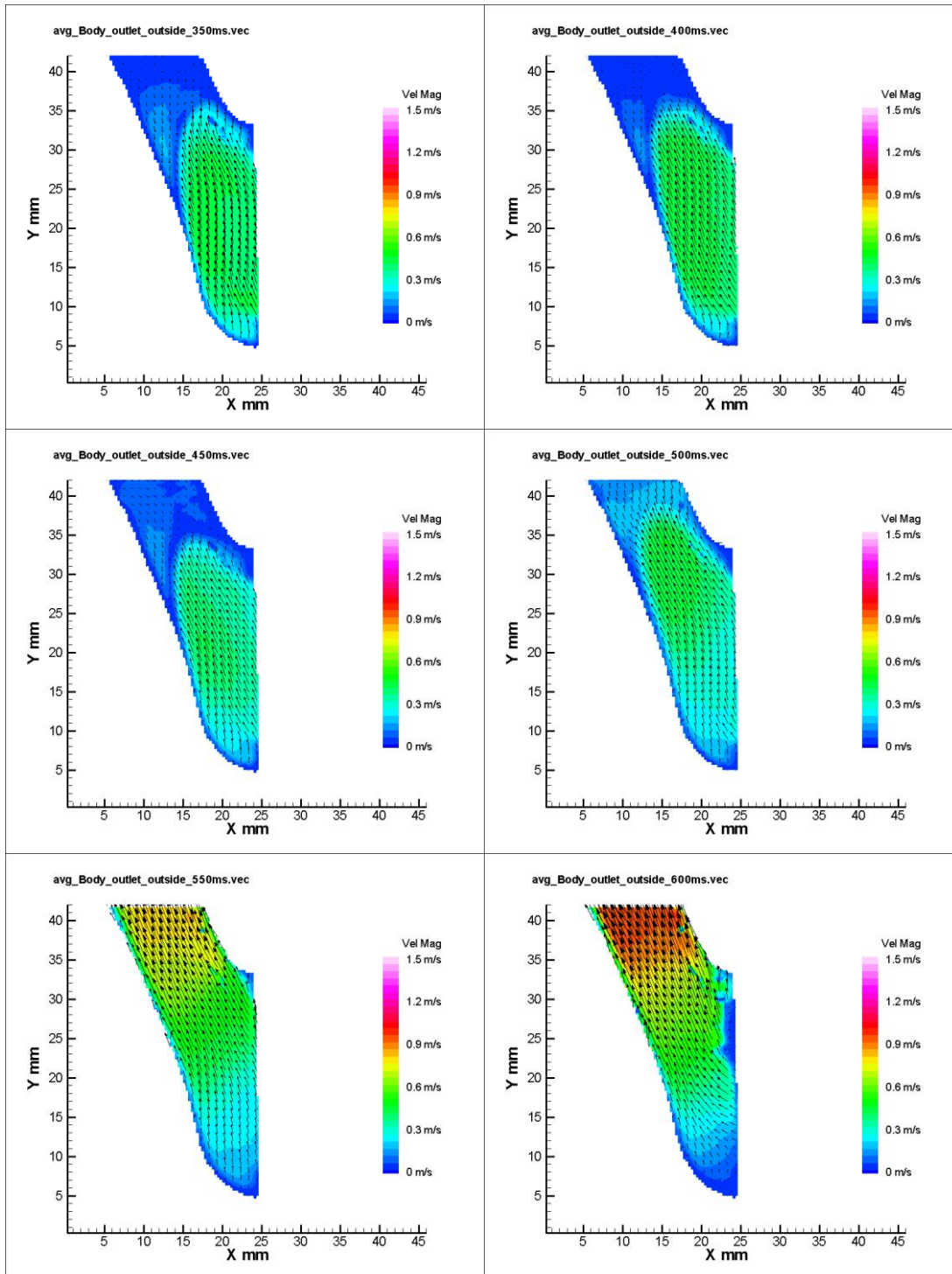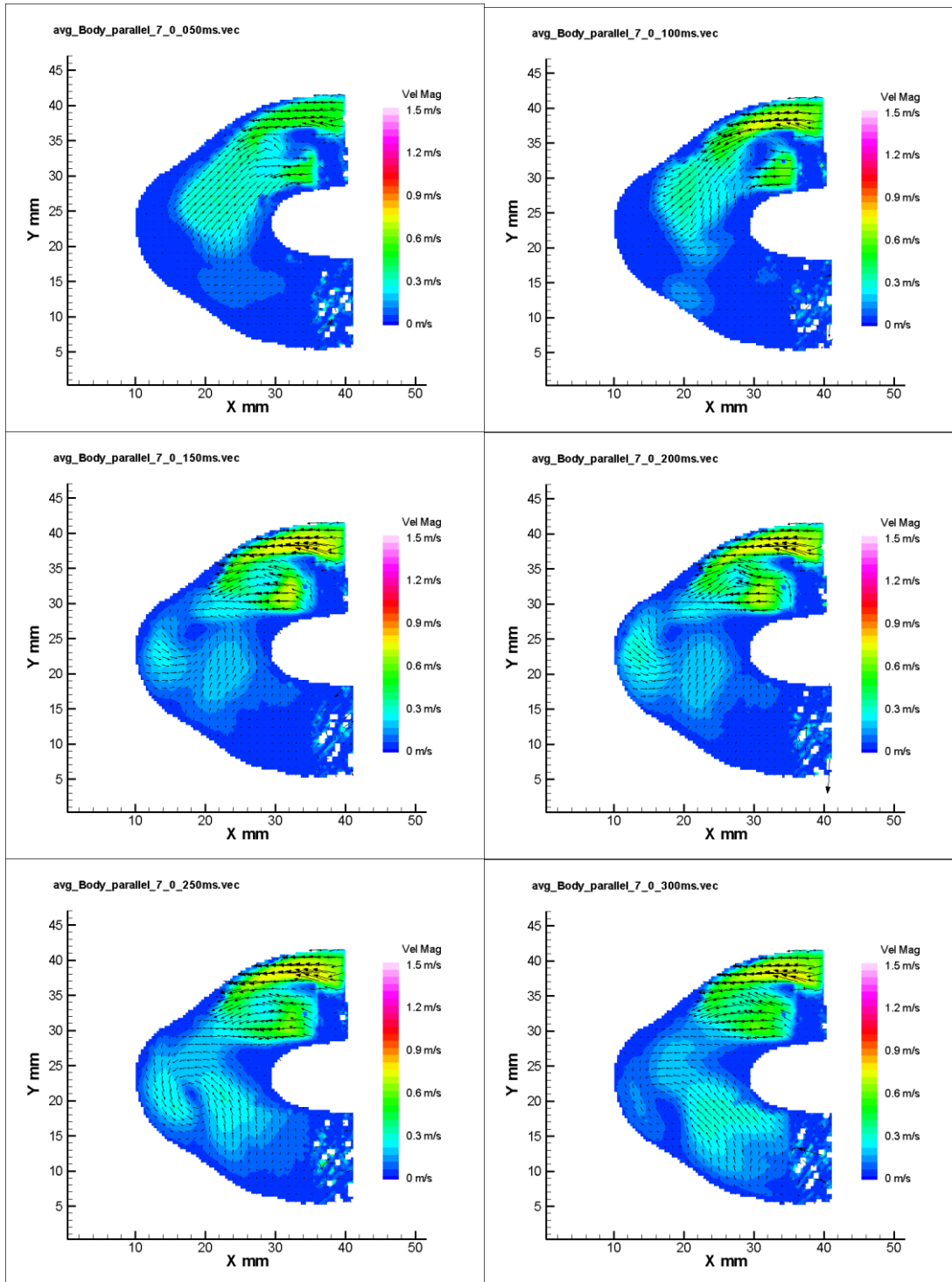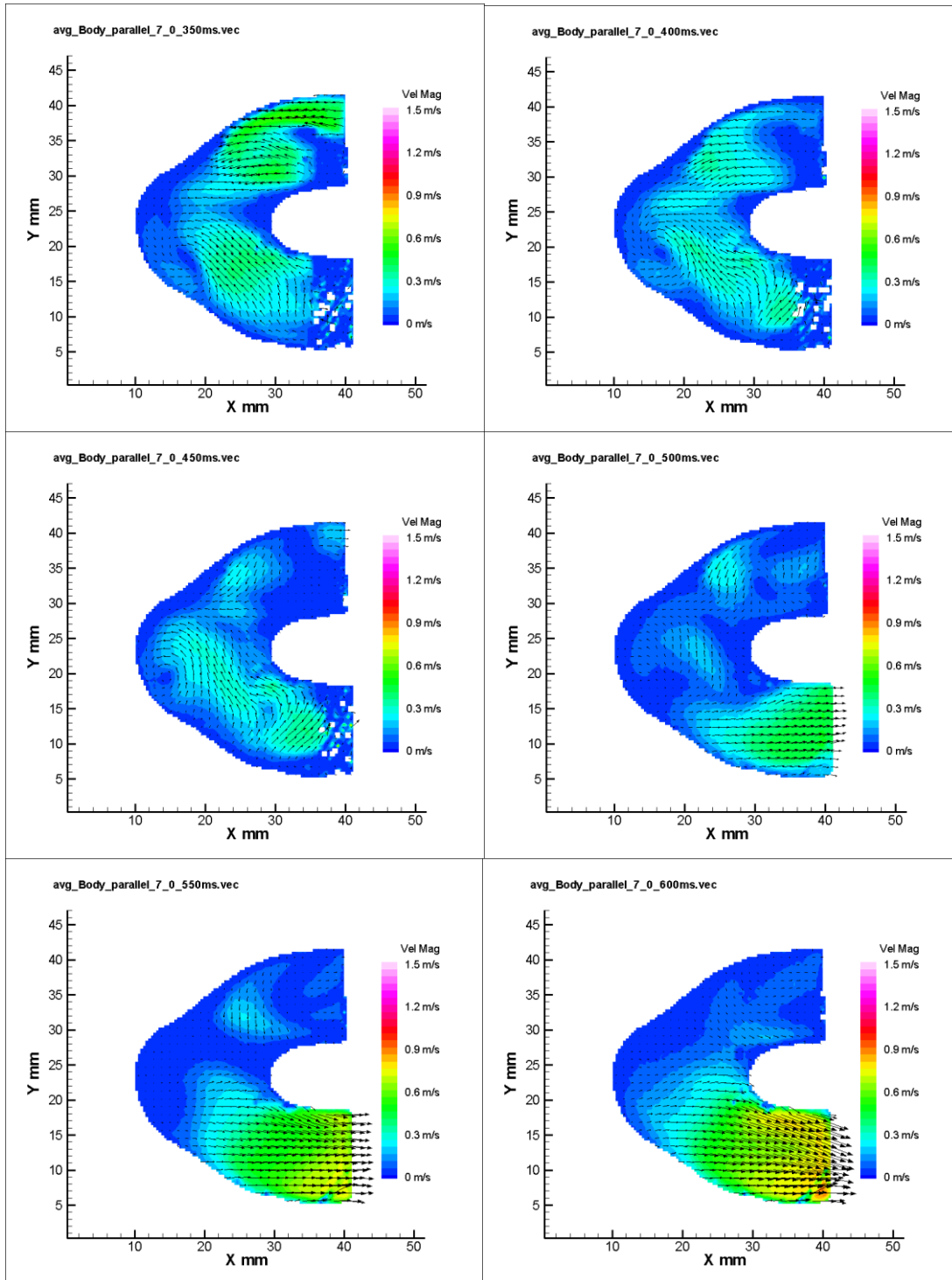# Appendix C – Body Parallel Planes Flow Maps

7.0 mm Body Parallel Plane

avg_Body_parallel_7_0_350ms.vec

avg_Body_parallel_7_0_400ms.vec

avg_Body_parallel_7_0_450ms.vec

avg_Body_parallel_7_0_500ms.vec

avg_Body_parallel_7_0_550ms.vec

avg_Body_parallel_7_0_600ms.vec

8.2 mm Body Parallel Plane

avg_Body_parallel_8_2_350ms.vec

avg_Body_parallel_8_2_400ms.vec

avg_Body_parallel_8_2_450ms.vec

avg_Body_parallel_8_2_500ms.vec

avg_Body_parallel_8_2_550ms.vec

avg_Body_parallel_8_2_600ms.vec

avg_Body_parallel_8_2_650ms.vec

avg_Body_parallel_8_2_700ms.vec

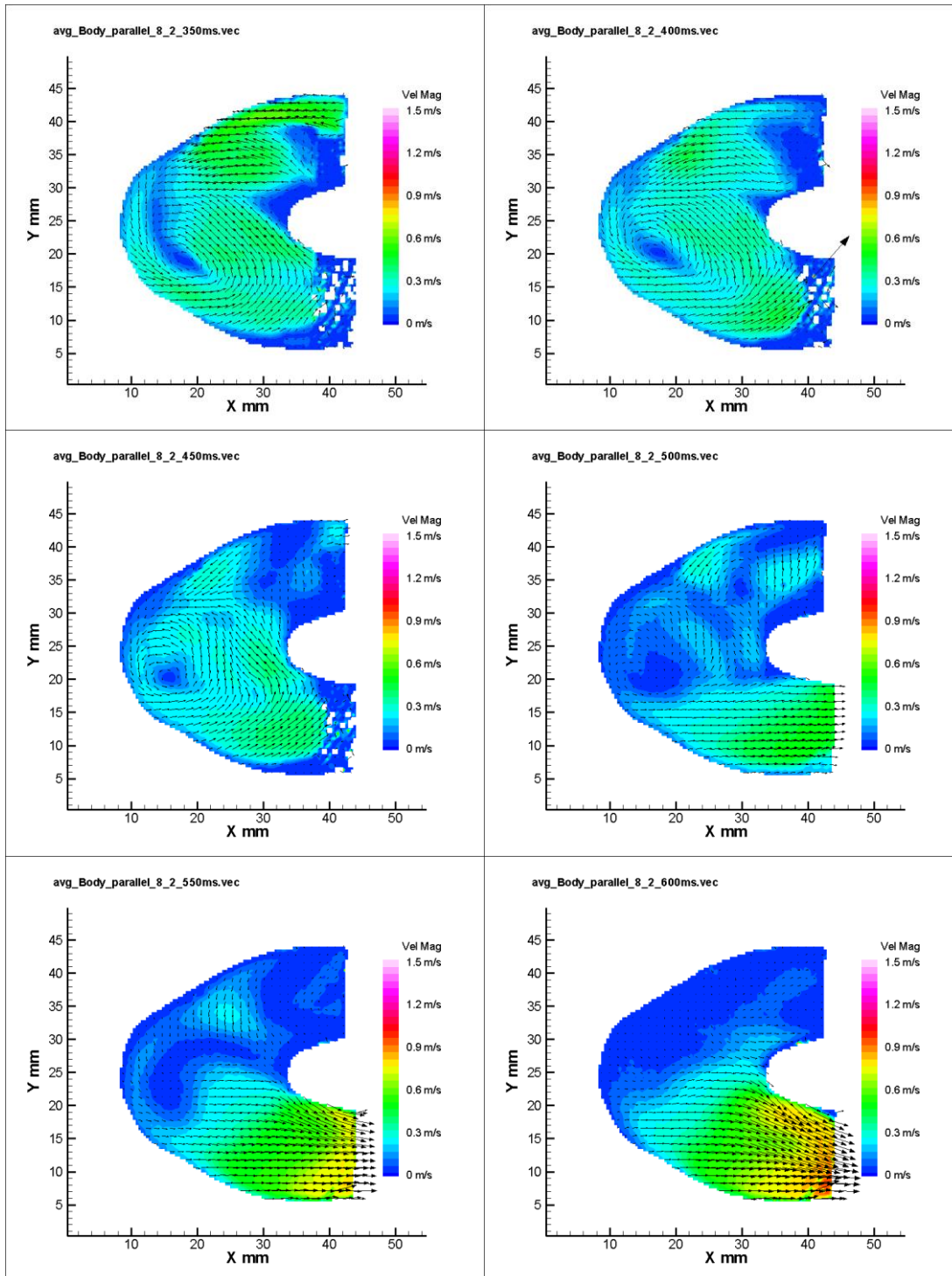avg_Body_parallel_8_2_750ms.vec

avg_Body_parallel_8_2_800ms.vec

11.0 mm Body Parallel Plane

avg_Body_parallel_11_0_350ms.vec

avg_Body_parallel_11_0_400ms.vec

avg_Body_parallel_11_0_450ms.vec

avg_Body_parallel_11_0_500ms.vec

avg_Body_parallel_11_0_550ms.vec

avg_Body_parallel_11_0_600ms.vec

Permanent Address
325 West Locust Lane
Kennett Square, PA 19348
Phone: 610-444-1017

MICHAEL G. FICKES

mgf5009@psu.edu
U.S. Citizen

Local Address
138 S. Atherton St. Apt# 509
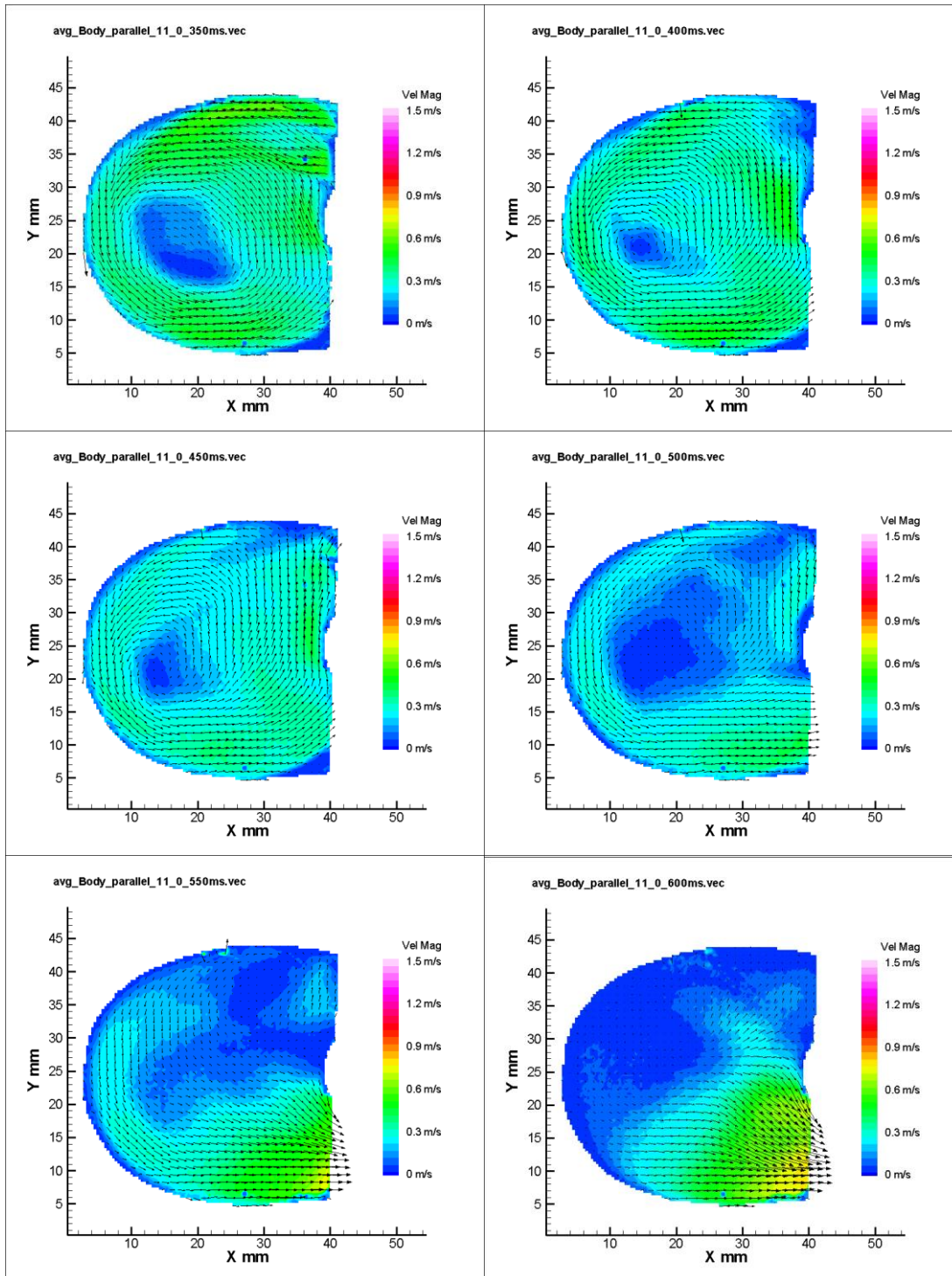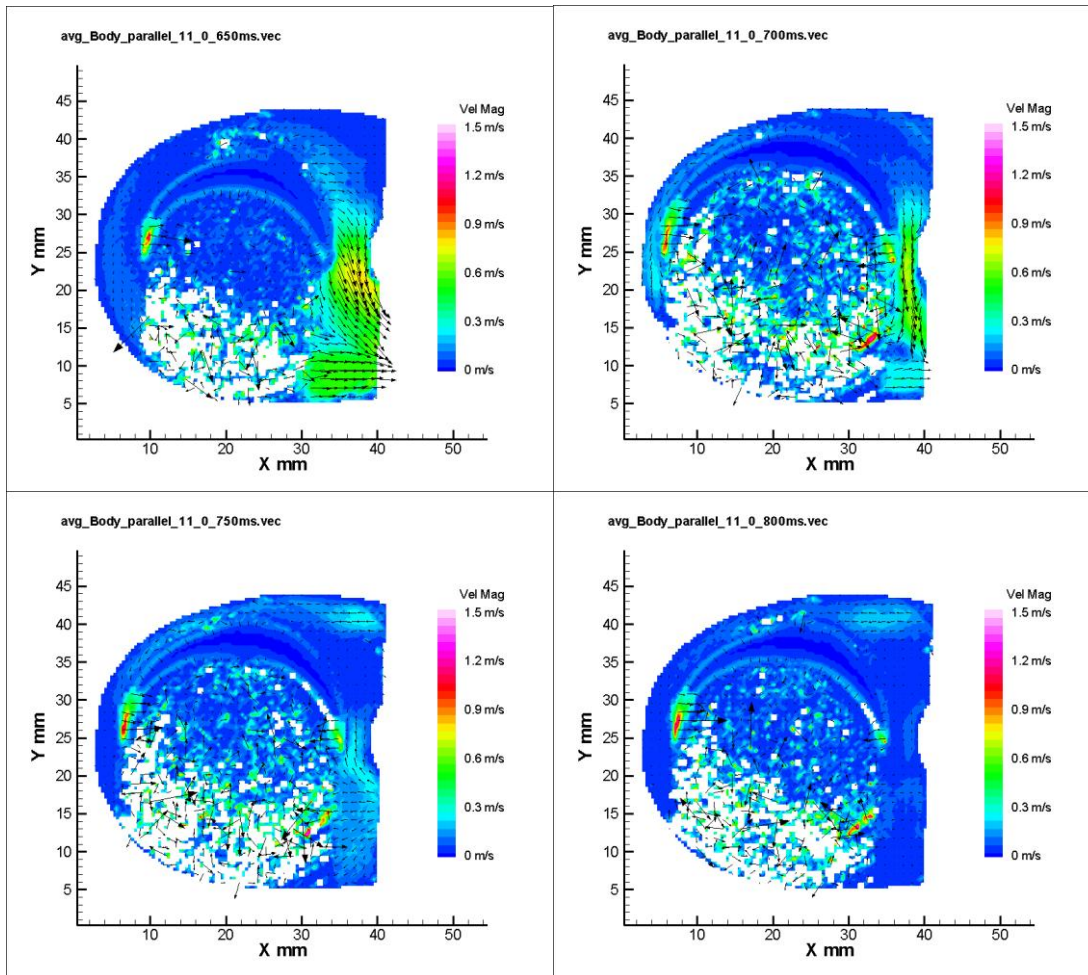State College, PA 16801
Cell: 610-301-2984

OBJECTIVE

To gain the necessary experience to pursue a career in the medical field, with a focus on novel surgical techniques

OFFERING

Demonstrated Leadership Skills in both research and academia
Effective Communication Skills in formal presentations and cross-functional networking
Extensive technical background in cardiac assist devices and cardiovascular flow
Research background in Gastroenterology

EDUCATION

The Pennsylvania State University, University Park, PA
Bachelor of Science in Bioengineering
Schreyer Honors Scholar, Class of 2010

RELEVANT EXPERIENCE

The Pennsylvania State University State College, PA   Fall 2008-Present
Researcher in Artificial Heart Lab
- ➢ Trained in MATLAB
- ➢ Assists Graduate students and Senior Undergraduates with Thesis Research
- ➢ Currently finishing a thesis on an extension of the outlet valve to the current 12cc Penn State Pediatric Ventricular Assist Device to minimize the probability of blood damage
- ➢ Will be presenting at an undergraduate research exhibition later this semester and an ASAIO conference over the summer

Northwestern University/The Feinberg School of Medicine Chicago, IL
Jun 2008-July 2008
Volunteer Researcher
- ➢ Utilizing lab techniques to analyze tissue samples from eosinophillic esophagitis (EE) patients to determine up-regulated and down-regulated genes in EE
- ➢ Performing various analytical tests including RNA purification, DNA microarray, Laser Capture Microdissection (LCM)
- ➢ Responsible for maintaining and updating two databases on samples collected in general and samples pertaining to the disease EE
- ➢ Collected samples from operating room and transported them to lab

Northwestern University/The Feinberg School of Medicine Chicago, IL
Jun 2009-August 2009
Grant-Funded Researcher
- ➢ Received a summer research grant through the Crohn's and Colitis Foundation of America
- ➢ Used mice to model colitis in the colon using α-CD3 to determine the pathway mesalamine acts through in order to be chemopreventive
- ➢ Dissected mice to obtain colon, fixed tissue in parafilm, sectioned tissue with a microtome, and used various staining techniques to determine protein levels within the tissue sections

Permanent Address
325 West Locust Lane
Kennett Square, PA 19348
Phone: 610-444-1017

MICHAEL G. FICKES

mgf5009@psu.edu
U.S. Citizen

Local Address
138 S. Atherton St. Apt# 509
State College, PA 16801
Cell: 610-301-2984

Kennett Area YMCA Kennett Square, PA   May 2007-Sept 2008
Lifeguard
  ➢ Fully certified Lifeguard, CPR/First Aid
  ➢ Responsible for ensuring the safety of club membership
  ➢ Supervise both indoor and outdoor facilities

**ACTIVITIES
& HONORS**

College of Engineering Dean's List, Fall '06 - Fall '08 and Fall '09
Student Red Cross Club
  ➢ Active Member Fall '06 - Spring '10
  ➢ On Site Coordinator Fall '06 - Spring '10
  ➢ Information Technology Officer for the 2008-2009 and 2009-2010
     school years
       -Responsible for maintaining a professional webpage that
       represents the organization
       -Made critical planning decisions for 4 major blood drive
       campaigns in the Greater Alleghenies Blood Region each year
Residence Hall Associations
  ➢ Blood Drive Chair: East Halls Fall '06 - Spring '07
  ➢ Blood Drive Chair: West Halls Fall -07 - Spring '10
Alpha Epsilon Delta, (Premedical Honors Society) Honors Member

SKILLS
Methods

Laboratory: NMR and IR Spectroscopy, Various Chromatography

Computer: Microsoft Word/Excel/PowerPoint/Front Page, C++, Solid
Works, MATLAB
Languages: Basic French